Dissertation

submitted to the
Combined Faculties of the Natural Sciences and Mathematics
of the Ruperto-Carola-University of Heidelberg, Germany
for the degree of
Doctor of Natural Sciences

Put forward by

Alexander Rischka

born in: Datteln, Germany

Oral examination: 27-06-2018

The First Direct Q_{EC} Measurement in ^{163}Ho and the Development of the High-Precision Mass Spectrometer PENTATRAP for Neutrino Physics

Referees: Prof. Dr. Klaus Blaum
Prof. Dr. Ulrich Uwer

ZUSAMMENFASSUNG

Für die Verbesserung der oberen Grenze der effektiven Neutrinomasse im unteren eV/c^2 Bereich, wird in der ECHo-Kollaboration unter Einsatz von Mikrokalorimetern das Abregespektrum im Elektroneneinfangprozess von ^{163}Ho nach ^{163}Dy gemessen. Um systematische Fehler auszuschließen, wird eine unabhängige Hochpräzisionsmessung des Q-Wertes vom Elektroneneinfang in ^{163}Ho benötigt. Zunächst jedoch musste die Diskrepanz zwischen den neuesten mikrokalorimetrischen Messungen des Q-Wertes zum Literaturwert geklärt werden. Dazu wurde die erste direkte Messung des Q-Wertes an dem Penningfallen-Massenspektrometer SHIPTRAP durchgeführt. Innerhalb des Fehlers stimmt dieser Wert mit den mikrokalorimetrischen Messungen überein. Zudem konnte mit Hilfe der neuen PI-ICR Methode eine so gute Genauigkeit erreicht werden, dass dieser Wert auch für die erste Phase von ECHo (ECHo-1K) als unabhängige Messung des Q-Wertes benutzt werden kann. Es ist geplant mit ECHo-1k die Obergrenze der Elektron-Neutrinomasse von $224\,eV/c^2$ auf ca. $10\,eV/c^2$ zu verbessern. Für weitere Verbesserungen in der Obergrenze der Elektron-Neutrinomasse muss der Q-Wert des EC in ^{163}Ho mit einer Unsicherheit von wenigstens $2\,eV/c^2$ bestimmt werden. Dafür ist ein neues Penningfallen-Massenspektrometer mit dem Namen PENTATRAP entwickelt und in Betrieb genommen worden. PENTATRAP wird fünf Penningfallen benutzen, um neue Messschemata mit drastisch verbesserten systematischen Unsicherheiten zu testen. Damit sollen relative Massenunsicherheiten im Bereich 10^{-12} erstmalig erreicht werden. Abschließend wurden im Rahmen der vorligenden Arbeit erste Testmessungen mit den bekannten Massen von Xenon-Isotopen (^{132}Xe und ^{131}Xe) durchgeführt, um die Leistungsfähigkeit von PENTATRAP zu testen.

ABSTRACT

An improvement of the upper limit of the electron neutrino mass to a sub-eV/c^2 level is the goal of the ECHo collaboration. The upper limit of the neutrino mass will be determined with cryogenic microcalorimetry from the analysis of the atomic de-excitation spectrum of ^{163}Dy after the EC in ^{163}Ho. To check for systematic errors an independent measurement of the Q-value of the EC in ^{163}Ho is required. For the first phase of ECHo the issue with the discrepancy between the latest microcalorimetry measurements of the Q-value and its literature value needed to be fixed. For this, a first direct measurement of the Q-value of the EC in ^{163}Ho with the Penning-trap mass spectrometer SHIPTRAP was accomplished in the context of this thesis using the novel PI-ICR technique. Within the uncertainty, it agrees with the latest microcalorimetry measurements. Furthermore, the achieved precision is sufficient for ECHo-1k to be able to improve the upper limit of the electron neutrino mass to $10\,eV/c^2$ (95% C.L.). For further improvements on the neutrino mass, the Q-value needs to be improved, too. For this, the novel high precision Penning-trap mass spectrometer PENTATRAP has been developed and commissioned. PENTATRAP will utilize five Penning traps to test new measurement schemes, which could make it possible to reach un-

certainties in the 10^{-12} regime. Currently, first mass-ratio measurements of the nuclei pair ^{132}Xe and ^{131}Xe with known masses were carried out to test the performance of PENTATRAP.

CONTENTS

LIST OF FIGURES

LIST OF TABLES

1 INTRODUCTION

Physicists investigate nature by trying to understand fundamental observations: Why does an apple fall from a tree? How are the elements formed and why is there solar abundance as it is? Why is there such a imbalance between mater and antimatter? The goal is to develop a model which allows to explain and predict fundamental forces.

The Standard Model is currently the best and well-tested model which explains the fundamental interactions of the elementary particles which forms our world. However it is not complete. Several phenomena and questions are yet not explained and answered, respectively, such as:

1. A unified theory of the general relativity theory and the quantum world,
2. the baryon / anti-baryon asymmetry abundance in the observable universe,
3. the evidence that neutrinos are massive particles,
4. and the experimental hints of dark energy and dark matter.

This thesis deals partly with the issue about massive neutrinos. The neutrino is a fundamental particle postulated in 1930 by Pauli to explain the continuous energy spectrum of emitted electrons by a β-decay. In the process a neutron n is converted into a proton p, an electron e^-, and an anti-electron-neutrino $\overline{\nu}_e$:

$$n \rightarrow p + e^- + \overline{\nu}_e. \tag{1.1}$$

However, neutrinos interact very weakly with ordinary matter. Thus, the practical direct observation of the decay products is missing the energy taken away by the neutrino. Although very unprobable, it is possible that neutrinos interact with matter: The first direct experimental proof of the existence of the neutrino happend 20 years after its postulation by observing the inverse β decay [1]. In this process a neutrino is captured by a proton resulting in a neutron and a positron:

$$\nu_e + p \rightarrow e^+ + n. \tag{1.2}$$

Later neutrinos were introduced in the Standard Model as massless leptonic fermions with spin 1/2. They are electrically neutral and interact through the weak interaction and gravity. It was shown that there must be three different types of neutrinos [2], which are the three flavor types: ν_e, ν_μ, ν_τ.

The discovery of neutrino oscillations, [3, 4], shows that the Standard Model description of the neutrino is incomplete. In fact, neutrino oscillation can be explained by massive neutrinos: For massive neutrinos, the flavor eigenstates $\nu_{e,\mu,\tau}$ are connected to the mass eigenstates $\nu_{1,2,3}$ via the Pontecorvo-Maki-Nakagawa-Sakata (PMNS) matrix U [5],

$$\nu_\alpha = \sum_{i=1}^{3} U_{\alpha,i}\nu_i \quad \text{with} \quad \alpha = (e, \mu, \tau). \tag{1.3}$$

The probability of the transition [6–8] between two flavor eigenstates α and β after the neutrino path length L is

$$P^{\text{vac}}_{\alpha\beta} = \delta_{\alpha\beta} - 4\sum_{i<j} U_{\alpha i}U_{\alpha j}U_{\beta i}U_{\beta j}\sin^2\left(\frac{\Delta m^2_{ij}}{4E}L\right), \tag{1.4}$$

where $\Delta m^2_{ij} = m^2_i - m^2_j$ is the difference of the squared masses of the mass eigenstates, $\langle \nu_\alpha | \nu_\beta \rangle = \delta_{\alpha\beta}$ is the orthogonality relation and E is the neutrino energy. It follows that with the observed finite probability of flavor oscillations at least two neutrino masses are non zero. Moreover it is already possible to determine the absolute squared neutrino mass differences from neutrino oscillation experiments. By considering the squared neutrino mass differences two orderings of the neutrino mass eigenstates are possible: The normal ordering with $m_1 < m_2 < m_3$ and the inverted ordering with $m_3 < m_1 < m_2$, see fig. 1.1 . The absolute squared mass difference Δm^2_{21} is in both ordering equal while for the normal ordering Δm^2_{31} and Δm^2_{32} for the inverted ordering have different sign but equal in value within the error [9],

$$\Delta m^2_{21} = (7.50^{+0.19}_{-0.17}) \cdot 10^{-5}(\text{eV}/c^2)^2, \tag{1.5}$$
$$\Delta m^2_{31} = (2.524^{+0.039}_{-0.040}) \cdot 10^{-3}(\text{eV}/c^2)^2, \tag{1.6}$$
$$\Delta m^2_{32} = (-2.514^{+0.038}_{-0.041}) \cdot 10^{-3}(\text{eV}/c^2)^2. \tag{1.7}$$

The absolute scale is also not accessible by neutrino oscillation experiments since the oscillations involve only differences of the squared masses.

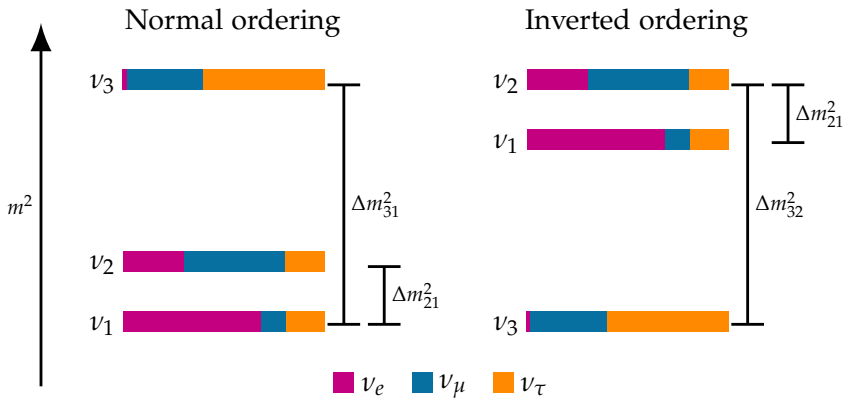

Figure 1.1: Shown is a common diagram of the neutrino mass hierarchy with its two cases: The normal ordering (left) and the inverted ordering (right). The single vertical bars symbolize the mass eigenstates $\nu_{1,2,3}$. The color code in the bars shows the relation (see eq. [1.3]) of the single values of the of the mass eigenstates to the flavor eigenstates $\nu_{e,\mu,\tau}$, however without uncertainties.

Cosmological surveys yield upper mass limits for the sum of the mass eigenstates $\sum m_\nu$ in the order of $10^{-1}\,\text{eV}c^2$ [10]. However these cosmological measurements are inherently model-dependent. Thus model independent measurements are needed to verify the conclusions or to proof/dis-proof the underlying model assumptions.

1.0.1 *How can the electron-neutrino mass be measured when it is a mixing of three mass eigenstates?*

The single mass eigenstates $\nu_{1,2,3}$ are currently not experimentally resolvable. The direct neutrino mass experiments which exploit a β-decay, are only sensitive to the so-called effective (anti-)electron neutrino mass m_β [11],

$$m_\beta = \left[\sum_i |U_{ei}|^2 m_i^2\right]^{\frac{1}{2}} = \left[0.67m_1^2 + 0.29m_2^2 + 0.02m_3^2\right]^{\frac{1}{2}}, \tag{1.8}$$

where the numbers are from the current evaluation of the PMNS-Matrix [9] without stating the errors. The measurement of m_β will give a first estimate of the offset from zero of the neutrino mass eigenstates.

1.0.2 *Current status of the model independent neutrino mass determination*

All relevant non-cosmological measurements of the neutrino mass are based on the investigation of a β-decay. Depending on the type of β-decay it is distinguished between a measurement of the anti-electron neutrino mass or the electron neutrino mass. Current model independent values are,

$$m_{\beta^-} < 2\,\mathrm{eV}/c^2 \quad (95\ \%\ \text{confident level}), \tag{1.9}$$

$$m_{\beta^+} < 225\,\mathrm{eV}/c^2 \quad (95\ \%\ \text{confident level}), \tag{1.10}$$

where the m_{β^-} value [12] is a combination of the result of the Troitsk experiment [13] and the Mainz experiment [14] on tritium β spectroscopy. While the m_{β^+} value comes from the spectroscopy of X-rays emitted in the electron-capture decay of ^{163}Ho [15]. The current values of the upper limits of the anti-electron neutrino or electron-neutrino mass, respectively, need to be improved to get near the limits ($\approx 10^{-1}\,\mathrm{eV}/c^2$) obtained by the cosmological surveys [10]. While the general measurement idea in both cases is the same, the experimental methods differ significantly. Thus, if both measurements yield the same result they would prove the mass equivalence between neutrino and anti-neutrino while in the other case it may open the discussion about possible violation of CPT symmetry or the search for unknown systematics in the experimental methods.

1.1 HOW AN ATOMIC MASS MEASUREMENT CONTRIBUTE TO NEUTRINO PHYSICS RESEARCH?

Since neutrinos are only weakly interacting particles, its properties are mostly determined by indirect measurement methods. Therefore most neutrino mass experiments are looking for the missing energy in weak decays: β-decays or electron capture processes. The β-decay can be modeled as a three-body interaction between the nucleus, an electron, and the neutrino. The electron, its direction and energy can be nowadays detected with high efficiency, which makes it possible to extract the neutrino rest mass from the endpoint of a β-decay spectrum. More details to this kind of endpoint experiments and a the role of atomic mass measurements for neutrino physics can be found in chapter 3 of this thesis. If the maximum endpoint energy is compared to the total released energy of the decay the neutrino rest mass is the difference between those values. The total released energy can be measured by measuring the mass difference between the mother and daughter

atom. With the use of $E = mc^2$, the total released energy can be determined. This mass difference can be precisely measured by Penning-trap mass spectrometers.

1.2 THE HIGH-PRECISION PENNING-TRAP MASS SPECTROMETER PENTATRAP

This thesis contribute to the improvement of the upper limit of the effective neutrino mass with experimental work on atomic mass measurements. PENTATRAP is a novel Penning-trap mass spectrometer which is specialized on spectrometry of mid- to heavy stable nuclei employing highly charged ions. It is ideal to study cases like the ^{163}Ho to ^{163}Dy mass difference which is subject to the electron-neutrino mass m_{β^+} determination. After a short introduction to the basic techniques of Penning-trap mass spectrometry in chapter 2, a first direct measurement of the ^{163}Ho to ^{163}Dy mass difference at the already long existing Penning-trap mass spectrometer SHIPTRAP is discussed in chapter 3. Afterwards, in chapter 4, the new PENTATRAP setup is presented. Followed by a description of the experimental setup, the commissioning status in chapter 5 is provided. The first proof of principle measurement of the two isotopes of xenon, ^{131}Xe and ^{132}Xe, which masses are already known to a relative mass precision of 10^{-10} are shown in chapter 6.

2

THEORY AND EXPERIMENTAL STANDARD TECHNIQUES OF PENNING-TRAP MASS SPECTROMETRY

This chapter will discuss the resulting motion of a charged particle which is trapped in a superposition of a static electric and a static magnetic field. The resulting motion can be split up into three harmonic eigenmotions if a superposition of a homogeneous magnetic field and a quadropolar electrical field is chosen. This configuration is known as Penning trap after Frans Michel Penning who was the first who superimpose an electric and a magnetic field[16]. The first one who used such a configuration to store particles was Dehmelt [17].

From the confined ion with charge q in a magnetic field B_0 the cyclotron frequency

$$\nu_c = \frac{1}{2\pi}\frac{q}{m}B_0 \tag{2.1}$$

is measured to determine the mass m by a frequency measurement. This chapter gives an introduction into the theory how the free cyclotron frequency can be measured in a Penning-trap mass spectrometer as much as it is needed to understand this thesis which is far away from being a complete description.

2.1 A SINGLE ION IN A PENNING TRAP

2.1.1 *Motion of a single ion in a Penning trap*

The forces of electromagnetic fields, $\vec{B}$ and $\vec{E}$ on charged particles are described by the Lorenz force:

$$\vec{F}_L = q(\vec{E} + \vec{v} \times \vec{B}). \tag{2.2}$$

Solving this equation with a quadrupolar electrical field which strength is given by a voltage V_0 and a constant C_2:

$$\vec{E} = -\vec{\nabla}\Phi = V_0 C_2 \begin{bmatrix} x \\ y \\ -2z \end{bmatrix}, \tag{2.3}$$

and a homogeneous magnetic field $\vec{B} = B_0[0,0,1]$ yields the equation of a motion for a charged particle in a Penning trap. Using a cylindrical symmetric system results in the equations

$$x(t) = \hat{\rho}_+ \cos(\omega_+ t + \phi_+) + \hat{\rho}_- \cos(\omega_- t + \phi_-) \tag{2.4}$$
$$y(t) = -\hat{\rho}_+ \sin(\omega_+ t + \phi_+) - \hat{\rho}_- \sin(\omega_- t + \phi_-) \tag{2.5}$$
$$z(t) = \hat{z} \cos(\omega_z t + \phi_z) \tag{2.6}$$

with their phases $\phi_{-,z,+}$, amplitudes $\hat{\rho}_{-,+}$, $\hat{z}$, and three characteristic eigenfrequencies:

$$\omega_{\pm} = \frac{1}{2}\left(\omega_c \pm \sqrt{\omega_c^2 - 2\omega_z^2}\right) \tag{2.7}$$

$$\omega_z = \sqrt{\frac{2qV_0C_2}{m}}, \tag{2.8}$$

which are called as follows: ω_- magnetron frequency, ω_z axial frequency, ω_+ modified cyclotron frequency. The resulting three eigenmotions are showing in fig. 2.1.

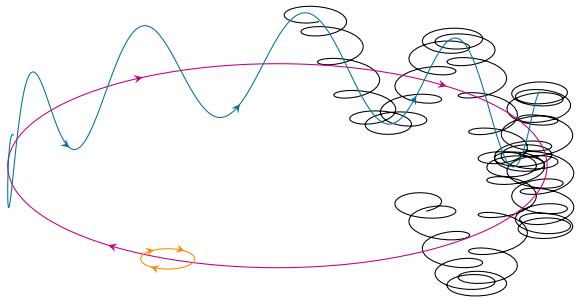

Figure 2.1: Shown is a not to scale single ion motion in a Penning trap and its respective eigenmotions. The black line shows the complete motion. The blue line shows the axial motion, the purple line the magnetron motion and the orange line the modified cyclotron motion, respectively.

For the existence of eigenfrequencies of periodic eigenmotions the trapping condition

$$\omega_z \leq \frac{\omega_c}{\sqrt{2}} \tag{2.9}$$

has to be fulfilled. This can also be expressed as:

$$0 > qV_0C_2 \tag{2.10}$$

$$B_0 > \sqrt{2\frac{m}{q}V_0C_2}. \tag{2.11}$$

The eigenfrequencies can be ordered according to:

$$\omega_- \ll \omega_z \ll \omega_+ < \omega_c, \tag{2.12}$$

and are related via:

$$\omega_z^2 = 2\omega_+\omega_-. \tag{2.13}$$

Furthermore, in an ideal Penning trap, the following frequency relations are given:

$$\omega_c = \omega_+ + \omega_-, \tag{2.14}$$

$$\omega_c^2 = \omega_+^2 + \omega_z^2 + \omega_-^2. \tag{2.15}$$

The later one is refereed to as invariance theorem [18] since it is also valid in a non-ideal Penning trap, e.g. when electric and magnetic fields are misaligned.

2.1.2 *Experimental generation of the electrical quadrupole field*

In order to generate an electrical field, one applies typically a voltage to some suitable electrode configuration. In the case of the Penning-trap, the obvious choice is to design electrodes which follow the equipotential lines of the electric quadrupole field. In the case of the PENTATRAP experiment and further discussed in this chapter, another configuration is chosen: The cylindrical Penning trap introduced by G. Gabrielse [19]. This kind of Penning trap approximates the electric quadrupole field with a stack of cylindrical electrodes which are mirror symmetric at the middle of the ring electrode, see fig. 2.2. Each kind of electrode has a specific length-to-diameter ratio with a defined voltage to approximate to a sufficient order an electric quadrupole field at the position of the ion.

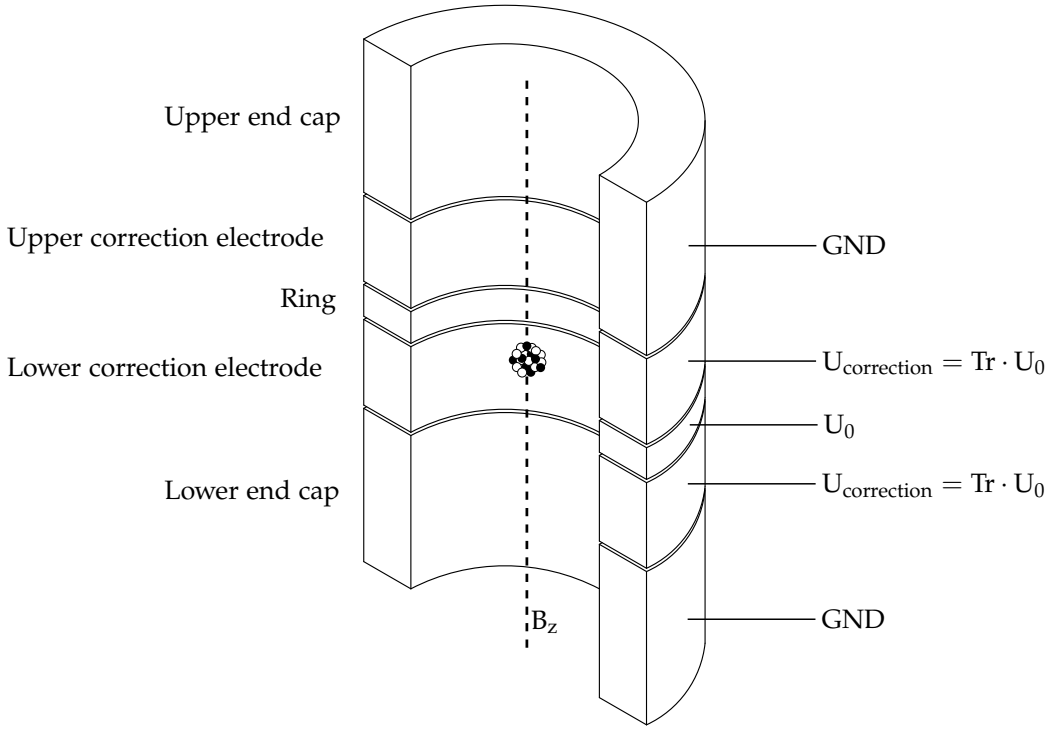

Figure 2.2: Vertical cut through a schematic cylindrical trap with five electrodes as it is used at PENTATRAP.

2.1.3 *Energy of a single ion in a Penning trap*

In an ideal Penning-trap, the eigenmotions are decoupled from each other. A trapped single spinless particle can be described by the Hamiltonian

$$H = \hbar\omega_+ \left(n_+ + \frac{1}{2}\right) + \hbar\omega_z \left(n_z + \frac{1}{2}\right) - \hbar\omega_- \left(n_- + \frac{1}{2}\right), \tag{2.16}$$

with $n_{+,-,z}$ being the number of quanta in the single modes. Due to the metastability of the magnetron motion, the energy decreases with an increase of the magnetron quanta n_-. If the magnetron mode is completely decoupled from the environment the remaining loss mechanism is the loss radiation. For an $^{132}Xe^{17+}$ ion in the PENTATRAP setup with a magnetron

frequency of $\omega_- = 2\pi \cdot 8360$ Hz the typical cooling time constant for this process is [20]:

$$\gamma_- = \frac{2q^2}{3mc^3}\omega_-^2 \frac{\omega_-}{\omega_+ - \omega_-} \Leftrightarrow \tau_- = \frac{1}{\gamma_-} \approx 6 \cdot 10^{29}\text{yr} \tag{2.17}$$

which can be neglected in the case of mass measurement applications.

2.2 MANIPULATION OF ION MOTIONS IN A PENNING TRAP

As seen in the last section the frequencies can be fixed by an ideal quadrupolar electric field and a static magnetic field. The amplitudes $\hat{\rho}_+, \hat{\rho}_-, \hat{\rho}_z$ instead can be manipulated by applying radio-frequency (RF) fields.

DIPOLAR EXCITATION: A dipolar excitation which is resonant with one eigenfrequency will increase the energy and thus the amplitude of the motion. Also, the phase of the motion will adjust to the irradiated frequency.

QUADRUPOLAR EXCITATION: An electric quadrupolar excitation, e.g. in the x-z plane:

$$\vec{F}_q = qA_{rf} \begin{bmatrix} z \\ 0 \\ x \end{bmatrix} \cos(\omega_{rf} t + \phi_{rf}), \tag{2.18}$$

at a frequency of ω_{rf} corresponding to the sum or difference of the frequencies of two eigenmotions will result in a coupling of the respective motions. The motional energy will undergo a Rabi oscillation where the energy will be transferred periodically from one motion to the other. Two cases have to be considered:

a) In the case of $\omega_+ + \omega_z$, $\omega_+ - \omega_-$ (due its opposite sign in the magnetron energy) additional energy will be put into the system.

b) In the opposite case $\omega_+ - \omega_z$, $\omega_+ + \omega_-$ the energy is periodically exchanged between the coupled motions.

The larger coupling frequency of this two possible cases is commonly called upper sideband while the lower one is called lower sideband.

2.3 PRINCIPLES OF A MASS MEASUREMENT IN A PENNING TRAP

A mass measurement of an ion with charge-to-mass ratio q/m is based on frequency measurement of the free cyclotron frequency, see Eq. 2.1. The free cyclotron frequency can be obtained from the eigenfrequencies via the relations Eq. 2.14 or Eq. 2.15. The choice which one to use depends typically on the experimental conditions:

TYPICAL USE OF EQ. 2.14 In the case of $\omega_c = \omega_+ + \omega_-$, one doesn't need to measure the axial frequency. This is especially of importance for online mass spectrometers which are normally dealing with nuclei of short lifetimes. Here one has to balance the error from the systematic correction vs. the statistical error. Since these experiments are typically limited by statistics and the applications of the results require at most relative uncertainties in the 10^{-9} level, they are built such that a measurement of the axial frequency

is not required. This approach results in a different kind of measurement technique compared to offline mass spectrometers. The Phase-Imaging Ion-Cyclotron-Resonance (PI-ICR) detection technique based on eq. 2.14 is used to obtain ω_c is discussed in chapter 3 in the context with the online mass spectrometer SHIPTRAP.

TYPICAL USE OF EQ. 2.15 The equation $\omega_c^2 = \omega_+^2 + \omega_z^2 + \omega_-^2$, also known as Brown-Gabrielse invariance theorem [18], has the advantage that it is still valid for some field imperfections, misalignment between the electric and magnetic field axis and ellipticity of the electric field. This equation is mainly used in offline experiments with long storage times which allow measuring all three frequencies accurately enough. This detection method will be discussed in chapter 4 in the context of PENTATRAP.

2.3.1 *The (atomic) mass obtained from the free cyclotron frequency and how to determine a mass difference*

To extract the mass from a free cyclotron frequency measurement the parameter $q = e \cdot N$, with e as elementary charge, and B_0 need to be known too. The current experimental relative uncertainty on the elementary charge e is $6.1 \cdot 10^{-9}$ [21]. But the most critical parameter at modern Penning-trap experiments is the knowledge about B_0. To overcome this limitation, a relative measurement is done. In the same trap a sequential measurement of the free cyclotron frequencies of the two ions is carried out. In the best case, one of the ions will be $^{12}C^{n+}$ since the mass of ^{12}C defines the atomic mass standard: $1u = 1/12m(^{12}C)$. In a relative measurement e and B_0 will drop out, if they are constant in time. In many modern Penning-trap mass spectrometer experiments the magnetic-field-drift during one measurement cycle is the dominant systematic error. To reduce the effect of the drifting magnetic field a new measurement scheme is proposed for PENTATRAP and discussed in chapter 4.

CORRECTION OF THE MISSING ELECTRONS To finally evaluate the mass difference $M_{atom,\Delta}$ for neutral atoms one has to account for the missing electrons with mass m_e and their binding energies in each of the compared systems.

$$M_{atom,\Delta} = (M_{\text{ion, 1}} + N_1 \cdot m_e - E_{\text{binding, 1}}) - (M_{\text{ion, 2}} + N_2 \cdot m_e - E_{\text{binding, 2}}), \quad (2.19)$$

where $M_{\text{ion, i}}$ is the measured mass of the ion and $E_{\text{binding, i}}$ the total missing binding energy.

THE MASS DIFFERENCE FROM THE MASS RATIO To obtain the mass difference from the mass ratio the knowledge of one of the two masses is needed,

$$\begin{aligned} M_{atom,\Delta} &= m_1 - m_2 \\ &= m_2 \cdot \frac{m_1}{m_2} - m_2 \\ &= (R-1)m_2, \end{aligned} \quad (2.20)$$

where $R = \frac{m_1}{m_2}$. The relative uncertainty in the mass difference is given by

$$\frac{\delta(M_{atom,\Delta})}{M_{atom,\Delta}} = \sqrt{\left(\frac{\delta m_2}{m_2}\right)^2 + \left(\frac{\delta R}{(R-1)}\right)^2}. \tag{2.21}$$

In order to minimize systematic uncertainties it is best to choose R as close as possible to 1 in a mass ratio measurement. However, due to the second summand in eq. [2.20] the requirement of the uncertainty in R is increasing if one wants to maintain the uncertainty in the mass difference measurement.As in modern Penning-trap experiment it becomes possible to choose easier R due to access to higher charges this consideration becomes more important.

2.4 DETECTION OF ION MOTIONS IN A PENNING TRAP

2.4.1 *Effective electrode distance*

To account for different trap geometries the effective electrode distance D of a trap electrode was introduced [22]. It is the distance between the plates of an effective parallel plate capacitor, which produces the same field strength E_z^p at the position of the ion as the real electrode does. The field strength of a parallel plate capacitor with applied voltage V is

$$E_z^p = \frac{V}{D}. \tag{2.22}$$

The field strength E_z^{el} of the real electrode can be calculated or simulated. The effective electrode distance can then be calculated as

$$D = \frac{V}{E_z^{el}}, \tag{2.23}$$

and in the case of PENTATRAP it is typically in the range of 10 mm to 30 mm. Note, at PENTATRAP the size of the trap is much smaller than the wavelength of the applied and detected RF signal.

2.4.2 *Detection circuit*

In this subsection, the detection of the axial motion will serve as an example since the direct detection of the other motions can be realized in a similar way. If the ion oscillates in an effective parallel plate capacitor it will induce an image charge current I_{img} in the electrodes. Due to parasitic capacitances in the experimental setup, which are in the order of a few pF, the directly detectable signal strength is limited. To overcome this limitation an inductor L is connected in parallel to the parasitic capacitances to form a resonant circuit, see fig. 2.3. This resonator will have a high impedance on its resonance frequency. If the ion oscillates on the same frequency the voltage-drop of the induced signal is increased compared to a non-resonant detection. After amplification of the induced signal, a Fourier transform of the signal is done and the ion frequency can be extracted.

COOLING VIA COUPLING TO A RESONATOR Due to the energy loss in the resonator the ion thermalizes with the resonator with the time given by the cooling time constant τ:

$$\tau = \frac{mD^2}{q^2 R_p}, \tag{2.24}$$

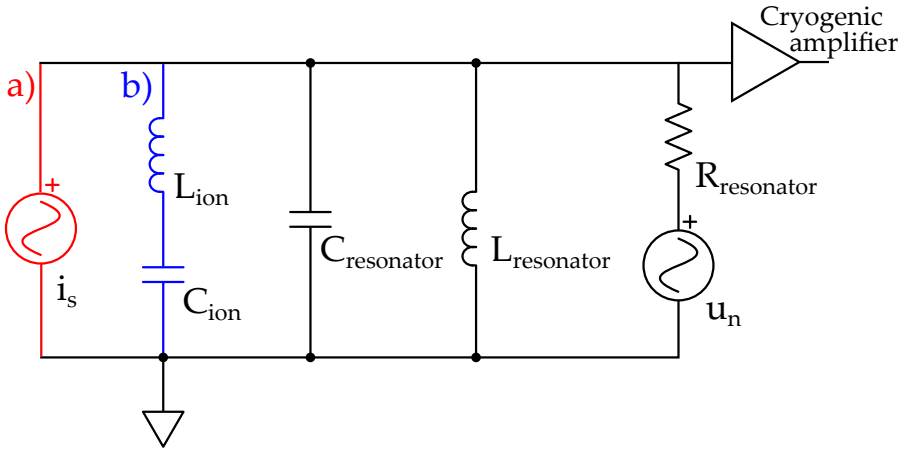

Figure 2.3: Schematic detection circuit in the case of a thermal "hot ion" ($T \approx 1000\,\mathrm{K}$) a) and in the case of a thermalized ion ($T \approx 4\,\mathrm{K}$) b). The hot ion will induce an image charge current into the electrodes causing a voltage drop. This voltage drop is maximal when the ion's oscillation frequency is in resonance with the eigenfrequency of the resonator. In the case of a thermalized ion, the ion can be described with a series LC circuit which causes a short of the noise u_n on the oscillating frequency of the ion.

where R_p is the effective parallel resistance of the resonator. On resonance R_p is

$$R_p = Q\omega_{res}L, \tag{2.25}$$

where Q is the quality factor and L the inductance of the resonator. With a quadrupolar excitation on the suitable sideband (see. sec. 2.2) all motions can be cooled by coupling to a motion which is resonant to a tank circuit. In this case, the reachable temperature of the sideband cooled motion T_s is determined by the temperature of the tank circuit T_t and the frequency ratio of the motion which is resonant with the tank circuit ω_{res} and the sideband cooled motion ω_s:

$$T_s = \frac{\omega_s}{\omega_{res}} \cdot T_t. \tag{2.26}$$

In order to reach an as low particle temperature as possible it is best to use a cyclotron resonator and to sideband cool the other motions.

DIP DETECTION In case the ion is thermalized with the coupled resonator, the ion shortcuts the noise u_n at its oscillating frequency. A so-called dip appears in the frequency spectrum. The ion can be described as a series resonator, see fig. 2.3. The analytical function to describe the dip is [23]:

$$A_{dip}(\omega) = A_0 \frac{\omega^2\omega_{res}^2(\frac{\omega^2}{\omega_z^2}-1)^2}{\omega^2\omega_{res}^2(\frac{\omega^2}{\omega_z^2}-1)^2 + \frac{(\omega^2\omega_{res} - Q\tau(\omega-\omega_{res})(\omega+\omega_{res})(\omega-\omega_z))^2}{\tau^2\omega_z^4}}, \tag{2.27}$$

where ω_z is the ion's axial oscillation frequency and A_0 the amplitude. The width of the dip in Hz can be expressed as

$$\gamma = \frac{1}{2\pi \cdot \tau}. \tag{2.28}$$

If a small number of ions n are stored so that the direct Coulomb interaction is negligible the width scales linearly with n, thus $\gamma \to n \cdot \gamma$. In the case the ion is off-resonant to the resonator a dispersive response is observed, see fig. 2.4. With adding an offset A_{off} and converting to a logarithmic scale eq.

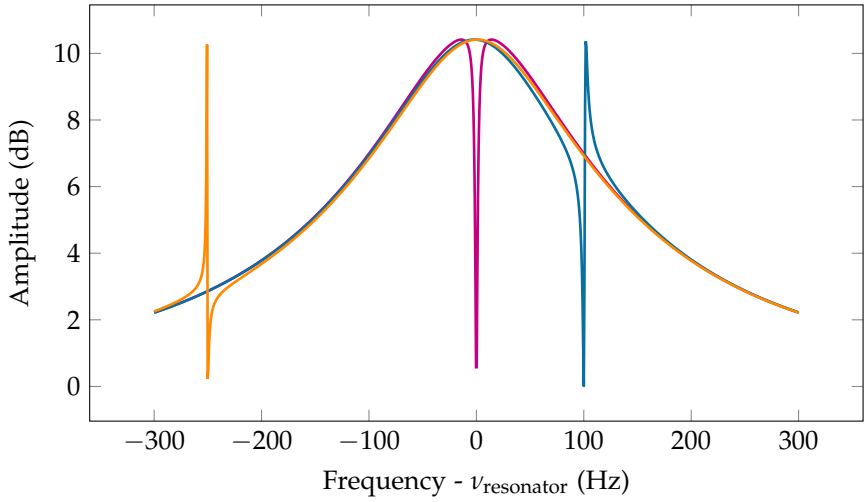

Figure 2.4: Full solution of the interaction of the ion with the detection system for three different cases: (i) The particle frequency is same as the detector frequency (purple), (ii) the particle frequency is 100 Hz higher (blue) or (iii) 250 Hz lower (orange) than the detector frequency. The quality factor of the resonator in this example is 5000 and the dip width of all dips 5 Hz.

[2.27] is used as fitting function for the measured dips,

$$A_{FFT}(\omega) = 10\log_{10}(A_{dip}(\omega) + A_{\text{off}}) + th \cdot (\omega - \omega_{res}). \tag{2.29}$$

Here the last therm: $th \cdot (\omega - \omega_{res})$ is a approximation for the transfer function of the amplifier. Where th is typical < 1, see [23] for details.

DOUBLE DIP DETECTION If one radial motion is coupled to the axial motion with an quadrupolar RF-excitation ν_{rf} (see. eq. [2.18]) and both motions are thermalized, a double dip appears in the axial frequency spectrum, see fig. 2.5. The analytical function to describe the double dip is [24],

$$A_{double}(\omega) = A_0 \cdot \text{Re}\left(-1 \cdot \frac{A}{B + C}\right), \tag{2.30}$$

where A, B, C are,

$$A = i\tau_l\tau_r\omega(\omega - \omega_l)(\omega + \omega_l)(\omega - \omega_r)(\omega + \omega_r)\omega_{res}, \tag{2.31}$$

$$B = \omega(\tau_r\omega(-\omega^2 + \omega_r^2) - i\tau_1(\omega - \omega_l)(\omega + \omega_l)(\omega(-i + \tau_r\omega) \tag{2.32}$$

$$- \tau_r\omega_r^2))\omega_{res}, \tag{2.33}$$

$$C = Q\tau_l\tau_r(\omega - \omega_l)(\omega + \omega_l)(\omega - \omega_r)(\omega + \omega_r)(\omega - \omega_{res})(\omega + \omega_{res}). \tag{2.34}$$

Here the indexes l or r denote the left or the right dip. To fit a double dip the same eq. [2.29] as the one to fit the single dip is used, but $A_{dip}(\omega)$ is replaced with $A_{double}(\omega)$.

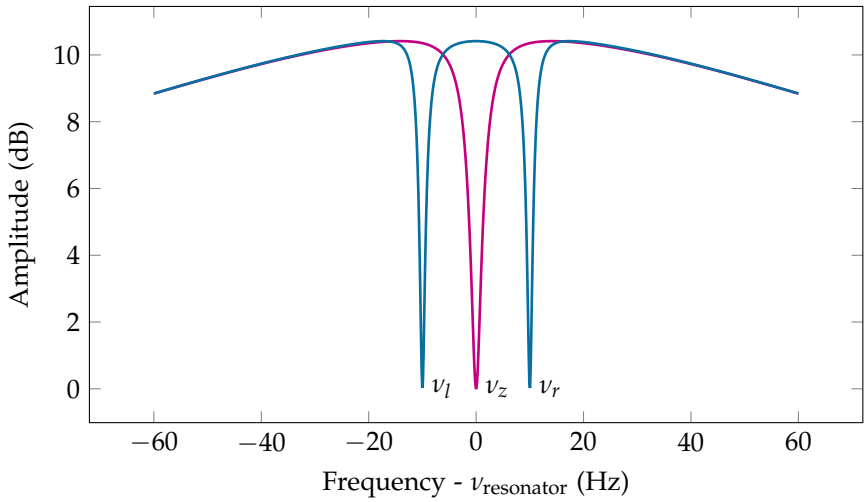

Figure 2.5: Plot of the dip and double dip function, eq. [2.27] and eq. [2.30], respectively. The single dip has a width of 5 Hz while the double dips have widths of 2.5 Hz each. In this example the resonator has a quality factor of 5000.

With a previously measured axial frequency ν_z it is possible to calculate the magnetron respectively the modified cyclotron frequency from the frequencies of the right ν_r and left ν_l double dip,

$$\nu_- = \nu_{rf} + \nu_z - \nu_l - \nu_r, \tag{2.35}$$

$$\nu_+ = \nu_{rf} - \nu_z + \nu_l + \nu_r. \tag{2.36}$$

If the coupling is resonant i.e. $\nu_{rf} = \nu_\pm \mp \nu_z$, the splitting in frequency of the two dips is exactly the rabi frequency Ω.

$$\Omega = \nu_r - \nu_l. \tag{2.37}$$

For an off resonant drive, in the example of a magnetron double dip,

$$\delta = \nu_{rf} - (\nu_z + \nu_-), \tag{2.38}$$

the Rabi frequency gets modified

$$\Omega = \sqrt{\Omega_0^2 + \delta^2}, \tag{2.39}$$

where Ω_0 is the Rabi frequency on resonance being proportional to the amplitude of the driving E-field component. Depending on the difference of the drive to the resonant frequency δ the frequency of the left dip ν_l and of the right dip ν_r are shifted,

$$\nu_{l,r} = \nu_z - \frac{1}{2}\left(\delta \pm \sqrt{\Omega_0^2 + \delta^2}\right), \tag{2.40}$$

as shown in fig. 2.6.

2.5 FIELD IMPERFECTIONS AND HOW TO TUNE AND TO USE THEM

With the experimental realization of a quadrupolar electric field (see sec. 2.1.2) and a homogenous magnetic field also some deviations from the ideal

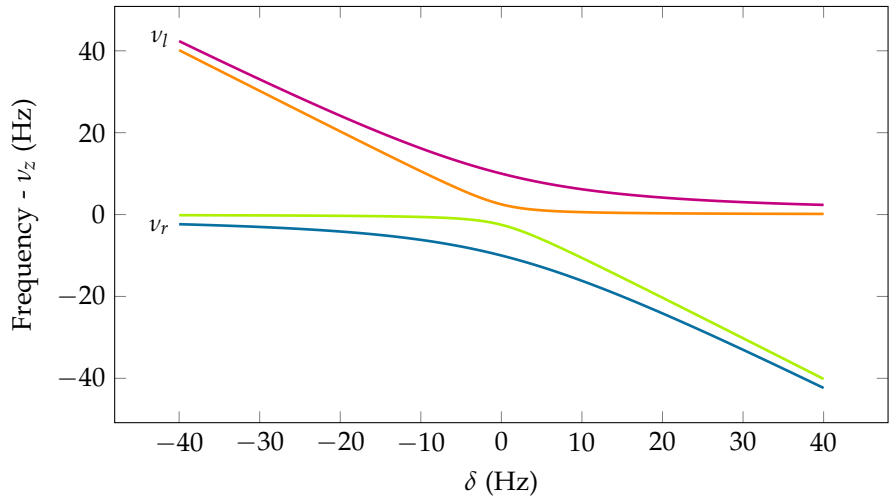

Figure 2.6: Shown are the frequency shifts of ν_l, ν_r for the magnetron double dip as function of the detuing δ. The purple and blue colored curves belong to the case where Ω_0 is 20 Hz, orange and green curves belong to the case where Ω_0 is 5 Hz.

theoretical fields will occur. Approximating the quadrupolar electric field at the position of the ion in the case of a cylindrical Penning trap means that the ion motion is altered and not perfectly harmonic. Even in a hyperbolic Penning trap the electrical field is not perfect due manufacturing tolerances and misalignment in the setup.

2.5.1 *Description of the real electrical field*

The potential in the trap needs to be a solution of the Laplace equation $\nabla^2\phi(\rho,z) = 0$ with the given boundary conditions by the trap geometry and the applied voltages. This field can be written in cylindrical coordinates as a Taylor expansion as proposed in [25]. At the mean position of the ion (aka. trap center) the potential can be described by

$$\phi(\rho,z) = \sum_{j=0}^{inf}\sum_{i=0}^{j}\frac{1}{i!(j-i)!}\cdot\frac{\partial^j\phi}{\partial\rho^i\partial z^{j-i}}\bigg|_{(0,0)}\cdot\rho^i z^{j-i}. \tag{2.41}$$

The Taylor coefficients $\frac{1}{i!(j-i)!}\cdot\frac{\partial^j\phi}{\partial\rho^i\partial z^{j-i}}\Big|_{(0,0)}$ can be normalized to U_0 and substituted in Eq. 2.41 as $c_{i,j-i}$, which results in

$$\phi(\rho,z) = U_0\sum_{j=0}^{inf}\sum_{i=0}^{j}c_{i,j-i}\cdot\rho^i z^{j-i}. \tag{2.42}$$

With the requirement of solving the Laplace equation the potential can be described completely with the potential on the symmetry axis. Therefore, the coefficients $c_{i,j-i}$ can be written as a function of the pure axial coefficients

$$c_j \equiv c_{0,j} = \frac{1}{U_0}\frac{1}{j!}\cdot\frac{\partial^j\phi}{\partial z^j}\bigg|_{(0,0)}, \tag{2.43}$$

which in turn are functions of the electrode geometry and the applied voltage. Thus $c_{i,j-i}$ can be written as

$$c_{i,j-i} = (-1)^{i/2} \frac{j!}{(j-i)! \left(\frac{i}{2}!\right)^2 2^i} \cdot c_j. \tag{2.44}$$

Furthermore, using Eq. 2.44 in Eq. 2.42 the trap potential can be written as

$$\begin{aligned}\phi(\rho, z) \cdot U_0^{-1} = c_0 & \\ + c_2 & \left(z^2 - \frac{1}{2}\rho^2\right) \\ + c_4 & \left(z^4 - 3\rho^2 z^2 + \frac{3}{8}\rho^4\right) \\ + c_6 & \left(z^2 - \frac{15}{2}\rho^2 z^4 + \frac{45}{8}\rho^4 z^2 - \frac{5}{16}\rho^6\right) \\ + & \ldots .\end{aligned}$$

The potential is expanded in the practical most important coefficients. While c_2 is the parameter for the harmonic potential, c_4 and c_6 are the first anharmonic terms which needs to be considered, in the experimental work, see chapter 5.

2.5.1.1 *Tuning ratio*

In a five electrode trap, the tuning ratio is defined as the ratio between the voltage applied to the ring electrode and the voltage applied to the correction electrodes where the leading an-harmonic terms c_4 and c_6 vanish:

$$\mathrm{Tr}\big|_{c_4,c_6=0} = \frac{U_c}{U_0}. \tag{2.45}$$

By detuning the tuning ratio determined c_4 and c_6 coefficients can be adjusted which can be used e.g. for amplitude measurements.

$$\mathrm{Tr}\big|_{c_4,c_6} = e_j + \mathrm{Tr} d_j \text{ with} \tag{2.46}$$

$$d_j = \frac{\partial c_j}{\partial T}. \tag{2.47}$$

The d_j coefficients are a measure for the change of the c_j coefficients to the applied voltage at a given geometry. A trap with $d_2 = 0$ is called orthogonal. In case of cylindrical Penning traps with more than five electrodes, multiple tuning ratios will appear.

2.5.2 *Frequency shifts due field imperfections*

A complete overview and discussion of frequency shifts due to field imperfections is given in [26] [1]. Here the most important shifts for PENTATRAP are discussed: The detector which is used for the frequency determination is the axial detector. Since most of the time the ion is cooled to $\approx 4\,\mathrm{K}$, i.e. in thermal equilibrium with the resonator, axial frequency and thus cyclotron frequency shifts occur only to c_4 and B_2:

$$\frac{\Delta\omega_z}{\omega_z} = \frac{C_4}{C_2}\frac{3}{4}\left(\hat{z}^2 - 2\hat{\rho}_+^2 - 2\hat{\rho}_-^2\right) \tag{2.48}$$

$$\frac{\Delta\omega_z}{\omega_z} = \frac{B_2}{4B_0}\frac{\omega_+ + \omega_-}{\omega_+\omega_-}\left(\hat{\rho}_-^2\omega_- + \hat{\rho}_+^2\omega_+\right) \tag{2.49}$$

1 C_2 is in [26] in units of $1/d^2$ where d is a characteristic length in hyperbolic traps.

where $\hat{z}$, $\hat{\rho}$ are the amplitudes of the single motions.

3

Q-VALUE OF THE ELECTRON CAPTURE IN ^{163}HO FOR NEUTRINO PHYSICS

Introduction to some aspects of neutrino physics is given in chapter 1. In the following the ECHo experiment on the determination of the neutrino mass will be introduced, which is in a direct competition with the similar project HOLMES [27]. The Q-value of the EC in ^{163}Ho obtained in the ECHo experiment substantially deviated from the evaluated AME 2012 value. This problem motivated the first direct measurement of the mass difference of ^{163}Ho and ^{163}Dy with the Penning-trap mass spectrometer SHIPTRAP.

3.1 NEUTRINO-MASS ENDPOINT EXPERIMENTS

In neutrino mass endpoint experiments the energy spectrum of the released energy in $\beta^{\pm}$-decay is investigated. The β^{+}-decay is a three-body process which involves a nucleon (proton), an incoming electron (electron capture) or outgoing positron and an electron-neutrino, see fig. 3.1. Since all particles which participate in the decay except the neutrino can be detected with high efficiency, the detectable energy misses the part taken away by the neutrino. The endpoint of the measured spectrum corresponds to the case where the neutrino is created at rest. This means that the endpoint differs by the neutrino rest mass from the Q-value, i.e. by the mass difference between the mother and daughter atom. Measuring this difference is the goal of neutrino mass endpoint experiments. In the following this thesis will only focus on the electron capture in holmium experiment, ECHo.

3.1.1 *The electron capture in ^{163}Ho*

One of the most important criteria which a β-transition has to fulfill to suit the experiments on the determination of the neutrino mass is its small Q-value. It should be as small as possible. In fact, the smaller the Q-value the higher the relative contribution of the neutrino mass in the released energy

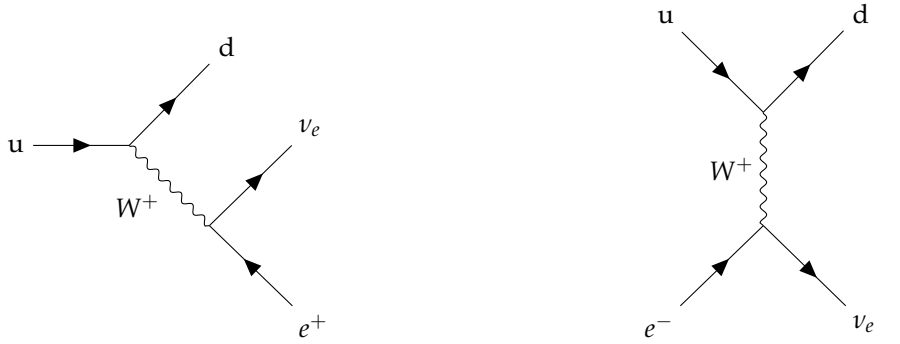

(a) β^{+}-decay (b) Electron capture

Figure 3.1: Feynman diagrams of two weak interaction decays: (a) β^{+} and (b) electron capture decays which produce an electron neutrino.

Element	Q-value	half-life
^{163}Ho	2.833(30) keV	4570 ± 50 y [29]
^{193}Pt	56.63(30) keV	$\approx$50 y [30]

Table 3.1: Elements which are suitable to study the electron neutrino mass in an endpoint experiment.

Element	Q-value	half-life
^{3}H	18.59201(7) keV	12.32 y [31]
^{187}Re	2.470(5) keV	$4.2 \cdot 10^{10}$ y [32]

Table 3.2: Elements which are suitable to study the anti-electron neutrino mass in an endpoint experiment.

of the process. Thus, the signal-to-noise ratio is larger, since more events n are in the interesting region ΔE near the endpoint [28],

$$n(Q, \Delta E) \propto \left(\frac{\Delta E}{Q}\right)^2 . \tag{3.1}$$

Interesting candidates for the determination of the electron neutrino and anti-electron neutrino mass are listed in tab. 3.1 and 3.2, respectively.

Since the EC in ^{163}Ho has the lowest Q-value among EC-transitions to ground state it is the most favorable candidate. Furthermore, the half-life is suitable long for handling samples and low enough to have enough decays per amount of material which can be produced, since it needs to be artificially produced either in a nuclear reactor or at a radioactive ion beam facility.

3.2 THE ECHO EXPERIMENT

The Electron Capture in ^{163}Ho Experiment - ECHo [33] is a collaborative project to improve the upper limit of the electron-neutrino mass via the electron capture in ^{163}Ho. In the final design stage ECHo is planned to reach sub-eV sensitivity on the upper limit of the electron-neutrino mass by analyzing the endpoint of the electron capture spectrum obtained via a calorimetric measurement.

The design of the colorimetric experiment is highly scalable, thus ECHo is divided into different phases, each using a different amount of ^{163}Ho: ECHo-1k with 1 kBq of ^{163}Ho which should reach a neutrino mass sensitivity below $10\,eV/c^2$ and ECHo-100k with 100 kBq of ^{163}Ho which is foreseen to reach a neutrino mass sensitivity below $1\,eV/c^2$.

The collaboration consists of five subgroups with the following tasks:

- Calorimetric measurement
- ^{163}Ho source production and purification
- Background identification and reduction
- Independent measurement of the Q-value of EC in ^{163}Ho
- Theoretical description of the electron capture spectrum.

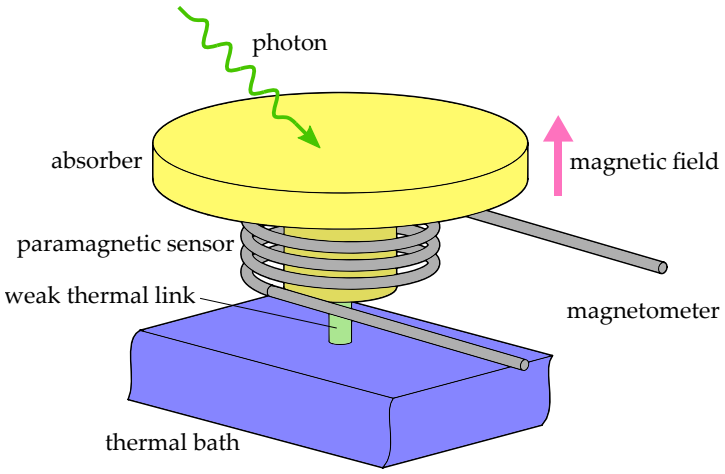

Figure 3.2: Schematic overview of the used metallic magnetic calorimeter.

One of the contributions of this work is the first direct measurement of the difference of ^{163}Ho and ^{163}Dy Q-value by Penning-trap mass spectrometry (see below).

3.2.1 *The MMC-Detector to determine the released energy spectrum*

The ECHo experiment determines the energy spectrum via a metallic magnetic calorimeter measurement at low temperature ($\approx$ mK). The ^{163}Ho is directly implanted in the absorber material of the calorimeter. The latter has a heat capacity C, which has a weak thermal link with a conductance of G to a thermal bath at temperature T, see fig. 3.2. Any energy deposition in the absorber material increases the Temperature by $\Delta T \simeq \frac{E}{C}$. After the increase, the temperature settles back to the value T which can be described by an exponential law with time constant $\tau = \frac{C}{G}$. The measurement is based on the randomization of the magnetic spins induced by the temperature increase. Due to a strong dependency of the magnetization of the sensor on the temperature, any change in the temperature leads to a detectable change of a magnetic flux in a coupled SQUID detector leading to a voltage signal. Thus, any interaction of the MMC-Sensor with a particle increases the temperature and results in a voltage pulse. The implanted energy can be determined from the amplitude of this pulse. A measurement of the energy spectrum after the decay of ^{163}Ho will lead to a signal as shown in fig. 3.3. The peaks in the spectra correspond to the different electronic binding energies of the daughter dysprosium atom where a hole was created by capturing an electron by the parent holmium nucleus. Moreover, a zoom on the endpoint is shown for the two cases in which the electron-neutrino has zero or $1\,eV/c^2$ mass.

3.2.2 *Sensitivity to the electron neutrino mass*

The statistical sensitivity to the neutrino mass of the ECHo experiment with fixed detector parameters depends on the number of detectors and the Q-value of the EC in ^{163}Ho. In Fig. 3.11 the sensitivity is shown for different numbers of detectors and the same observation time of the experiment in dependence on the Q-value. However, at the start of the ECHo-experiment the published Q-value of EC in ^{163}Ho showed a large discrepancy between the

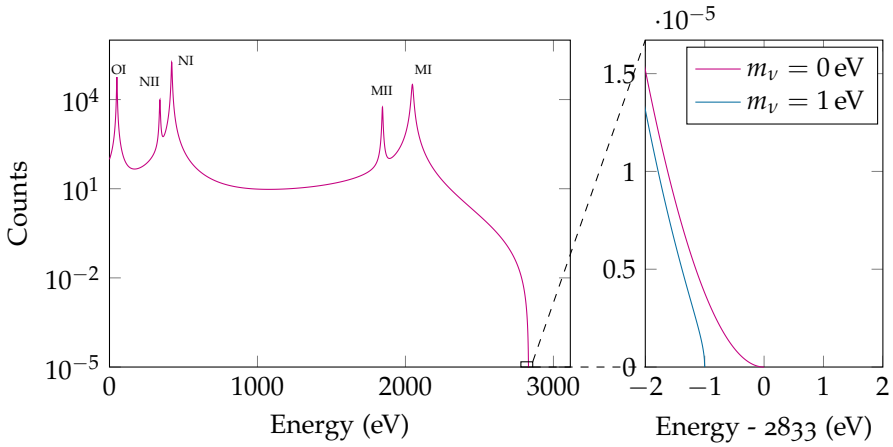

Figure 3.3: Simple simulated dysprosium deexcitation spectrum to illustrate the end point effect for a massless electron-neutrino (purple) and a electron-neutrino (blue) with mass $1\,eV/c^2$.

latest microcalorimetry measurements (see fig. 3.10) and the accepted literature value in the Atomic-Mass Evaluation AME 2012 [34]. In order to solve the discrepancy in the data, a direct Q-value measurement was needed. The first direct measurement of the Q-value was performed with the Penning-trap mass spectrometer SHIPTRAP [35].

3.3 THE PENNING-TRAP MASS SPECTROMETER SHIPTRAP

The SHIPTRAP Penning-trap mass spectrometer is located in Darmstadt, Germany at the GSI Helmholtzzentrum für Schwerionenforschung. It is an online mass spectrometer coupled to the SHIP facility to study heavy ions.

For the measurements discussed in this thesis, an offline laser ion source was used. This source was originally installed to produce carbon cluster ions for calibration measurements at SHIPTRAP [36]. For the ^{163}Ho/^{163}Dy measurement a purified sample with 10^{16} ^{163}Ho atoms was coated onto a $5 \times 5\,\mathrm{mm}^2$ Ti-foil. The ^{163}Ho sample was placed into the laser ion source together with a solid $10 \times 10\,\mathrm{mm}^2$ plate of natural ^{163} Dy. The ^{163}Ho isotope has no natural abundance and the sample had to be produced by irradiating ^{162}Er with neutrons in the reactor at the Institut Laue–Langevin (ILL) [33].

A system of einzel lenses, steerers, and a quadrupole deflector guides the ions from the ion source to the central part of SHIPTRAP: the Penning traps. SHIPTRAP is a double Penning-trap system where two cylindrical Penning traps are placed in two spatially sperated homogenous regions of a 7 T superconducting magnet. The traps are connected via a diaphragm, see fig. 3.4. The first trap is called the preparation trap (PT). An ion bunch coming from the source is loaded into the PT, where it is cooled and cleaned from unwanted species. The cooling achieved by buffer gas, which forces to separate the two traps with a diaphragm in order not contaminate the environment of the measurement trap (MT) trap with unwanted rest gas. After mass separation in the PT, the ions are transferred to MT. There the measurement procedure is applied which ends by ejecting the ions to a position sensitive detector. The measurement procedure is described in the following.

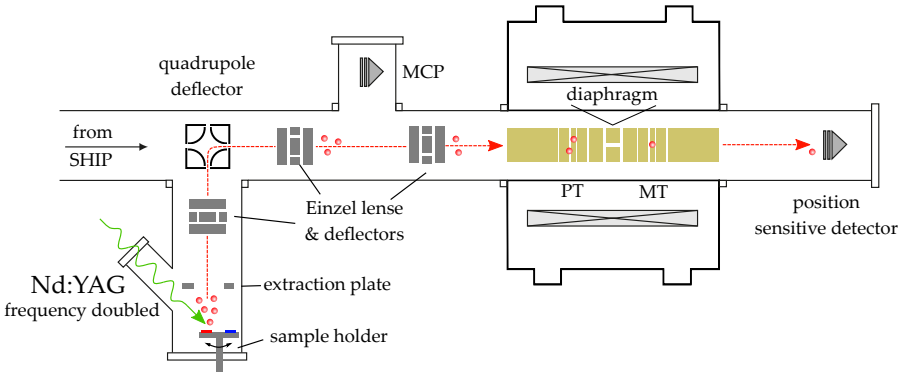

Figure 3.4: Schematic overview of SHIPTRAP. On the left side the connection to SHIP can be seen and the offline laser ablation ion source. Ion optical lenses guide the produced ions to the 7 T superconducting magnet with its two homogenous regions. Therein, two Penning traps are placed. In the first Penning trap, the ions are cooled via buffer gas cooling. To suppress gas flow from the first to the second trap, the latter is separated by a pumping barrier from the first one. With the second trap and a position sensitive MCP detector, the cyclotron measurement is done. For details see text.

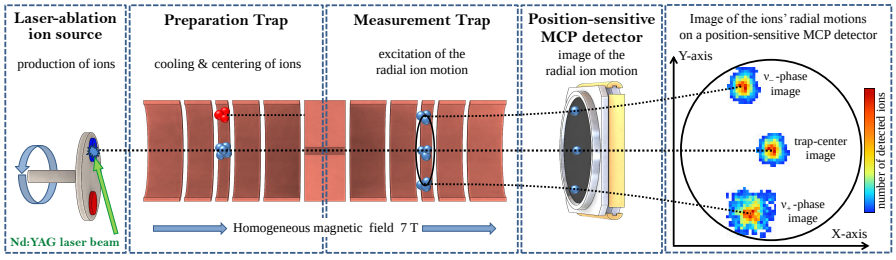

Figure 3.5: Schematic view of the image process of the radial motions in a penning trap used in the PI-ICR technique.

3.3.1 *Phase-Imaging Ion-Cyclotron-Resonance technique*

The Phase-Imaging Ion-Cyclotron-Resonance (PI-ICR) technique is a destructive phase measuring method developed for online mass spectrometers dealing with low production rates and low half lives [37]. This method measures the free cyclotron frequency Eq.(2.14) and is very similar to PnP, see chapter 6.2. The phase of a radial eigenmotion can be read out by projecting the motion after ejecting the ion from the trap onto a position sensitive detector sitting in a low magnetic field region. The travel of the ion through the magnetic gradient magnifies the motions radii, see fig. 3.5. While the trap center will be measured by projecting cold ions to the detector, the radial motion has to be excited to measure the respective phases and frequencies. The thermal distribution and scattering at rest gas atoms reduces the position resolution of single phase spots. The phase of the reduced cyclotron motion can't be directly projected due to its fast motion compared to the axial frequency. A direct projection would lead to a phase spot smeared out to a ring-like shape on the projecting plane. Because of this, the cyclotron phase information is transferred via a sideband coupling ($\nu_+ + \nu_-$) to the magnetron motion which is then projected. The PI-ICR method allows measuring directly the free cyclotron frequency from measuring the phase difference between to pulse patterns, see fig. 3.6 for pattern 1 and fig. 3.7

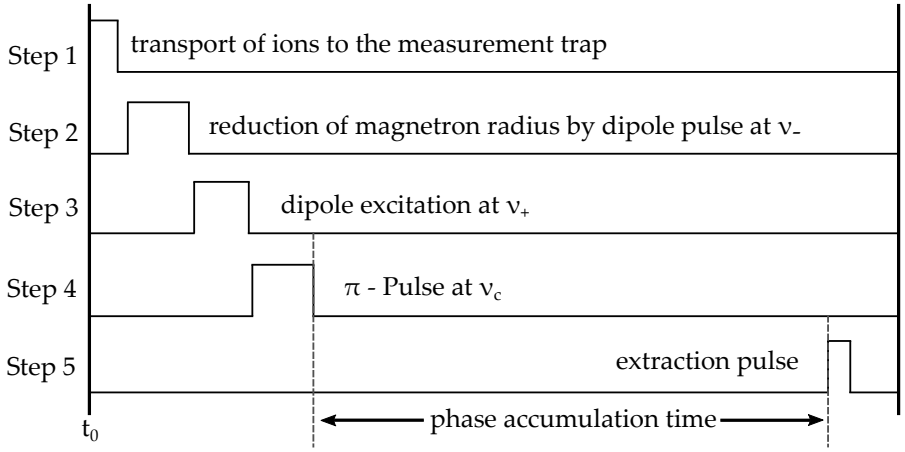

Figure 3.6: Timing diagram of pattern 1. Shown are the applied pulses in the two measurements which are needed to determine ν_c with the PI-ICR technique. For details see text. Picture taken from [37].

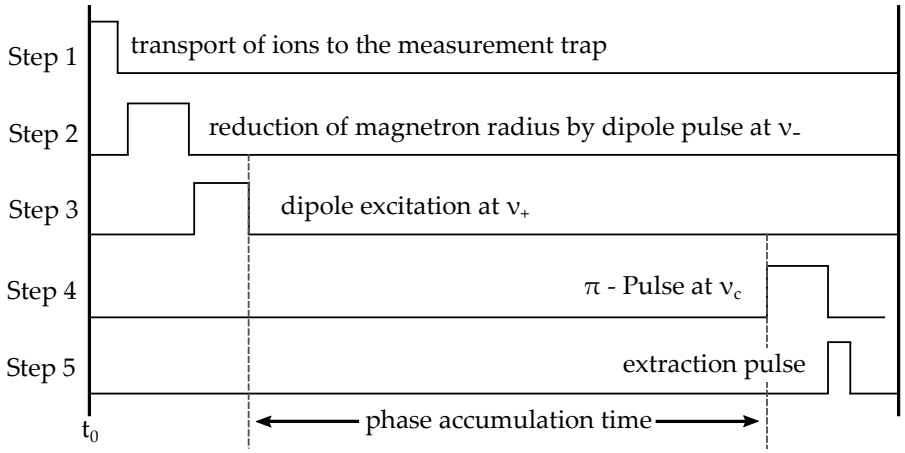

Figure 3.7: Timing diagram of pattern 2. Shown are the applied pulses in the two measurements which are needed to determine ν_c with the PI-ICR technique. For details see text. Picture taken from [37].

for pattern 2. Both pulse patterns are similar except the timing of the phase evaluation time in the pulse sequence. The first measurement (pattern 1) has the phase accumulation time t_1 after a π-pulse converts the phase information into the magnetron mode, the second measurement (pattern 2) has the phase accumulation time t_2 before the π-pulse. If both accumulation times are equal $t = t_1 = t_2$, the free cyclotron frequency can be calculated with

$$\Delta\Phi_c = 2\pi\nu_c t - 2\pi(n_+ + n_-), \tag{3.2}$$

where $\Delta\Phi_c$ is the measured phase difference and $n_\pm$ are integers of the full revolutions (2π), of the reduced cyclotron and respectively magnetron frequency in the phase accumulation time t. The drift and disturbances of the magnetic field determines the maximum of the phase accumulation time, since the any drifts and disturbances should not lead to a missing revolution. The phase spots measured with pattern 2 are larger due the longer storage time in the excited cyclotron motion which increase the probability of rest gas interactions.

3.4 EXPERIMENTAL RESULTS AND DATA EVALUATION

This section will discuss the analysis procedure of the measured data.

3.4.1 *Interpolation of the magnetic field*

One free cyclotron frequency measurement of one ion specie takes about 5 min with the PI-ICR technique. Thus, the average magnetic field within this time intervall will be measured and the ratio R between two followin measurements of e.g. the mother and daughter nuclei can be written as

$$\overline{R} = \frac{\nu_{c,m}}{\nu_{c,d}} = \frac{q_m m_d}{q_d m_m} \frac{\bar{B}(t_m)}{\bar{B}(t_d)} \tag{3.3}$$

where the indices m, d denote the mother and the daughter nuclei and the $\bar{B}(t)$ is the average magnetic field strength over the measurement time, of the respective nuclei. Since t_m and t_d are separated in time, a temporal drift in the magnetic field is leads to a shift and to an uncertainty in the ratio of

$$\delta\overline{R} = \frac{m_d}{m_m} \cdot \frac{\bar{B}(t_m) - \bar{B}(t_d)}{\bar{B}(t_d)}. \tag{3.4}$$

Typical superconducting magnets have a stability of about $\frac{\delta B}{B} \cdot \frac{1}{\delta t} = 10^{-11}/h - 10^{-10}/h$. To account for the B-field temporal instability of the magnetic field the field strength can be interpolated in sequential measurement schemes with a polynomial fitting, as will be discussed now.

POLYNOMIAL INTERPOLATION METHOD IN A SEQUENTIAL MEASUREMENT SCHEME Assuming slow magnetic field changes compared to the time of one ratio measurement a polynomial of the order n and constant coefficients a_i can be used to approximate the field during the measurement:

$$B(t) = \Sigma_{i=0}^{n} a_i t^i. \tag{3.5}$$

The offset in the free cyclotron frequency measurement caused by the drift of the magnetic field can be only determined with a second ν_c measurement of the same nuclei. Thus most information is collected by an alternating measurement of the two nuclei of which the free cyclotron frequencies can be written as

$$\nu_m = \frac{q}{2\pi m_m} \Sigma_{i=0}^{n} a_i t^i = \Sigma_{i=0}^{n} A_i t^i, \tag{3.6}$$

$$\nu_d = \frac{q}{2\pi m_d} \Sigma_{i=0}^{n} a_i t^i = R_m \cdot \Sigma_{i=0}^{n} A_i t^i, \tag{3.7}$$

where $A_i = (q a_i)/(2\pi m_m)$ and $R_m = m_m/m_d$. Both parameters can be obtained by fitting both functions to the experimental frequency points. The fitting procedure will minimize the following χ^2_{red}:

$$\chi^2_{red} = \frac{1}{\mathcal{F}} \left[\sum_{k=1}^{N_1} \frac{(\bar{\nu}_m(t_k) - \nu_m(t_k))^2}{\delta\nu_m^2} + \sum_{s=1}^{N_2} \frac{(\bar{\nu}_d(t_s) - \nu_d(t_s))^2}{\delta\nu_d^2} \right], \tag{3.8}$$

where $\bar{\nu}_{m,d}(t_{k,s})$ are the measured cyclotron frequencies for the mother and daughter nucleus with the uncertainty $\delta\nu^2_{m,d}$ at time t_k respectively at time

t_s. N_1, N_2 are the number of measurements. The normalization factor $\mathcal{F}$ is the degree of freedom and calculated as

$$\mathcal{F} = N_1 + N_2 - p - 1, \tag{3.9}$$

with the number of fit parameters p, which is in this case the degree of the polynomial n with offset and the ratio R_m: $p = n + 2$. The uncertainty the ratio δR_0 is obtained from the fit $R_m = R_0$. Finally, the uncertainty is $\sqrt{\chi^2_{red}} \cdot \delta R_0$. Ideally χ^2_{red} is 1, a value $\chi^2_{red} < 1$ indicates that the polynomial fit over fitting the data and over estimates the uncertainties. A larger value $\chi^2_{red} > 1$ indicates that either the approximation of the B-field variation with a polynomial with constant coefficients is not quite correct or uncertainties of a single frequency measurement is underestimated.

3.4.2 *Cyclotron frequency ratio measurements and statistical uncertainty*

The entire analyzed data set consists of 34 measurement intervals each about 5-hours long. An typical data set of one of these intervals with a polynomial fit is shown in fig. 3.8. With the polynomial method, the frequency R_0^{inter} and its uncertainty δR_0 was obtained from each measurement. The order of the polynomial was determined by the F-test [38, 39]. The relative change of χ^2_{red} for nearby orders of the fit polynomial is taken as a value of measure to find the best value for the polynomial. Finally, the polynomial order was fixed to five. The frequency ratios of each measurement are shown in fig. 3.9.

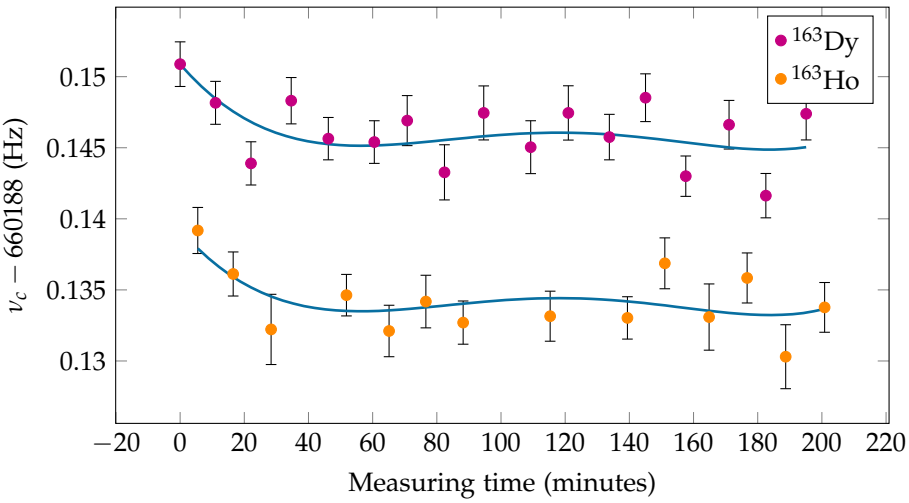

Figure 3.8: Excerpt data of the Ho/Dy frequency ratio measurement with polynomial interpolation of the magnetic field. For details see text.

To determine the final value of R from the 34 single measured ratios the weighted mean R_0, the inner δR_0^{in} uncertainty and the outer uncertainty δR_0^{out} are calculated as follows

$$R_0 = \frac{\Sigma_{i=0}^{n}(\delta R_0^i)^{-2} \cdot R_0^i}{\Sigma_{i=0}^{n}(\delta R_0^i)^{-2}}, \tag{3.10}$$

$$\delta R_0^{in} = \left(\Sigma_{i=0}^{n}(\delta R_0^i)^{-2}\right)^{-\frac{1}{2}}, \tag{3.11}$$

$$\delta R_0^{out} = \sqrt{\frac{\Sigma_{i=0}^{n}(\delta R_0^i)^{-2} \cdot (R_0^{mean} - R_0^i)^2}{(N-1)\Sigma_{i=0}^{n}(\delta R_0^i)^{-2}}}. \tag{3.12}$$

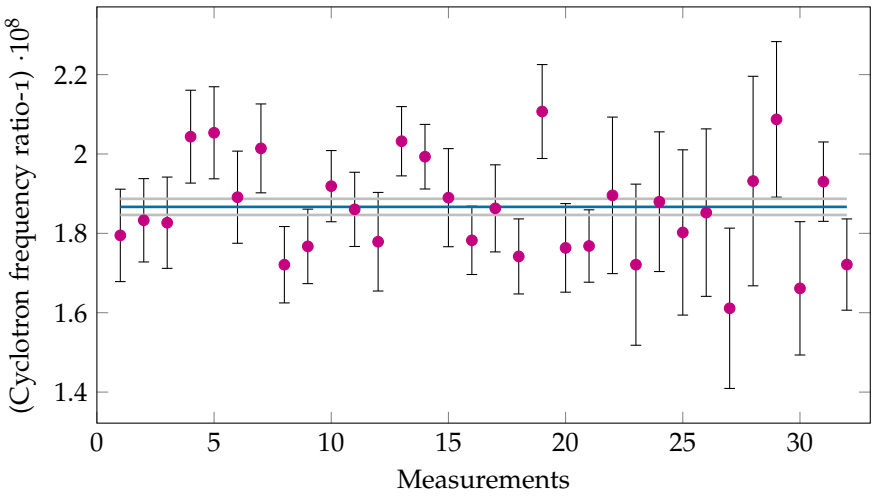

Figure 3.9: Shown are all single cyclotron-frequency ratio measurements of ^{163}Ho to ^{163}Dy. The mean value is indicated with the blue line, the error band is given by the grey lines. For details see text.

An approximately equal value of δR_0^{in} and δR_0^{out} indicates a good error estimation. The error of this analysis results in the statistical uncertainty of the measurement of $20\,eV/c^2$ indicated in fig. 3.9 as error band. While the following section will estimate the systematic uncertainty.

3.4.3 *Estimation of the systematic uncertainty*

To determine the systematic uncertainty the following effects are investigated:

CHOICE OF THE ANALYZED TOF SPECTRA AND POSITION DATA The PI-ICR method produces time-of-flight data and position data. On both sets of data window functions are applied to reduce noise and thus improve the signal-to-noise ratio. Within this predefined window, both data types can be described with a Gaussian distribution.

Since the mean and the width of the Gaussian ToF distribution is different for every measurement, however the chosen window is the same for all measurements, there are several choices for a suitable window. The typical measured value for the FWHM of the ToF distribution is 500 ns and the window was chosen to be 3 FWHM of the Gaussian distribution. This ambiguous choice of the ToF window introduced a systematic error, which was estimated by analyzing the data and calculating the ratio R_0 and ΔR_0

for two different windows. The two different windows are with a maximal and minimal chosen FWHM. The mean position $\bar{t}$ and the mean FWHM $\bar{\Delta}t$ was used to calculate a minimal $\bar{\Delta}t - \delta\bar{\Delta}t$ and maximal $\bar{\Delta}t + \delta\bar{\Delta}t + \delta\bar{t}$ FWHM from which the window is calculated. Applying these two different windows results in a ΔR_0 less than 10^{-10} which can be neglected compared to the statistical uncertainty.

A similar choice needs to be taken in the analysis of the position data. Since the positions of the phase diagrams change with time, the centers of the position data are calculated for each determination of the cyclotron frequency of one species. The phase diagrams have a large distribution width due to ion scattering on rest gas and thus the choice of the window leads to a non negligible relative systematic error of $9 \cdot 10^{-11}$.

FLUCTUATION OF THE PROJECTION OF THE TRAP CENTER The projection of the trap center on the MCP detector changes with time due to e.g. voltage drifts in the extraction electrodes and temperature variations and thus alignment changes. The trap center is not measured for every cyclotron frequency determination rather once in a certain time interval, usually once every day. This lack of knowledge of the exact center during a measurement leads to a systematic error. This error is estimated by two measurements: One at the beginning of the measurement periode and the other one on the end. The difference in the trap center projection position does not exceed 0.04 mm. Half of this drift was taken as an uncertainty of the position and thus already taken into account in the statistical uncertainty.

DISTORTION OF THE PROJECTION ONTO DETECTOR The projection of the ion motion in the Penning trap to the position sensitive detector is typically not a perfect circle. For example a misalignment of the detector plane to the radial plane or the not ideally cylindrical symmetry of the magnetic field leads to an elliptic distortion. The resulting error in the measurement of this distortion can be nullified by minimizing the angle between the magnetron and cyclotron phase spot to zero. In a typical measurement, this angle is in the order of a few degrees. The resulting error is estimated by measuring an upper limit of the ellipticity of the projection and correcting the measured angles with it. The upper limit of the ellipticity was smaller than 1.04 and the differences of the non-corrected and corrected calculated ratios were much smaller than 10^{-10} and thus negligible.

ANHARMONICITY OF THE TRAP POTENTIAL Anharmonicities in the electrical field of the trap potential leads to an radii dependence of the eigenfrequencies of the stored ion. In the case of PI-ICR, this effect can be canceled if the radii of the excited magnetron and excited cyclotron motion are equal. Unfortunately, due to the higher probability of ion scattering in the cyclotron motion, it has a smaller radius than the magnetron motion which leads to a systematic error. To calculate this error only the leading anharmonic c_4 and c_6 are of interest. The relative cyclotron frequency shift $\Delta\nu_c/\nu_c$ caused by the small radii difference is typically less than 10^{-9}. If the radii of the motions of the two nuclei equal $\rho_{m,\nu_+} = \rho_{d,\nu_+}$ and $\rho_{m,\nu_-} = \rho_{d,\nu_-}$ respectively the shift in the ratio can be calculated by

$$\frac{\Delta R_0}{R_0} \approx \frac{\Delta m}{m} \cdot \frac{\Delta \nu_c}{\nu_c}, \tag{3.13}$$

where $\Delta m = m_d - m_m$ and $m = (m_d - m_m)/2$. Thus, the impact of the shift in ν_c is suppressed by $\frac{\Delta m}{m}$ which leads to a shift in the ratio of less than 10^{-10}

Systematic error	relative uncertainty
Choice of the analyzed ToF spectrum	$< 10^{-10}$
Choice of the position data window	$9 \cdot 10^{-11}$
Distortion of the projection onto the detector	$< 10^{-10}$
Anharmonicity of the trap potential	$5 \cdot 10^{-11}$
Inhomogeneity of the magnetic field	$< 10^{-10}$

Table 3.3: Sources of systematic errors and their impact on the result. A detailed discussion is given in the text.

and thus can be neglected. The measured radii of $^{163}Dy^{+}$ and $^{163}Ho^{+}$ are not equal. The cyclotron radius differ of about 0.1 mm to the magnetron radius. This leads to a systematic uncertainty $5 \cdot 10^{-11}$ which can be neglected, too. Similar the relative systematic uncertainty caused by inhomogeneity of the magnetic field can be estimated to a negligible value well below 10^{-10}.

SUMMARY OF SYSTEMATIC ERRORS In tab. 3.3 the systematic erros are summarized. The leading error is caused by the ambiguity in the choice in position data window which determine the systematic error to $9 \cdot 10^{-10}$. The final ratio is thus

$$R = 1.00000001867(20_{\text{stat}})(10_{\text{sys}})$$

and hence with the value of the mass excess of ^{163}Dy of -66379.9(1.9) keV [40] the Q_{EC}-value can be calculated to

$$Q_{\text{EC}}(^{163}\text{Ho} \rightarrow ^{163}\text{ Dy}) = 2.833(30_{\text{stat}})(15_{\text{sys}})\,\text{keV}$$

3.5 IMPACT OF THE RESULT

This first direct measurement of the Q_{EC}-value of the EC in ^{163}Ho shows a large discrepancy of 7σ compared to the value in the Atomic-Mass Evaluation 2012 [34]. As shown in fig. 3.10 especially the discrepancy between the microcalorimetry measurements [41, 42] and the literature value of AME 2012 was a concern for the ECHo experiment. The large offset could have been interpreted as missing knowledge about some systematic effects in the microcalorimeter measurement, making it unlikely without further investigations to obtain the electron neutrino mass with the targeted upper mass limit of $< 10\,\text{eV}/c^2$ (95% C.L.) within ECHo-1k. Based on the above presented results, not only the discrepancy is resolved but thanks to the use of the quite new PI-ICR method, the obtained uncertainty in the Q-value of 32 eV is good enough to act as an independent Q-value determination in ECHo-1k. With the newly determined Q_{EC}-value the uncertainty in the expected sensitivity of the first phase of ECHo can be reduced, as shown in fig. 3.11. Thus in the first phase of ECHo with a foreseen number of recorded events of $N = 10^{10}$, ECHo will be able to reach a statistical uncertainty of less than $10\,\text{eV}/c^2$ on the electron-neutrino mass. This will improve the current value of $m(\nu_e) < 225\,\text{eV}/c^2$(95% C.L.) [15] by more than an order of magnitude. For further improvements of the upper mass limit of the electron neutrino mass to sub-eV level, the Q_{EC}-value of the EC in ^{163}Ho needs to be improved, too. This measurement is planned to be done with the high-precision mass spectrometer PENTATRAP as it will be introduced in the next chapter.

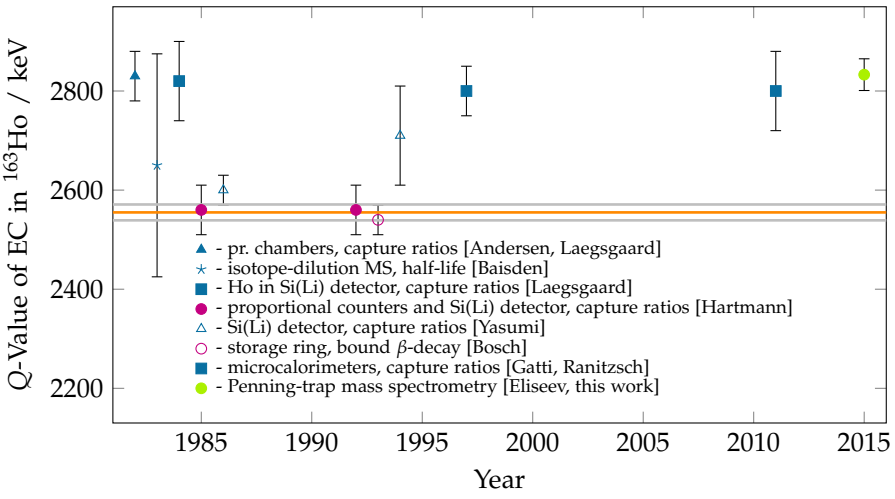

Figure 3.10: Shown are measured Q_{EC} of the EC in ^{163}Ho against the year publication year (Andersen [43], Baisden [44], Laegsgaard [45], Hartmann [46, 47], Yasumi [48, 49], Bosch [50], Gatti [41], Ranitzsch [42], Eliseev [29]). Different experimental methods are marked with different shapes. The literature value is marked as orange line. Purple colored points are used to determine the literature value.

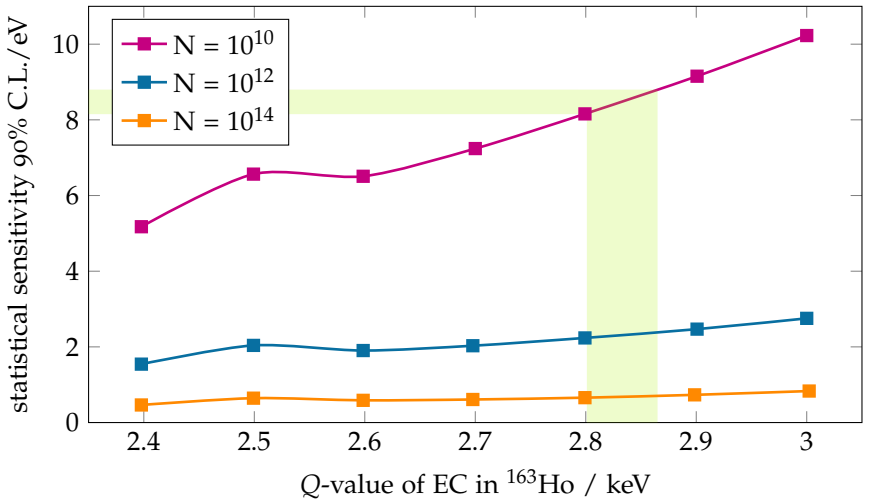

Figure 3.11: Achievable statistical uncertainty of the ECHo experiment in the determination of the electron-neutrino mass as a function of the Q_{EC} of the EC in ^{163}Ho. The different curves show this dependence for different acquired electron-capture events. The green colored region maps the newly achieved uncertainty [29] of the Q_{EC} of ^{163}Ho to the statistical sensitivity for $N = 10^{10}$ acquired events.

4 THE PENTATRAP MASS SPECTROMETER

The objective of PENTATRAP breaks down to build an apparatus which can measure mid to heavy long-lived nuclei with a relative mass uncertainty of better than 10^{-11}. In this chapter the design and construction of the PENTATRAP setup is discussed starting with the fundamental ideas of PENTATRAP (4.1), which are supported by the experience of other Penning-trap mass spectrometers. This discussion is followed by a description of the beamline (4.2), an overview of the cryogenic setup (4.3), an overview of the cryogenic electronics (4.4) and a brief description of the FFT-Analyser and the control system (4.6).

4.1 INTRODUCING THE MOTIVATIONS FOR PENTATRAP

4.1.1 *Limitations of existing mass spectrometers*

In order to develop a new mass spectrometer it is useful to learn from existing projects and to adapt and to overcome their limitations. A discussion of the main systematic uncertainties of existing Penning-trap mass spectrometers can be found in [51] and they are mainly caused by:

- magnetic field drifts and
- voltage instabilities.

Not only sources of systematic errors can be reduced also the maintaining and controlling effort of the mass spectrometer. The improvement of the later ones will reduce the time between the measurement projects reduce handling errors and thus increase the output of the experiment.

4.1.2 *The idea of a five trap system - how to reduce the impact of magnetic field drifts?*

As the name PENTATRAP indicates the main idea is to use a stack of five nearby Penning traps in the same magnet system. A five trap system gives access to a number of different schemes [52] which among other things can reduce the influence of the magnetic field drifts:

SINGLE MEASUREMENT TRAP The simplest scheme is to use only one trap to perform the measurements. The other traps are used as storage traps. To apply a fast switching scheme, one of the three traps in the middle has to be used. Two Ions will be loaded: One in the measurement trap the other one in one of the neighboring traps. To switch the ion species in the measurement trap the ions are shifted both one trap in the direction to the empty neighboring trap.

TWO MEASUREMENT TRAPS This is the favorite advanced measurement scheme which will be at PENTATRAP firstly tested. With two measurement traps ($\text{trap}_{1,2}$) simultaneous measurements of the free cyclotron frequencies $\nu_{c_{1,2}}$ of both species can be performed. While exchanging the ion species

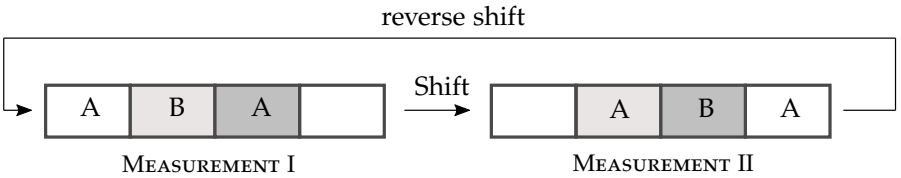

Figure 4.1: Schematic visualization of the favorite measurement scheme for PENTATRAP. The single traps are represented as rectangular boxes. The measurement traps are marked with light-grey and dark-grey. The two ion species are given the letters A respectively B. After the first step of the relative measurement (Measurement I) the ion are shifted on trap further for the second step (Measurement II). After the second step, the ions are reverse shifted to restart with the first step until the statistical error is at least as low as the systematic error.

(A, B) after each measurement cycle, it is possible to eliminate magnetic field drifts to a large extent:

$$R_n = \frac{\nu_{c,A,trap_1,n}}{\nu_{c,B,trap_2,n}} = \frac{B_{trap_1,n} q_A m_B}{B_{trap_2,n} q_B m_A} = \rho_n \frac{q_A m_B}{q_B m_A} \tag{4.1}$$

$$R_{n+1} = \frac{\nu_{c,B,trap_1,n+1}}{\nu_{c,A,trap_2,n+1}} = \frac{B_{trap_1,n+1} q_B m_A}{B_{trap_2,n+1} q_A m_B} = \rho_{n+1} \frac{q_A m_B}{q_B m_A}, \tag{4.2}$$

where R_n is the cyclotron frequency ratio measured at time n and $\rho_n = \frac{B_{trap_1,n}}{B_{trap_2,n}}$. Combining these two consecutive measured ratios yields the Ratio R,

$$R = \sqrt{\frac{R_n}{R_{n+1}}} = \sqrt{\frac{\rho_n}{\rho_{n+1}}} \frac{q_A m_B}{q_B m_A}. \tag{4.3}$$

In case the ratio of the magnetic field strengths in the two measurement traps is constant,

$$\rho_n = \rho_{n+1}, \tag{4.4}$$

the magnetic field dependence in the cyclotron frequency ratios determination drops out,

$$R = \frac{q_A m_B}{q_B m_A}. \tag{4.5}$$

In this scheme three ions are loaded: Two of the same specie, one spices one of the reference specie. Similar to the single trap measurement the exchange will happen by shifting all ions one trap further in the same direction. This measurement scheme needs thus four traps. A schematic flow diagram of the measurement scheme is shown in fig. 4.1. Only changes in the magnetic field gradient will add to the systematic error: To which degree the magnetic field ratio can be assumed to be constant is still under investigation. The hope is that the change in the ratio is strongly suppressed compared to global magnetic field drifts.

THE FIFTH TRAP The fifth trap can be used for a third ion specie e.g. ^{12}C to be used as a magnetic field sensor. Another possibility is to use it as a voltage to frequency converter which can be used to stabilize the voltage source of the traps. Since the advanced measurement scheme only uses four

traps the fifth trap gives you freedom in choosing the two measurement traps. In this way the "fifth" trap will be either the most upper or lower one in the trap tower. Introducing this redundancy can higher the duty time of the system in the event of the failure of the outer measurement traps.

4.1.3 *Using highly-charged ions*

This section summarizes the description given in [53]. Voltage instabilities affect the measurements of all single eigenfrequencies. This voltage instabilities would drop out if all eigenfrequencies could be measured simultaneously. Unfortunately neither with the double dip method nor with the phase method can the eigenfrequencies measured simultaneously. However this voltage instabilities are suppressed in the determination of ν_c with a more pronounced frequency hierarchy (see eq. [2.12]) and the resulting shift has to be treated for each eigenfrequency measurement independently as follows: Beginning with the shift in the ν_+ measurement,

$$\frac{\Delta\nu_c}{\nu_c} = -\left(\frac{\nu_+}{\nu_c}\right)^2 \frac{\nu_z^2}{\nu_+(\nu_+ - \nu_-)} \frac{\Delta U_0}{2U_0}. \tag{4.6}$$

The shift in the ν_- measurement only differs relative to the previous shift in the frequency ratios,

$$\frac{\Delta\nu_c}{\nu_c} = -\left(\frac{\nu_-}{\nu_c}\right)^2 \frac{\nu_+^2}{\nu_+(\nu_+ - \nu_-)} \frac{\Delta U_0}{2U_0}. \tag{4.7}$$

And finally the shift in the ν_z measurement,

$$\frac{\Delta\nu_c}{\nu_c} = -\left(\frac{\nu_z}{\nu_c}\right)^2 \frac{\Delta U_0}{2U_0}. \tag{4.8}$$

Modern state-of-the-art voltage sources have a relative voltage stability of $\frac{\Delta U_0}{U_0} = 10^{-8}$ over a timescale of $\approx 10\,\text{min}$, which is the time PENTATRAP needs for one single ν_c measurement. In order to reach a relative uncertainty of better than 10^{-11} the suppression of $\Delta U_0/U_0$ needs to be in the order of 10^{-3} or better. Assuming an axial frequency of 500 kHz and ^{163}Ho as the ion of interest, a minimum charge state of 17+ is needed to reach this suppression factor. In the case of and ^{132}Xe a charge state of at least 14+ is required.

4.2 EXTENDED BEAMLINE SETUP - CONNECTING THE ION SOURCES TO PENTATRAP

To reduce the time needed to lift the trap system out of the magnet, a major modification of the beamline was done within this thesis. Among others one of the ions sources(DREBIT) was moved to a permanent position. Additionally the hole in the ceiling was enlarged and the vertical beamline was mounted on rails. This made it possible to lift or lower the cryogenic setup without venting major parts of the beamline. However, these modifications required adding electrostatic optical elements which increase the number of parameters which have to be optimized. The present parts of the beamline setup will be discussed in the following sections.

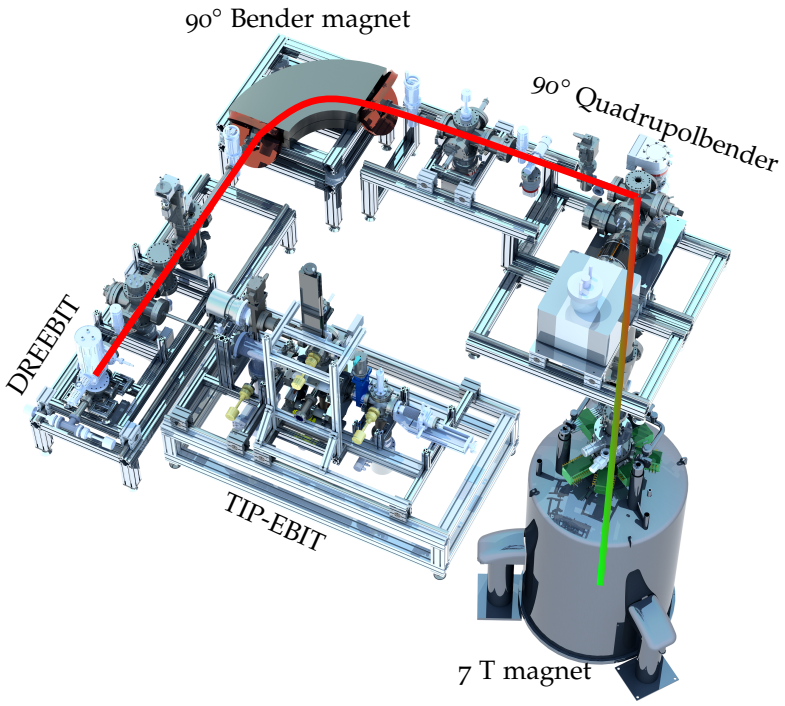

Figure 4.2: Overview of the PENTATRAP setup without the coupling to the HD-EBIT. The red line indicates the ion path from the DREBIT to the magnet center where the traps are installed. The red color indicates the start energy of the ions of about 7 keV down to 10 eV indicated by the green color. For the deaccelerating electrostatic drift tubes are used which are sitting in the vertical section indicated by the color gradient.

4.2.1 *Ion sources*

Originally the beamline contained two ion sources for the production highly charged ions: A tabletop EBIT from the comapny *DREBIT* is used for measurements where no bare nuclei are needed and the larger superconducting HD-EBIT to deliver bare nuclei up to lead. But due to the small amount of material available for some specific cases like ^{36}Cl and ^{163}Ho which are to little to not efficiently be injected in the DREBIT as well as in the HD-EBIT, a new development (TIP-EBIT) was started to overcome this problem [54]. With this new development three highly-charged ion sources will be available in the near future:

- Dresden-EBIT3, see [55],
- TIP-EBIT, based on [54],
- HD-EBIT, see [56].

With the TIP-EBIT it will be possible to bread highly charged ions from small amounts of material ($\approx 10^{14}$ atoms). This new EBIT can be coupled to the existing beamline with an extra 90° electrostatic bender, see fig. 4.2.

4.2.2 *Electrostatic lenses and q/m separator*

Compared to the previous setup described in [53] one electrostatic lens and deflector was removed, see fig. 4.3. In the horizontal section of the beamline, an electrostatic lens and deflector are installed in front and after a the 90°

bender magnet. The 90° bender magnet is used as a charge-to-mass ratio (q/m) separator. With a proper slits system a resolution of 400 was reached [57]. It is used to load the trap with q/m separated ion samples from the DREBIT and the TIP-EBIT. In addition, an ion beam with one well-defined velocity component simplifies the tuning of the electrostatic optical components. The current of the magnet is supplied by a power-supply *TOE 8872* by the company *TOELLNER*. Since the digital control of the supply is not precise enough, the analog current control input is used. This input is connected to a RF-Generator *33500B* of the company *Keysight Technologies*. This allows a current control in 0.1 mA steps. An installed hall sensor *SS495A1* of the company *Honeywell* measures the magnetic field. The output of the hall sensor is read by a multimeter *34465A* of the company *Keysight Technologies*. The *34465A* and *33500B* are controlled and read out by the control system.

4.2.3 *Diagnostics units*

There are several beam diagnostic possibilities available in the beamline: An inline diagnostic unit, a fixed MCP detector unit and two cryogenic Faraday cups:

THE INLINE DIAGNOSTIC: The inline diagnostic unit has two options: A MCP detector with phosphor screen and a Faraday cup. Both are mounted on the same linear stage which enables to place one or none of the devices inside the beam path. The phosphor screen is read out via a camera of type *Prosilica GC 655* of the company *Allied Vision*. A detailed description of the diagnostic unit is found in [58].

THE FIXED MCP DIAGNOSTIC: The fixed MCP detector diagnostic unit is an MCP with phosphor screen which can be placed at the end of the beamline. The phosphor screen is read out via a camera of type *Prosilica GC 655* of the company *Allied Vision*.

CRYOGENIC FARADAY CUPS: In front of the cryogenic pumping barrier a Faraday cup is installed with a hole of the size of the pumping barrier tube. At the end of the trap tower another Faraday cup is installed which is mainly used for the optimization of the beamline settings and to find the correct timing of the cryogenic pulsed drift tube, see next paragraph.

4.2.4 *Drift tubes for deaccelerating ions*

The energy of the ions which can be captured depends on the maximum voltage of the voltage source which supplies the trap. In practice, the maximum ion energy is defined by the frequency of the axial resonator since the ion frequency needs to match the resonator frequency to be detected and especially cooled. At PENTATRAP the ions are decelerated with two drift tubes. The first and larger drift tube decelerates the ions from their start kinetic energy of about $\approx 7\,\mathrm{keV/q}$ down to $150\,\mathrm{eV/q}$. This drift tube sits outside of the magnetic field, while the cryogenic drift tube sitting directly in front of the traps in the 7 T magnetic field. In the final step the cryogenic drift tube decelerates the ions down to few a eV. Due to the cabling in the cryogenic setup, the maximal apply able voltage for the cryogenic drift tube is 200 V.

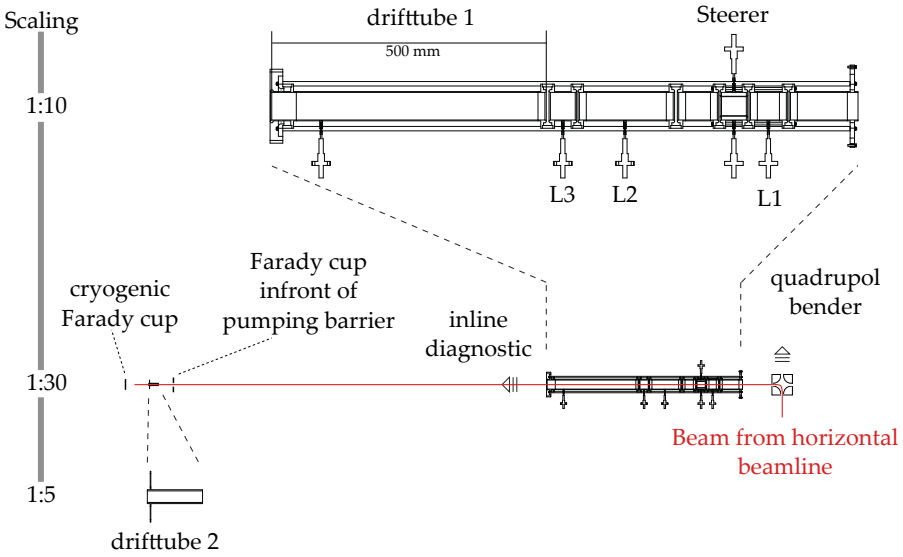

Figure 4.3: Sketch of the electrostatic optical elements in the vertical beamline. The beam enters the vertical beamline after being bent by the quadrupole bender. An electrostatic einzel lens with steering unit sits in front of two einzel lenses and the 50 cm long drift tube. Below the first drift tube a diagnostic unit can be moved into the beamline. After a few meters the beam passes a Faraday cup with a hole in it which is mounted in front of the pumping barrier. After the Faraday cup the beam enters the second drift tube and can be detected by the last Faraday cup which is located after the trap tower. Figure taken and modified from [53]

4.3 CRYOGENIC SETUP

Within this thesis, a complete redesign of the cryogenic setup was performed. The former setup suffered from vacuum leaks which occurred during the cool down process to 4.2 K. The main idea in the new setup is to reduce the complexity and to increase the maintainability compared to the predecessor setup. To do so a cryogenic trap adjustment system is no longer foreseen, the feedthroughs are now exchangeable in groups of six. The setup is separated into two vacuum areas, the prevacuum and the trap vacuum. Still of concern is the permeability of the materials which should disturb the homogeneity of the magnet as less as possible. In the next sections the single parts of the new setup are described:

4.3.1 *Trap tower*

The trap tower is the central part of the cryogenic setup. Everything else in the cryogenic setup is build to supply the trap tower with DC and RF voltages or to provide a vacuum better than 10^{-14} mbar. There are five single Penning traps stacked in the tower. Each one consists of five cylindrical electrodes, some of them are splitted to be able to apply radial dipole and quadrupole excitations.

For the first commissioning phase the previously designed trap tower was used, for details see [58]. Since the use of the previous tower is only temporary, the rest of the setup is designed for the new trap tower. The new trap setup will overcome some limitation in the mechanical realization, see [59] and [60] for details:

- The support structure can be set onto a variable potential, which will give more flexibility for the loading procedure, compared to [58].
- The copper electrodes will shrink onto the sapphire rings, which should avoid a possible deforming while cooling down.
- More splitted electrodes are introduced to have more flexibility concerning RF excitations.

The new design is shown in figure 4.4. The first as well as the second designs are based on the calculation done in [61].

4.3.2 *Dual vacuum system: Pre- and trap-vacuum*

Two strategies were applied to reduce the chance and the impact of possible leaks. The first one was to reduce the number sealings which are in contact with liquid helium to a minimum level without affecting the maintainability. The second one was to shield the trap vacuum with a prevacuum enclosure: Any leaks in the trap-vacuum system are reduced by the prevacuum. Due to this extra vacuum also the thermal coupling was reduced, which resulted in a reduced thermal shock of the trap vacuum system and the attached critical components like the ceramic feedthroughs during the cool down process. In fig. 4.6 the temprature over time during the cooldown is shown.

To avoid the problem of two fixed bearings in the setup it was necessary to decouple the pre-vacuum chamber with bellows. Thus, one side of the thermal coupling of the inner part need to be flexible, too. Even though at room temperature the remaining flexibility without extra flexible elements would still allow an assembly of the parts, the flexible parts avoid stress on the setup during the rapid cooldown to 4.2 K. Especially the inner parts cool down slower than the outer chamber. A great improvement of the maintainability comes with the double vacuum setup: For any change on the electronics which, are mounted in the pre-vacuum, the trap-vacuum doesn't need to be vented.

To reach a vacuum of better than 10^{-14} mbar in a system which is cryogenically pumped it is necessary to reduce the amount of helium and hydrogen in the system already at room temperature. Because at 4.2 K helium is not freezing to the surfaces and hydrogen forms only a monolayer at the surfaces.

4.3.3 *Pumping barrier versus cryogenic valve*

A not closed cryogenic system has to suffer from a continuous stream of particles from the room temperature section. Of major concern are again helium and hydrogen. On the one hand, it is possible to reduce the helium and hydrogen background with well-chosen materials e.g. low hydrogen annealed steel. On the other hand, one can reduce the flow into the trap-vacuum. This is either possible with a cryogenic pumping barrier (see fig. 4.7) or a cryogenic valve (see fig. 4.8). Since a cryogenic valve is a larger engineering effort especially with the available space at the new PENTATRAP setup, in a first version a cryogenic pumping barrier was chosen to have time with the engineering of the cryogenic valve.

CRYOGENIC PUMPING BARRIER: The cryogenic pumping barrier is a 45 mm long and 3 mm in diameter sized gold plated tube. It is sitting close

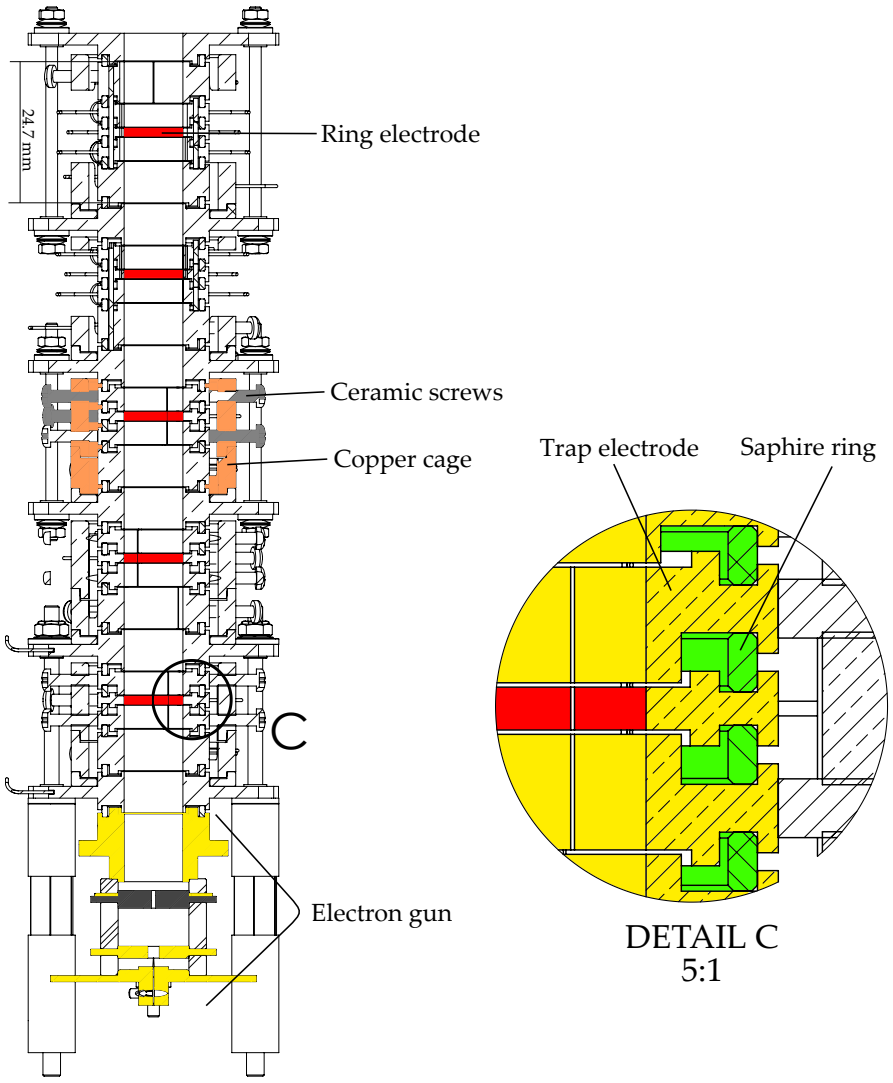

Figure 4.4: Drawing of the vertical cut through the new PENTATRAP trap design with its five traps and an electron gun for in trap ion production. Every ring electrode is marked with red color. One of the copper cages which presses with ceramic screws (grey) the halved electrodes again the sapphire rings are marked in orange. Detail C shows an enlarged view of the electrode geometry which shrinks onto the sapphire rings.

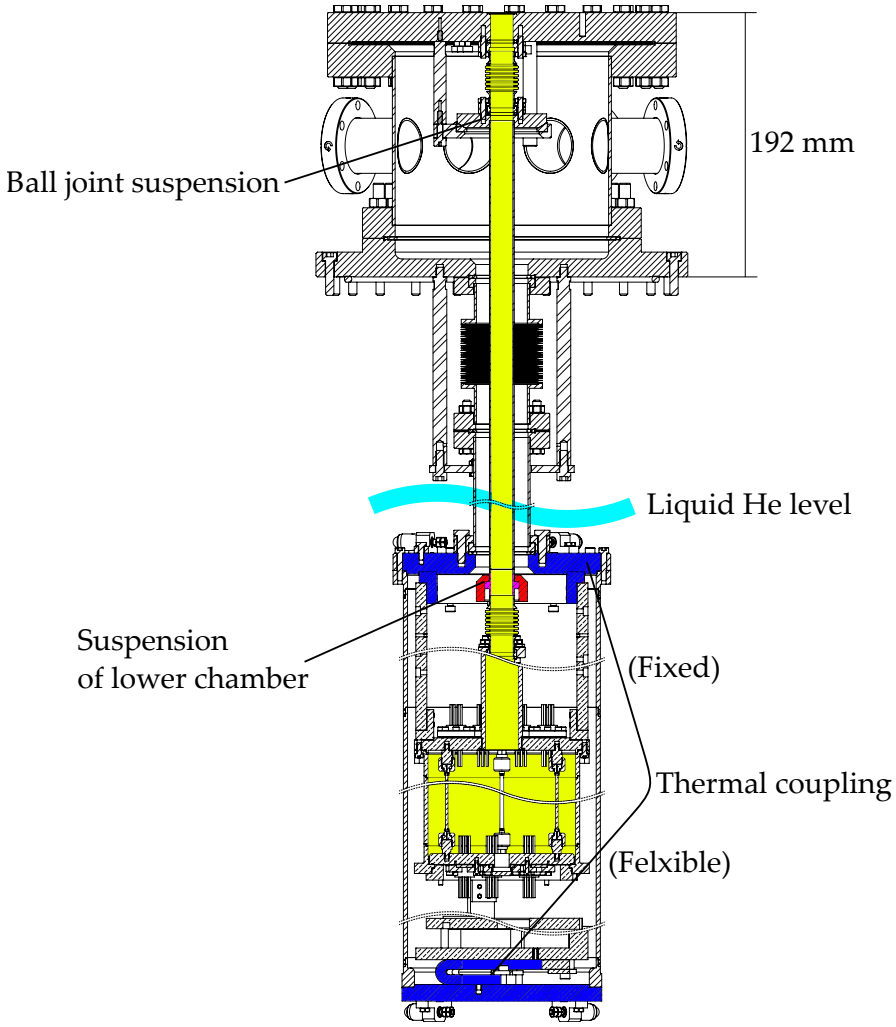

Figure 4.5: Reduce cut drawing of the vacuum setup. For better length-to-width ratio of the picture long repetitive parts are cut away indicated by two-wave lines. The beamline and trap-vacuum are highlighted in yellow. The thermal couplings of the inner parts of the pre-vacuum chamber are marked in blue. The planned level of the liquid helium is indicated by light blue. The lower chamber is decoupled by a ball joint suspension from the upper chamber to allow some movement against each other. This is necessary to avoid stress while the setup is inserted into the magnet. The length of the pre-vacuum chamber emerged in liquid helium is 932 mm.

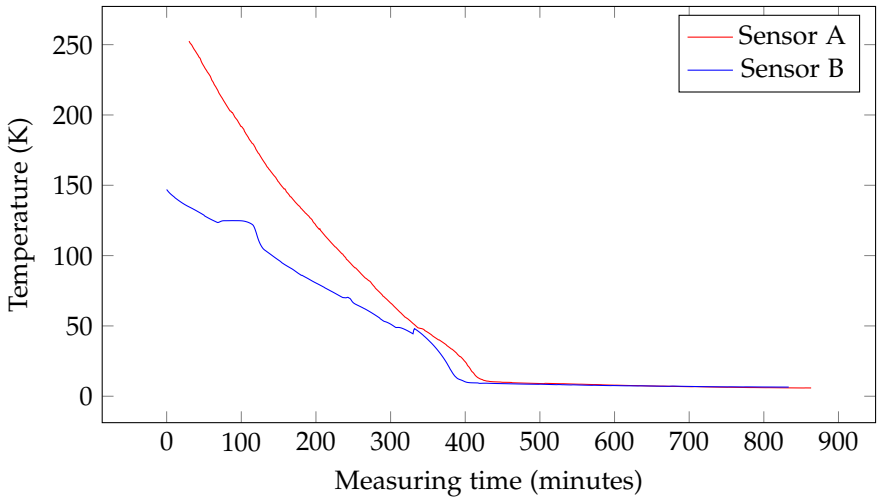

Figure 4.6: Sensor values of the two installed temperature sensors in the cryogenic section of PENTATRAP. Sensor A sits at the top of the pre-vacuum chamber while sensor B is attached to the axial-resonator chamber near the bottom of the pre-vacuum chamber. The measurement started about 30 min after the setup was installed in the magnet. The first step in the curve of sensor B was caused by a readout error while the other steps in the curve were caused by different actions on the valves attached to the magnet. The helium level is lowered during the insertion of the setup due to the higher pressure caused by evaporating helium. The helium level only has contact to the lower end of the setup. This also explains why the sensor B is more sensitive to pressure changes caused by actions on the magnet valves.

to the 7 T magnetic field. With this boundary conditions, the compression of an incoming ion beam is given by the Brillouin radius [62] extended by Herrmann [63]. The radius r of the particle beam depends on the magnetic field B:

$$r \propto \frac{1}{\sqrt{B}}. \tag{4.9}$$

In the worst case, the starting radius is defined at the entrance of the magnet by the inner diameter of the CF 16 tube being at PENTATRAP 16 mm. The starting magnetic field is roughly 10 mT while the pumping barrier is about B=7 T [58]. This results in a compression radius of about 0.6 mm at the pumping barrier. A conservative factor of two is added for possible alignment errors of the pumping barrier in respect to the magnetic field resulting in a rounded value of 3 mm inner diameter. Due to space requirements, a length of 45 mm was chosen. At room temperature, the trap chamber has to be pumped through the pumping barrier, therefore, an extra pumping port below the pumping barrier was installed. This pumping port can be closed by pinching off a soft glowed copper tube. With the connection of a pressure gauge at the pumping port it was verified that it is possible to reach the necessary background pressure of 10^{-6} mbar pumping though the pumping barrier within an acceptable time of few days. Thus the pinch off port was closed with a blind flange to reduce the complexity. A drawing of the pumping barrier is shown in fig. 4.7. To have a possibility to check if ions can reach but can't pass the pumping barrier a Faraday-cup with a centered hole of the size of the pumping barrier is installed above the pumping barrier.

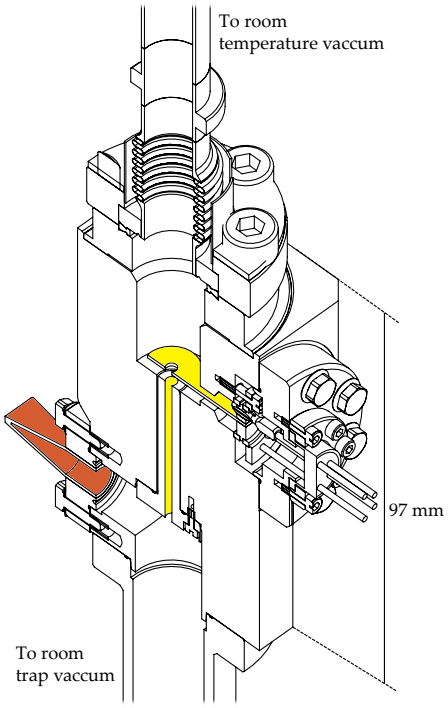

Figure 4.7: Cut view of the cryogenic pumping barrier sitting at ca. 7 T. From above the ion with $\approx$ 100 eV/q are injected. The colored parts are the Faraday cup, die pumping barrier tube in yellow and the pinched off tube in red.

CRYOGENIC VALVE: Due to space requirements the cryogenic valve cannot be actuated with a rigid shaft as installed at ALPHATRAP [60]. With the current design of the valve it is opened by pulling a Bowden cable and is closed by copper beryllium springs. In this way, it should be assured that there is no force acting on the setup by pulling the cable while a measurement is running. To have a high sealing pressure a rotatable sealing ball was placed above the sealing surface. If the valve is opened by lifting the middle platform the ball starts rotating till the channel in the ball is aligned with the axis. The middle platform is decoupled by two bellows. It is pressed down in the closed mode by four copper-beryllium springs which apply a force of effective 200 N each. The valve is opened by pulling a stainless steel wire. The wire is guided through a pulley system for two reasons: First, it reduces the pulling force second, it distributes the pulling force over the platform and reduces the stress for the linear stages guiding the middle platform. The functionality of this valve has still to be shown. A drawing of the valve is shown in fig. 4.8.

4.3.4 *Trap chamber*

The trap chamber sits below the pumping barrier, the electronic section and above the resonators. Connections need to go to both directions, thus the chamber is equipped with feedthroughs on the top and bottom. During installation of the trap, the two feedthrough flanges are held on distance by four 2 mm thick copper roods which are formed to have an extra elasticity. When the trap chamber is closed two indiums sealings are needed to be tightened at once. Of course also the wiring of the trap has to allow for some elasticity while closing the trap chamber.

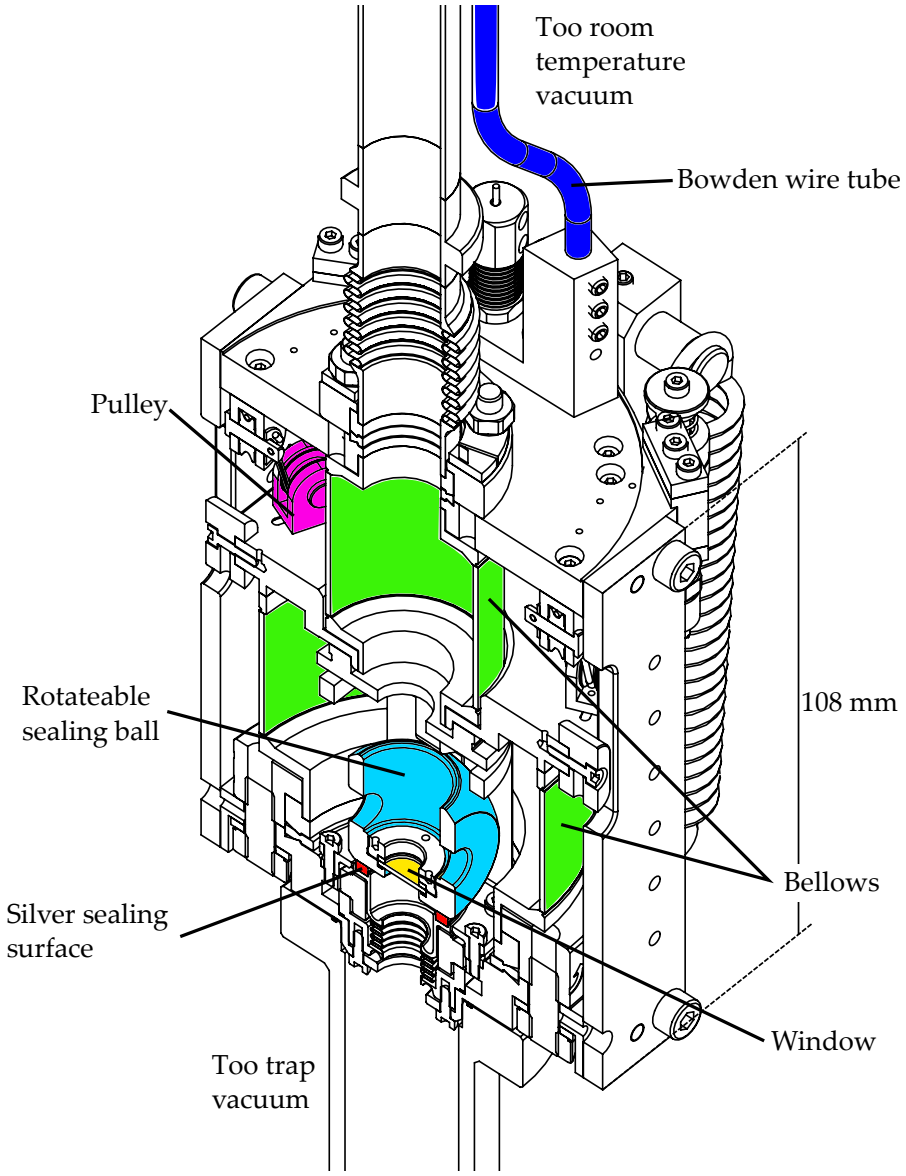

Figure 4.8: Cut view of the 3d model of the cryogenic valve. Important parts are highlighted: The middle platform is decoupled by two bellows (green). This platform is pressed down copper beryllium springs and can be pulled up by pulling on the cable guided by the wire tube (blue). The force which is needed to lift the setup is reduced by a pulley system (purple). When the middle platform is pressed down the sealing ball will rotate into the "'close"' position and is pressed against the silver sealing surface. For future laser accessibility, a window was added.

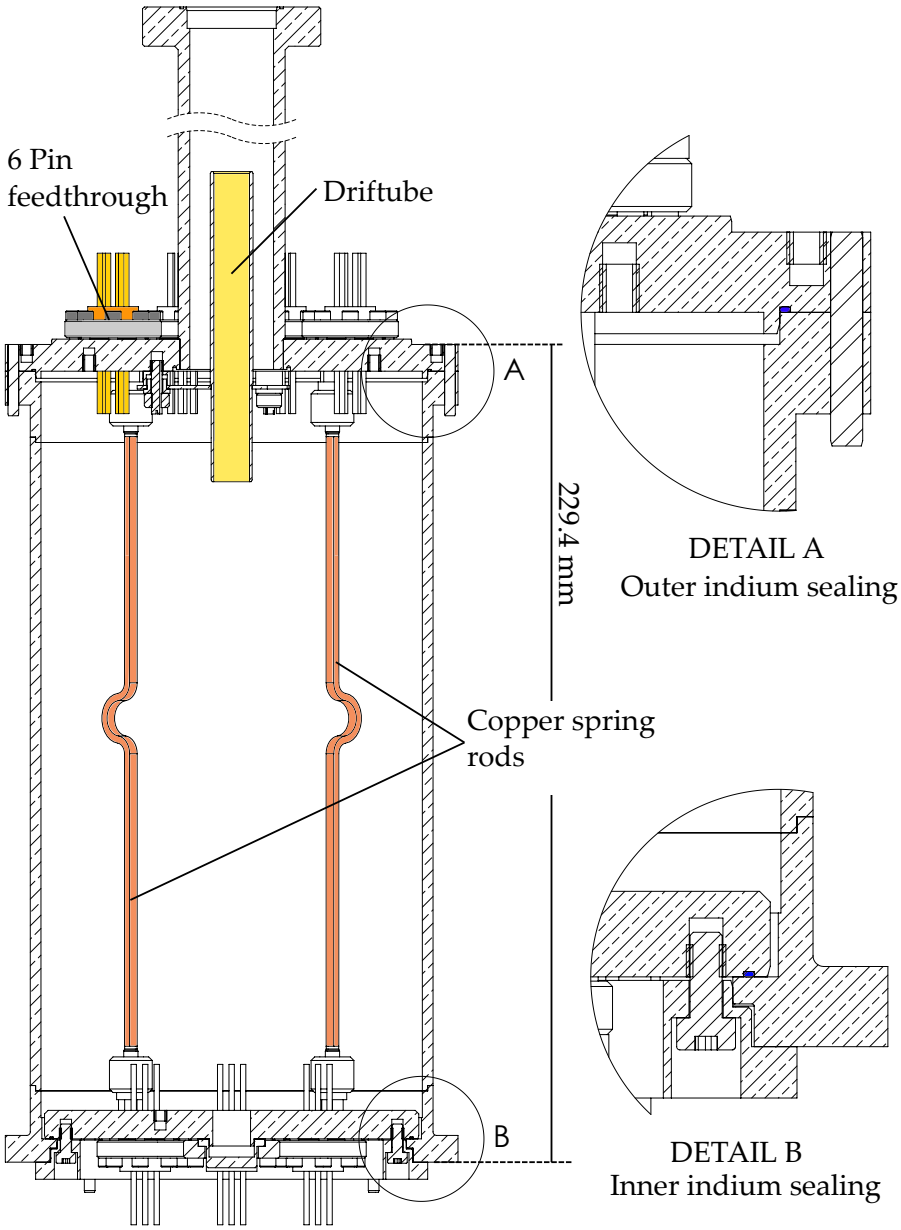

Figure 4.9: Drawing of a cut through the trap chamber. Highlighted are one 6 pin feedthrough, the drift tube, the copper spring rods and the both indium sealings. The copper spring rods are necessary to keep the two flanges on distance while installing the trap. When the chamber is closed the two indium sealings needs to be tightened simultaneous.

4.4 CRYOGENIC ELECTRICAL SETUP

The cryogenic electrical setup has following purposes:

- thermalisation of incoming and outgoing cables from and to the room temperature section,
- low pass filtering of DC voltages for trapping potential and gate voltages,
- switching RF signal lines to ground to reduce incoming noise if the lines are not in use,
- merging RF signals with the DC voltages before connecting to the trap electrode.

Most of the used components are passive components, i.e. resistors and capacitors. The only active component are the RF-switches. The selection of the components are based on previous experience [53], [61]. Resistors where chosen from the *PANASONIC ESU Series*. RF-switches are *SW-232* based on GaAs which are still operational at 4.2 K. Due to lack of experience with the some required capacitors, ones with *CoG* and *NOG* dielectrics were chosen and tested for suitability. For cryogenic coaxial connections the MCX Connectors by *Radiall* are used. Although they have a nickel layer below the gold layer. If the usage of this connectors results in a too large disturbance of the magnetic homogeneity the connectors will be replaced by the commercial available non-magnetic versions. The DC connections are made with simple pin-headers and sockets from different companies. In the following sections the different electronics parts are explained in detail:

4.4.1 *Room temperature electronics*

In the uppermost chamber of the setup which is inserted into the magnet, eight CF40 ports are radially installed, see fig. 4.5. On this ports the electrical feedthroughs are mounted and the six room-temperature electronics boxes are connected to them. One port is equipped with 4-port SMA feedthroughs which are used to read out the level sensor, the cryogenic Faraday Cups and to provide high-voltage to the cryogenic drift tube.

The boxes are separated by their purpose:

1. Trap voltages (low pass filter: 80 $k\Omega$ and 25 nF)
2. Switch control voltages and temperature readout (low pass filter: 80 $k\Omega$ and 25 nF, temp. readout not filtered)
3. Amplifier output (active mixer boards)
4. Amplifier feedback lines (capacitive voltage divider, 10 nF to 10 nF)
5. Amplifier supply and gate voltages (supply lines not filtered, gate voltages: low pass filter: 80 $k\Omega$ and 25 nF)
6. RF-excitation (capacitive voltage divider, 10 nF to 10 nF)

The boxes are either connected to a CF40 D-SUB 25 pin feedthrough (*210-D25-C40* by *Allectra*) or a CF40 Micro-D 51 pin feedthrough (*CF40-MDTL8-51-FM-CE-CBG* by *VACOM*) on the upper chamber. For the latter ones self-made vacuum side connectors have to be mande, see fig. 4.11. Most of the

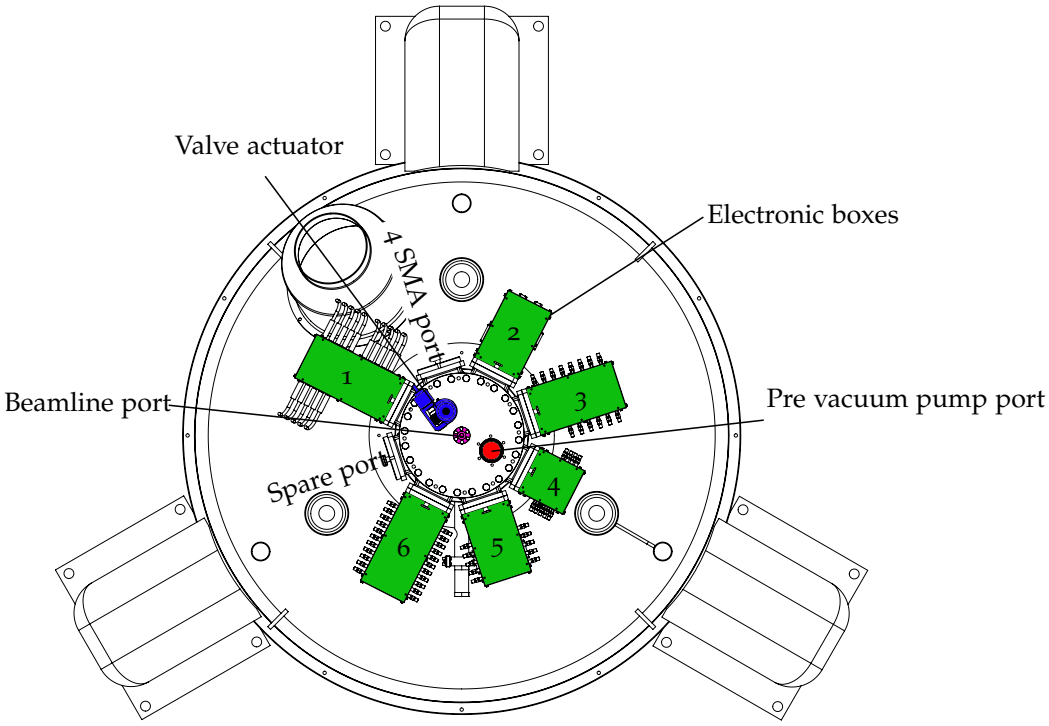

Figure 4.10: A schematic view on the top of the magnet with installed cryogenic setup is shown. Highlighted are the six electronic boxes, the planned valve actuator, the prevacuum pump port and the beamline port. The numbers of the boxes matches the enumeration their description in the text.

boxes contain only passive components for capacitive voltage dividers or low pass filters. Another important feature of the boxes are the mapping of the vaccum-feedthrough connectors to a more user friendly connection system.

4.4.1.1 *Pre-amplifier and Downmixer - Amplifier Output Box*

When the output signal from the cryogenic amplifier arrives at room temperature it will be again amplified and mixed down in the audio range (1 kHz to 20 kHz). This is done with special design electronics boards. For details see [53].

4.4.2 *RF-DC mixer boards*

There is one RF-DC mixer board for each trap. Each trap needs five DC voltages and the new design of the trap foresees seven RF excitations. To reduce noise from the RF-excitation lines which obviously cannot be low-pass filtered, the RF-excitation lines can be grounded with a semiconductor switch before merging with the DC-voltage. Also to reduce the impact of noise in-coupling, the RF-excitation lines have a capacitive voltage divider on the RF-DC mixer board. This allows applying higher voltages at the inputs of the room temperature boxes, thus higher the signal to noise ratio. In the present case the ring electrode is split and on both half an RF-excitation can be applied. This circuit is shown in fig. 4.12. The DC voltage is filtered with an effective 40 kΩ resistor and a 22 nF capacitor. The choice of two par-

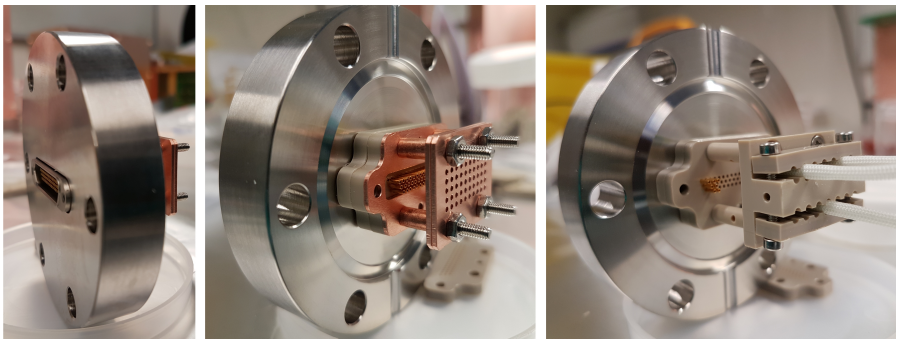

Figure 4.11: Self made vacuum compatible micro-sub-d connectors made from PEEK. From left to right: Front side of the micro-sub-d CF40 flange, vacuum side connector for RF-lines, vacuum side connector für DC-lines.

allel resistors of each 80 kΩ was chosen to have a redundancy in a case of a failure of one resistor. Typically the SMT capacities are not perfect and have in addition to a finite resistance also a small inductance. To suppress better high-frequency components a 220 pF capacitor is mounted parallel to the 22 nF capacitor [64]. If a resonator is connected to the trap electrode a RF-input is not needed. In the case of a non-splitted electrode only the half with the DC-input is used.

All electronics boards have to be fitted in the available space. To assure a good thermal coupling and a good ground connection a single sided layout was chosen except on the edge where the connectors are mounted upside down, see fig. 4.13. Hence it is possible to mount a large part of the board on a solid copper plate. Due to the symmetry of the available space above the trap chamber, a radial design was chosen. The single boards are rotated by 90 degrees to each other. Therefore the single connectors on one board side are slightly repositioned in a way that the connectors are not in one column when the boards are stacked. The arrangement is shown in fig. 4.14. This avoids collisions when inserting the connectors.

4.4.2.1 *Influence on the detection electronics*

Due to the parasitic capacitances between the single electrodes and the two halves of an electrode the connected resonator circuit is influenced by the circuitry of the neighboring electrodes as well. To avoid high AC resistance paths to ground neighboring electrodes should have a low resistance to the AC ground but on the other hand, it is not possible to strong ac ground the these electrodes while still be able to apply an RF-Excitation to it. In order to find a compromise for the used values of grounding capacities the circuitry was simulated in spice (*LTSPICE*) to choose values which still allow strong enough RF-excitations and don't reduce the performance of the detection resonators.

4.4.3 *Thermalisation boards, Filter board*

The incoming coaxial lines which are connected to the amplifier boards are first thermalized on a thermalisation boards. Also the DC lines for the amplifiers are first connected to some filter boards with low-pass filters in order to filter the gate voltages. For these line this filter boards are used as thermal anchor, too.

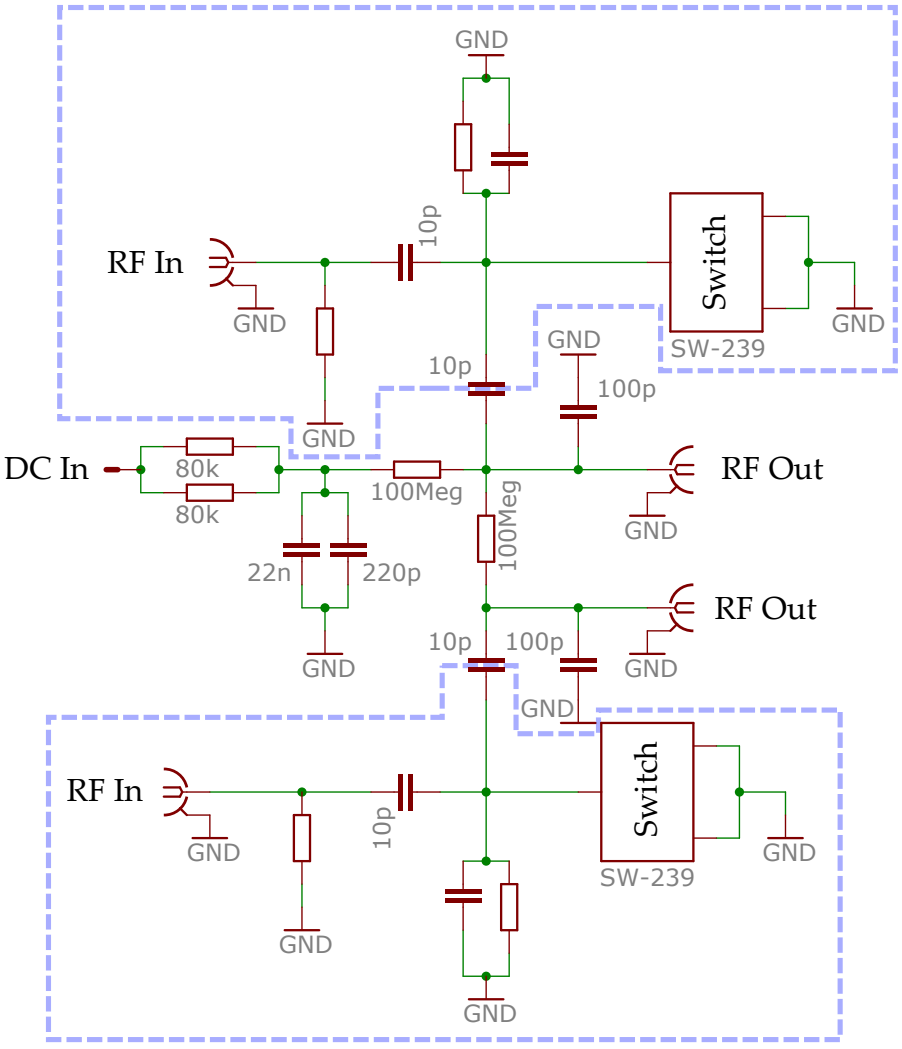

Figure 4.12: Shown is the circuit plan of the case in which a the two segments of a splitted electrode is supplied with one DC-voltage and two RF-excitations. The circuitry which belongs to the RF-In part is surrounded by the blue dotted line. This part contains a capacitive voltage divider and and switch to ground the RF-line, to reduce possible noise on the trap electrode in the case the RF excitation is not used.

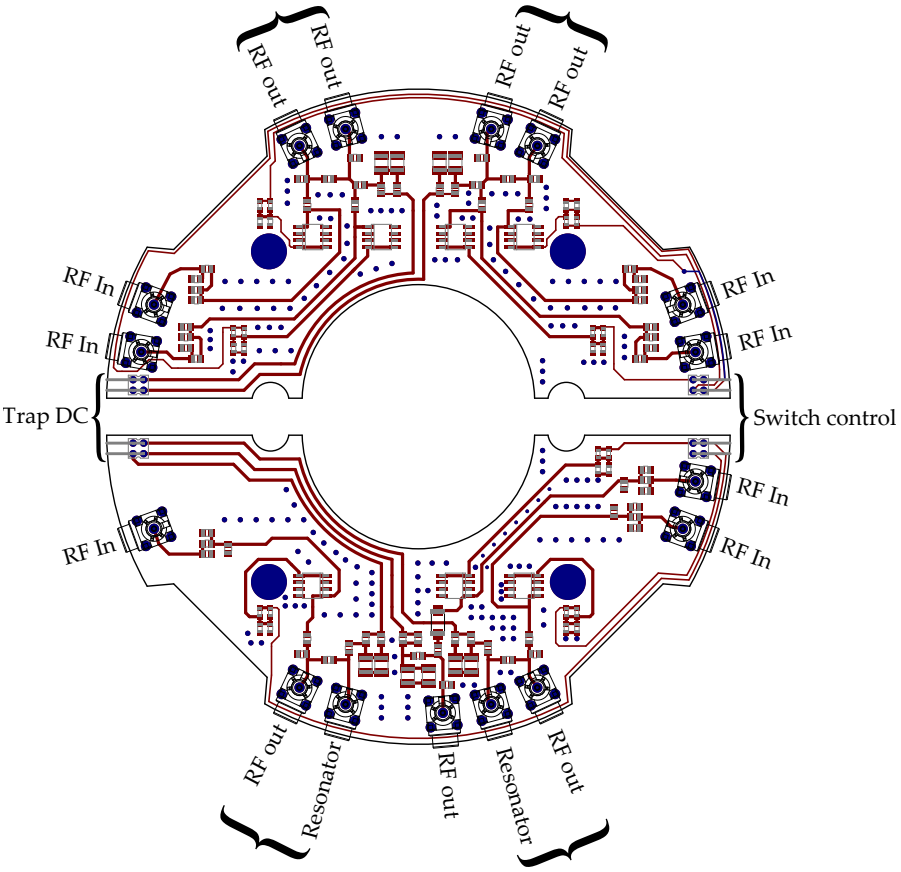

Figure 4.13: Shown is the layout of the RF-DC mixer board. The single connector are labeled corresponding their purpose. The thick curved bracket indicates to output to the two sides of a splited electrode which shares the same DC potential. Two ports are reserved for connecting to one splited electrode where also a resonator is connected. These ports don't have an RF-In connection.

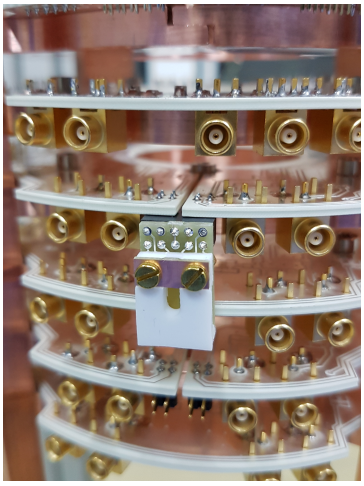

Figure 4.14: Shown is a photograph of the stack of the RF-DC mixer boards without the cables. Clearly visible is the shift of the connectors between the single layers to use the available space as efficient as possible.

Parameter	Value
Number of channels	25
Voltage range	0 to -100 V
Stability	$\leq 4 \cdot 10^{-8} \cdot U_{\text{out}}$ within 10 min
Resolution	$\leq 1.5\,\mu$V
Temperature stability	$\leq 4 \cdot 10^{-7} \cdot U_{\text{out}}/\text{K}$
Noise (0.1 Hz to 10 Hz)	$\leq 1\mu$V

Table 4.1: Required parameters of StaRep.

4.4.4 *Resonator and trap connections*

There is space for up to six axial resonators and three cyclotron resonators. They are located below the trap chamber. To avoid unnecessary long cables the assembly of the trap is matches to the feedthrough pins which are matches to the RF-DC-mixer board. During the first commissioning phase, only two axial resonators and two functional cyclotron resonators were built in. The complete system is currently under development and will be deployed soon. For more details see [54].

4.5 ULTRA STABLE VOLTAGE SOURCE - STAREP

StaRep (Stable Reference for Penning-Trap Experiments) is the voltage source for PENTATRAP [65]. Due to the special requirements on this voltage source, see tab. 4.1, which no commercially available voltage supply could meet, it was developed in parallel to PENTATRAP. The main development was done by the electronics workshop of the Max-Planck-Institut für Kernphysik. This project started within the PhD-thesis of Christine Böhm [66] and was continued within this thesis. StaRep is fully remotely controllable. Each channel is developed as a single replaceable module with a specially designed housing to reduce the influence of sudden temperature changes of the environment. The modules can be plugged in crates. Each crate can take up to five channels. Up to five crates can be controlled by one master controller. One reference module can supply 25 channels. On the front side, each channel has a voltage output and an input for the reference voltage. Noncritical voltages and control signals are connected by the backplane connector. A channel consists of three modules: an HV-module, a DAC module, and a carrier board. The DAC module has a voltage output of 0 V to 10 V. The output of the DAC module will be inverted and amplified by a factor of 10 by the HV-amplifier. The DAC module has two modes: A ramping mode and a precision mode. The precision mode uses two 16-Bit DAC's which are summed with different weights such that one DAC, called coarse-DAC, can cover the full output range, while the remaining DAC, called fine-DAC, covers the range between the steps of the coarse-DAC, see fig. 4.15. With this configuration a theoretical step size of few ten nanovolts is possible. However, the thermal and electronic noise of all used components limit this resolution for practical purposes. The ramping mode uses one DAC to cover the whole voltage range and will be used for the transportation of the ions between the traps. The transportation needs fast voltage changes which disturb the thermal equilibrium of the electronic components. To avoid any effects on the ν_c measurement the precision channel is used while the measurement is

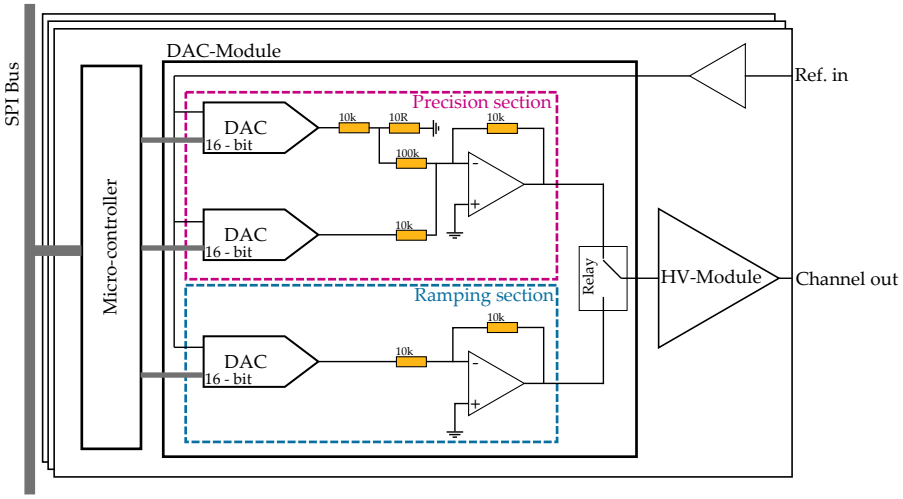

Figure 4.15: Simplified overview of the circuit plan of one StaRep channel. For details see text.

performed. For the transport, a relay at the output of the DAC module will switch from the precision mode to the ramping mode. Still of concern is the HV-module which is shared by the ramping and precision mode. Measurements on the possible thermal effects of the shared HV-module are still in progress. For further details see [65, 66].

4.6 CONTROL SYSTEM

Since there are many ways to fully explore the new PENTATRAP setup the control system needs to be as flexible as possible. An important requirement is that it should be easy to learn and quickly to modify by all group members. To this end it was decided to go for the popular programming language *PYTHON* in combination with *EPICS* (Experimental Physics and Industrial Control System) [67]. The control system was divided into two subparts: The beamline control system and the Penning-trap control system, see also [68].

The beamline is a well-understood system. No new method is planned to be implemented. There are four main groups of devices to control: The HV-supplies, the mass separator, the pulse generator for the pulse drift tube, and the beam diagnostic units. Due to this fixed structure, it was worth to build a graphical user interface. However, there is a simple remote interface which allows triggering the pulse generator to send a bunch of ions into the trap. This interface connects the beamline control system to the Penning-trap control system. In the beamline following parameters need to be controlled or read out,

- 27x High voltages
- 1x Bender magnet current
- 2x MCP diagnostics
- 2x Faraday cups (oscilloscope)
- 3x Timings (pulse generator)

which sums up to 35 control instances.

Parameter	Value
Input channels	8
Dynamic range	110 dB
Sample rates	32 kHz, 48 kHz, 64 kHz, 192 kHz (and some more)
Clock input	Yes
Control	USB

Table 4.2: Important specifications of the *Fireface UC* sound card by *RME*.

To keep the trap control system as flexible as possible it is controlled by a command line interface. The basic structure of the trap control system structure is kept very clean and small. It consists of a trap control class, a configuration script, and an initial script. This base system is then used in different kind of script files. In these script files more experimental routines are implemented, e.g. trap cleaning, ion transportation or ν_c ratio measurement routines. If single routines are successfully debugged and used regularly they are integrated into the base system. With the trap control system following devices needs to be controlled,

- 25x Trap voltages
- 15x RF-Channels
- 35x RF-switches
- 5x FFT-Analyzers
- 1x Pulse generator

which is in total 80 instances to control. The trap base system provides a abstract access to the single instances e.g. the trap control class can receive the trapping depth and set respectively the five trap voltages. A full description with all details of the control system will be given in the master thesis of Menno Door [68].

4.7 FFT ANALYZER

A necessary tool to Fourier transform the ion signal is an FFT analyzer. Commercially available spectrum analyzers commonly have a large frequency range (e.g. 9 kHz - 6 GHz) but a rather unsuitable frequency resolution of 1 Hz and a not sufficient dynamic range. However, audio FFT-analyzers have a good dynamic range and a good frequency resolution. Due to the bad availability and rather high costs of Audio FFT analyzers we utilized a professional sound card, *Fireface UC* by *RME*, the important specifications are listed in tab. 4.2 A very important feature is the clock input. It accepts a frequency of 96 kHz with which the internal clocks are synchronized with phase lock loops. In our setup the 96 kHz are generated by a frequency generator which its synchronized with our 10 MHz frequency standard *SRS FS725*. With this setup, only cyclotron frequency ratio measurements are possible using the double-dip method (see chapter 2.4). In order to use this sound card also for phase sensitive detection methods the data stream needs to be synchronized with a trigger signal.

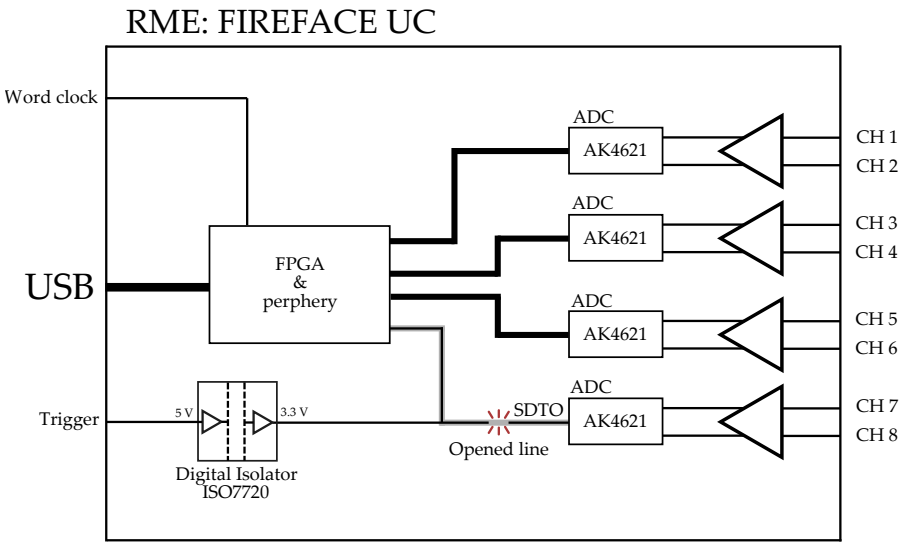

Figure 4.16: Schematic overview of the internal circuit and the modification of the professional sound card *Fireface UC*. For details see text.

4.7.1 *Adding a trigger port to the Fireface UC*

To synchronize the sampled ion signal with a trigger signal it is the most intuitive approach to connect the trigger signal to one free input channel of the sound card. Unfortunately, due to internal filters at the input channel, the trigger signal gets disturbed which makes it difficult to determine the beginning of the trigger signal within one period of the sampling clock. To overcome this problem it was possible to use directly the digital data outline (SDTO) of one ADC (*AK4621*) [69]. The SDTO line is a data line of an SPI bus which continuously output the data between two sample clocks to the FPGA, see fig. 4.17. It is directly connected to the FPGA and is used to input the trigger signal as a digital I/O signal, see fig. 4.16. In the software which analyzes the data stream, the trigger signal is detected as soon as one of the two channels which belongs to the modified ADC is different from zero. To protect the FPGA input pin from any external handling errors a digital isolator is build in, which also converts the common 5 V TTL signal to the 3.3 V level of the FPGA.

An issue with this approach is that there is a small time frame in which the trigger can't be detected. If the trigger arrives in this time gap, the software will detect the trigger signal in one later sample frame, see fig. 4.17. In a phase measurement, this causes an unwanted phase shift. To overcome this problem, the used timing needs to be checked on missing frames and if necessary it gets corrected.

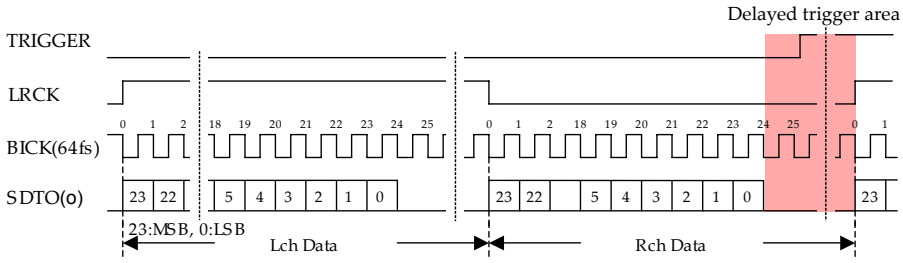

Figure 4.17: Timing diagram of the data stream from the ADC to the FPGA. The red area indicates the time in which no trigger can be detected within the current sampling frame. For details see text.

5 COMMISSIONING OF PENTATRAP

In this chapter the commissioning process of PENTATRAP is discussed. All results have been achieved with the available trap tower [58]. The five traps were all wired and operational. Furthermore, the second and third trap were equipped with an axial detection system.

5.1 COMMISSIONING OF THE BEAMLINE

The composition of the beamline is given in chapter 4.2. The DREBIT was taken in operation following the procedure described in [52]. It is used to produce highly charged ions with a kinetic energy of 6.7 keV/q. The calibration of the 90°-bending magnet (BM) was performed with highly charged ions of natural argon using the MCP diagnostic unit 1 (DU1) at the end of the horizontal beamline. The two Einzel lenses - right before and after the BM - were used to maximize the ion-beam intensity on the DU1.

Natural argon predominantly is composed of ^{40}Ar, which results in well-separated peaks in a q/m-spectrum (fig. 5.1). The maximal achieved resolving power of the BM was about 430 ± 30, [70], for further details see [57].

The next step was the optimization of the vertical beamline. First, the ions were deflected by 90° with the electrostatic quadrupole bender (QB) toward MCP diagnostic unit 2 (DU2). The optimum voltage values for the QB can be experimentally found by watching an ion signal on DU2 (see chapter 4.2). Subsequently, the other optical elements in the vertical beamline were optimized to maximize the intensity of the ion beam on DU2.

Finally, DU2 was moved out of the beam path and the ions were further guided to the cryogenic Faraday cup (cFc). The most time-consuming part was the retarding of the ions with the first pulsed drift tube to a kinetic energy of about 150 eV/q while maintaining a non-zero ion signal on the cFc. This was performed stepwise: the ion kinetic energy was decreased by relatively small values with subsequent tuning of the optical elements in the beamline to maximize the ion signal on the cFc.

5.1.1 *Optimizing the signal-to-noise ratio of the cryogenic Faraday-cup*

The cFc is connected with an approximately 1.5 m long coaxial cable to a charge amplifier HQA-15M-10T from the company *FEMTO*. Unfortunately, this long cable picks up noise dominated by 50 Hz component from the power line. In the beginning the charge amplifier was read out with an oscilloscope *MSO2024* (*Tektronix*), which averaged the signal. Then, already an averaged signal was read out by the control system. Since the time to record the data (< 100 μs) was much shorter than the period of the 50 Hz signal whereas the repetition rate (EBIT breeding time: $\approx$ 40 ms) was in contrary longer, the 50 Hz noise was only partly suppressed by the average process. To overcome this problem an oscilloscope *RTB2004* (*Rohde & Schwarz*) was used instead. One channel of this oscilloscope can be read out approximately 50 times per seconds, which is faster than the repetition rate. Every single triggered waveform is read out and averaged then by the control system. To compensate for the 50 Hz noise, before averaging, an offset to each wave-

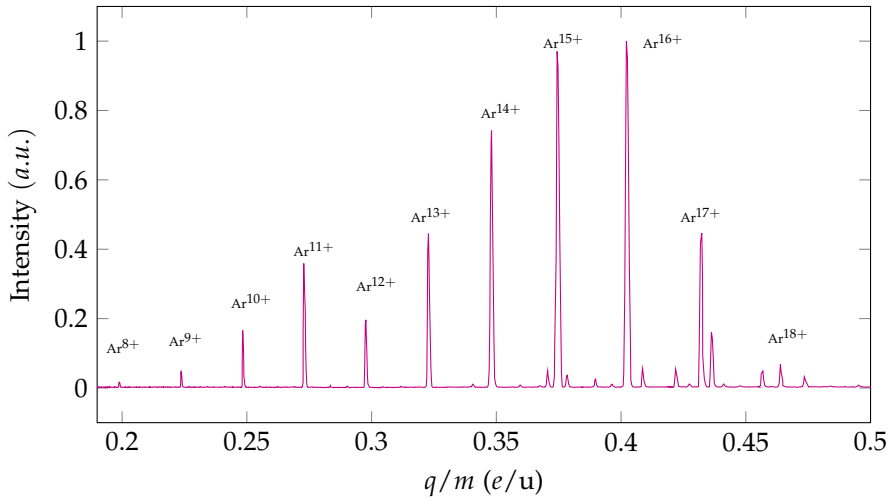

Figure 5.1: Shown is a normalized and calibrated ^{40}Ar spectrum acquired with the Dresden EBIT and the PENTATRAP beamline at the first MCP-diagnostic unit. The breeding time was 500 ms.

form is added to shift the first data point to zero. Thus it is possible to detect slow ion bunches with at least few hundred ions. In this way it was possible to increase the signal-to-noise ratio, which helped to speed up the beamline optimization process significantly.

5.2 CAPTURING OF IONS

As soon as the ion kinetic energy is decreased to about 150 eV/q, which is checked by counting ions on the cFc vs the blocking voltage applied to the cryogenic pulsed drift tube, first attempts to capture ions in one of the traps can be undertaken.

To make the ion trapping possible, the ions further are slowed down to a few eV/q with the cryogenic pulsed drift tube. The correct time of switching the electric potential of the cryogenic pulsed drift tube is determined by varying it around the calculated value in order to maximize the number of captured ions.

In the first attempts to capture ions, the last electrodes of the trap tower were set to some positive voltage to create a potential wall. The ions then were trapped between these electrodes and the cryogenic pulsed drift tube switched to the blocking state. This configuration leads to a long trap with an electrical-field-free region inside where the ions could change there magnetron energy due to patch potentials and thus get lost. This results in a very unstable reproducibility of the number of captured ions.

In the current optimized capture scheme the ions are initially trapped between the electrodes of the first trap and the cryogenic pulsed drift tube. In this scheme the ions have to pass by a cylindrical holding structure which lies on ground. This makes it necessary to use an extra bipolar voltage source for the first trap. In this way the ions are initially trapped in a trapping potential positive with respect to ground. This trap loaded with ions is then lowered to negative potential. In an interplay with the StaRep voltage source the ions are then transported to the finial measurement trap. A schematic of the used potentials can be seen in fig. 5.2.

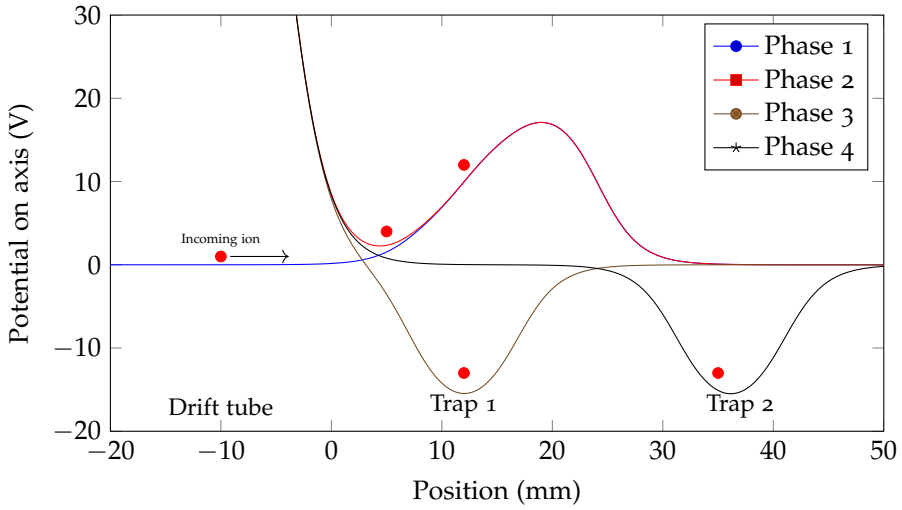

Figure 5.2: Shown are the different time depended phases of the electrical potential on the z-axis which are used to capture ions. Phase 1: Incoming slow (≈10 eV) ions. Phase 2: Pulsing up drift tube. Phase 3: Lowering trap 1 to negative voltages. Phase 4: Transporting ions from trap 1 to trap 2.

In the new trap design the holding structure is floating and thus can be set, e.g., to the potential of the first endcap. In this way the cryogenic pulsed drift tube can be pulsed to negative voltages and it would be possible to maintain the current loading scheme just only with StaRep.

5.2.1 *Detection of captured ions*

After being captured in the first trap, the ions are transported to the second trap, which is equipped with an axial detection system (measurement trap). Note that only ions with a certain mass-to-charge ratio transmitted through the beamline are captured and delivered to the measurement trap. A typical FFT-spectrum after the transport of the ions to the measurement trap is shown in fig. 5.3. The mass-to-charge ratio of the ion and hence the ion species itself can be determined with reasonable accuracy from the measurement of its axial frequency for a given set of trap parameters. The difference in the axial frequency of visible peaks in the FFT spectrum is mainly due to imperfections of the electrical quadrupole field and the difference in axial, magnetron and/or in the cyclotron energy of the trapped ions.

5.2.1.1 *Electrical feedback*

The second and third traps are equipped with axial resonators with a quality factor of 3000 and 1000, respectively. This results in a small width (< 1 Hz for Xe^{+17}) of the thermalized axial-motion dip,see chapter 2.4. Often, especially during the preparation of ions for their frequencies measurement, such narrow dips might be inconvenient to work with, since a very high resolving power and hence a long sampling time of the FFT-spectrum-analyzer are required. Especially in the commissioning phase the optimization of the trap and ion parameters requires high sensitivity of the measurement system to a variation of these parameters. This can be achieved by a substantial increase of the quality factor and the dip width via a realization of positive feedback (see chapter 2.4). To this end, the attenuated output signal of the

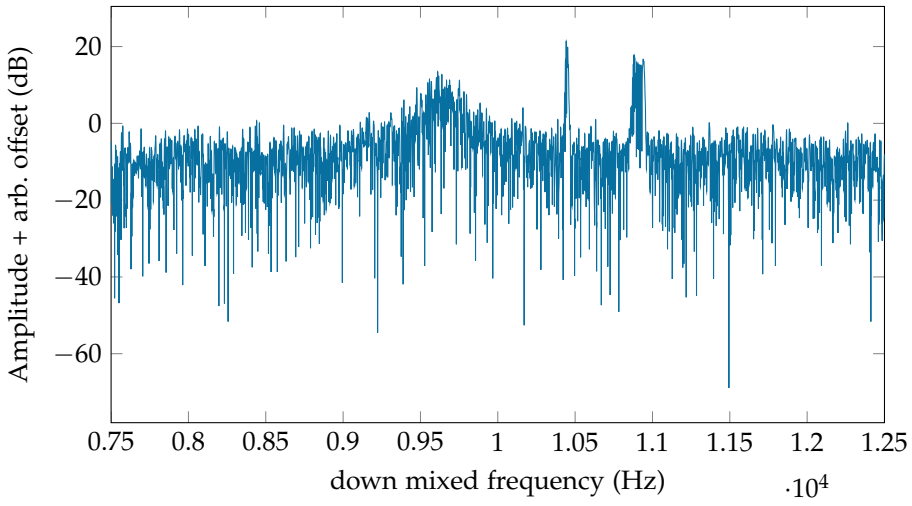

Figure 5.3: Two hot ions visible in the axial frequency spectrum at the guessed voltage of the expected species right of the resonator. The smear out of the peak is due to the change of the frequency within the sampling time of the FFT-Analyzer.

amplifier is fed back to the input with a 90° phase shift (see [23] for details). A schematic circuit of the feedback loop is shown in fig. 5.4. Note that the increase of the quality factor is achieved on the cost of respective increase of the ion axial-motion amplitude.

5.3 SIMPLE PREPARATION OF A SINGLE ION AND FIRST SIDEBAND COOLING

The next step, after capturing ions in the measurement trap, is a rough determination of their magnetron and modified cyclotron frequencies. For this it is important to reduce the number of ions in the measurement trap, ideally to unity. One of efficient ways to do it is a sudden decrease (drop) of the trap depth to some mV near zero. Ions with large axial amplitudes (axially hot ions) will leave the trap while ions with small axial amplitudes (axially cold ions) will remain in the trap. This means that ions, which axial motion is coupled to the axial resonator and hence are thermalized, have a higher probability to remain in the trap after the drop than other ions. The critical parameters to be tuned are the remaining trap depth, ramping speed and the time in which the trap depth remains near zero. These parameters need to be determined experimentally. With this technique it is already possible to prepare a single ion. Since axially hot ions (even if they are not coupled to the axial resonator) appear in the FFT-spectrum as well visible peaks (fig. 5.3), their ion species can easily be found by setting the theoritical value of the trap potential. As soon as an ion is visible in the frequency spectrum the trap potential can be adjusted to shift the ion onto the resonator. As soon as the axially hot ion comes into contact with the resonator, its axial amplitude gets reduced resulting in a change of ion axial frequency due to the inhomogeneity of the electrical field (see. eq. [2.48] for the effect of c_4). Finally it will thermalize near it's "true" axial frequency.

FIRST SIDEBAND COOLING AND DIP DETECTION In the beginning of the commissioning of the measurement trap the modified cyclotron and

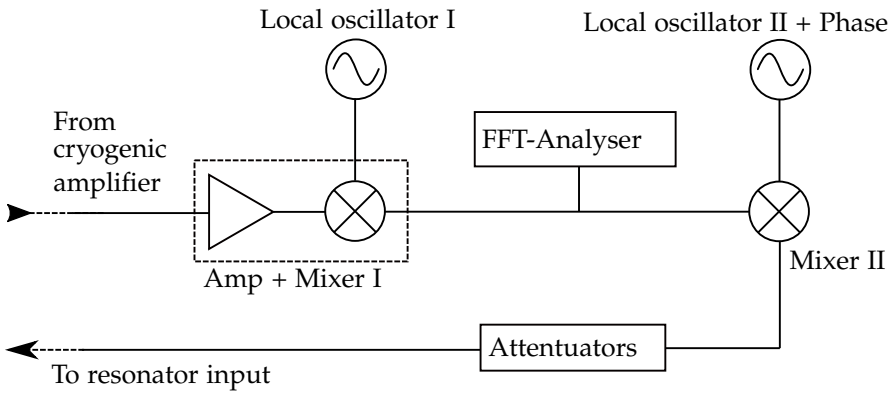

Figure 5.4: Electronic feedback, Amp+Mixer I are integrated on circuit designed by *Stahl Electronics*. Mixer II is a *ZAD-6+* from the company *Mini-Circuits*. The Two Local Oscillators of the same frequency are used to mix the frequency down to the range of the FFT-Analyzer and up again. With the phase of the second local Oscillator the phase can be adjusted. The feedback signal is than attenuated before guided back to the cryogenic amplifier input.

magnetron frequencies of test ions are only known roughly, since the parameters like the magnetic field and optimal tuning ratio are not well known. Still it is possible to cool the radial motions via sideband coupling if the rf coupling frequency is swept over the uncertainty range. Of course, this cooling process gets slower with increasing the frequency sweep range. The transfer of the energy of the radial ion motions to the axial motion results in appearance of a broad peak in the axial frequency spectrum. A slight variation of the trap potential can help to increase the overlap of the frequency sweep with the axial motion. When all motions are successfully cooled, a first dip can be observed, as seen in fig. 5.5 for the very first detected dip at PENTATRAP. Figure 5.6 shows an already optimized dip. With the detection of a dip a first optimization of the tuning ratio (see chapter 2.5.1) can be done to increase the dip depth. A more sophisticated tuning-ratio determination is described in section 5.6.

Note that the technique described in this section needs a fast FFT-Analyzer. Previous tries carried out with a FFT-Analyzer *35670A FFT Dynamic Signal Analyzer*, which hardly can produce a spectrum which one can call a "live" FFT-spectra, failed due to a slow feedback to any manual actions like changing voltages or applying axial excitations bursts. Also during this commissioning phase no high-performance FFT-Analyzer is needed: First tries were successfully done with a 25 Euro sound card *CREATIVE Sound Blaster PLAY! 3* and a small python program which has grown into the presently used sophisticated FFT-software.

5.4 FINDING RADIAL EIGENFREQUENCIES OF THE TRAPPED IONS

Unlike the axial frequency, which can be easily determined by coupling the axial motion to the axial resonator and observing a single dip, the determination of the magnetron and modified cyclotron frequencies is more tricky. The radial motions must be coupled to the axial motion by means of an RF-pulse. Only if the frequency of the coupling pulse is correctly set, the single dip gets split into two symmetric dips (a double dip), which allows one to determine the frequency of the coupled radial motion. Fig. 5.7 shows

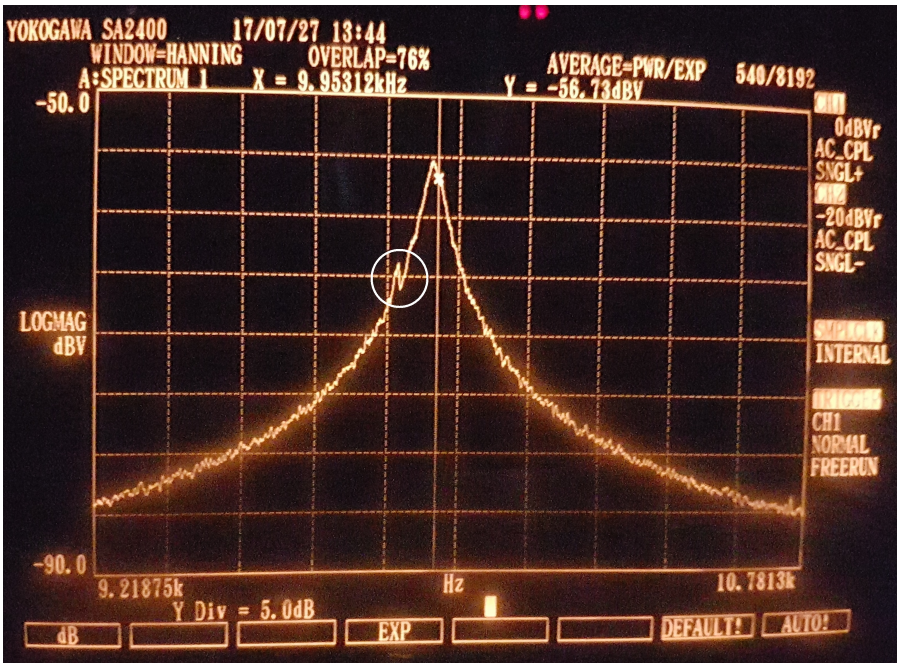

Figure 5.5: Photo of the screen of a *YOKOGAWA SA2400* FFT-Analyzer which shows the very first detected axial dip (white circle) at PENTATRAP with applied positive feedback to boost the quality factor of the resonator. The captured ion was $^{40}Ar^{+12}$.

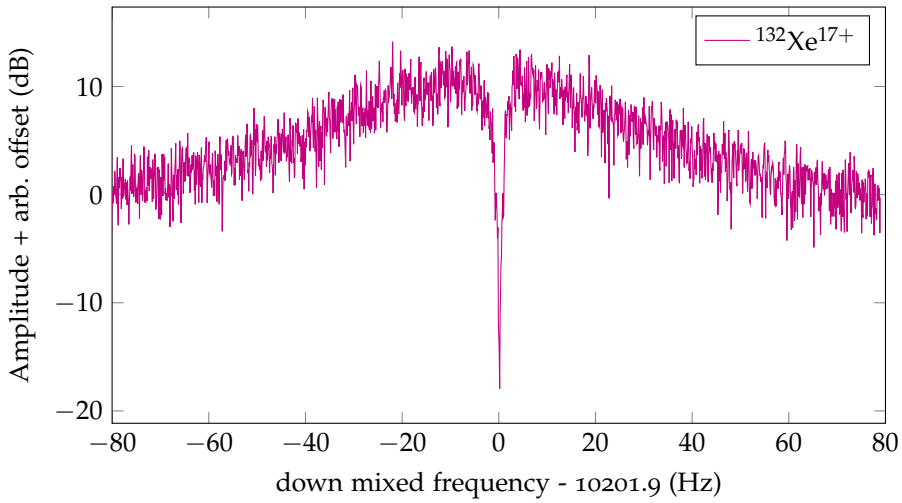

Figure 5.6: Cooled single $^{132}Xe^{+17}$ ion. With applied feedback to boost the quality factor of the resonant circuit from $\approx$ 3000 to $\approx$ 8000. The local oscillator frequency is 471474 Hz.

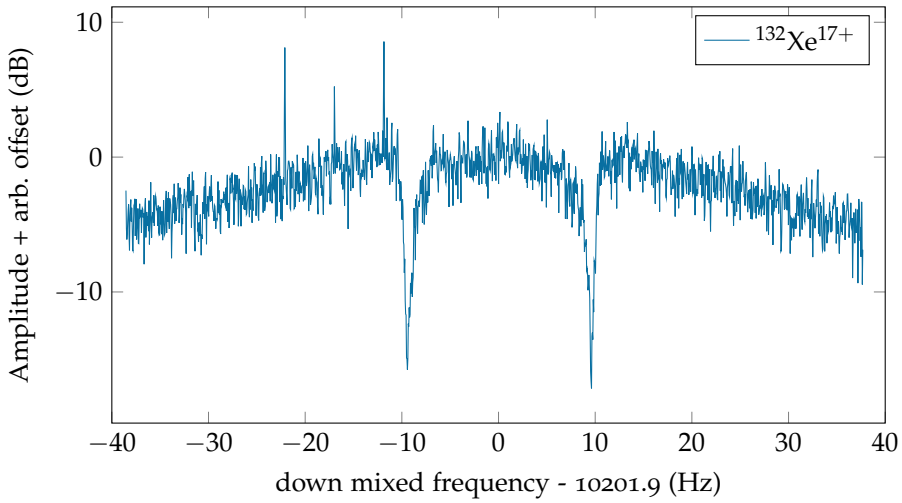

Figure 5.7: Cooled single $^{132}Xe^{+17}$ ion with coupled mod. cyclotron motion to the axial motion with $\nu_{rf} = \nu_+ - \nu_z$. The coupling was driven with the maximal possible driving amplitude of the RF-generator of 10V. Otherwise with the same condition as the spectrum in fig. 5.6 was taken. Additional some noise peaks are visible. The local oscillator frequency is 471474 Hz.

such a cyclotron double dip. Since the width of the double dips is just a half of that of the axial one, the sampling time of the FFT-Anaylser should be increased accordingly to be able to observe the double dips in the frequency spectrum.

The splitting of the double dip is proportional to the Rabi frequency (see eq. [2.37]) and thus depends on the amplitude of the coupling pulse. As seen in fig. 2.6 the frequency range in which the left or right dip becomes indistinguishable from the axial frequency depends on the the driving amplitude. Furthermore, with increase of the detuning factor δ the dip which is further away from ν_z gets less pronounced and at some point vanishes completely. From this follows that the step size of the scan of the coupling frequency can be increased with increasing the driving amplitude.

Typical values for Rabi frequencies in Penning traps like PENTATRAP are in the range of a few Hz to 20 Hz. Thus, a scan makes sense if the coupling frequency is known to few kHz, to be able to find it within a day of scanning. To scan in a rougher range for the resonance frequency it is possible to look for shifts of the axial frequency while trying to drive the chosen radial mode with a dipole frequency sweep. Depending on c_4 an increase of the radius of the radial motion leads to an axial shift, see eq. [2.48]. With a simple binary search it is possible to reduce the uncertainty range down to a range where a scan is economic.

As soon as the axial and one of the radial motion frequencies are found, one can use eq. [2.13] to get a rough idea of the frequency of the other radial motion and to repeat the search procedure.

5.5 CLEANING VIA BROAD-BAND EXCITATION OF THE MAGNETRON MOTION

Even when a single ion dip is prepared and no other ion is visible in the axial frequency spectrum, it doesn't mean that there is only one ion in the trap. Other ions can be stored on large magnetron radii, outside of the harmonic-

potential region, which makes them rather hard to observe. To get rid of those ions one can apply strong white noise within the bandwidth which covers the magnetron frequencies of all expected ions in the trap. This noise excitation will increase the magnetron radii till the ions hit the trap electrodes and get lost. In order not to loose the prepared ion, it is simultaneously sideband cooled. In the case of PENTATRAP five to ten minutes are enough to get rid of unwanted species with a maximal noise amplitude at maximal cooling drive amplitude.

5.6 OPTIMIZATION OF THE TUNING RATIO

At the optimal tuning ratio the anharmonic terms of the electric trap potential are minimized. To test the harmonicity of the electric trap potential, the dependence of the axial frequency vs ion magnetron radius is measured. At the optimal tuning ratio this dependence ideally vanishes. Within this measurement it is important that the excitation of the magnetron motion is large enough to see an effect. On the other hand, it must be small enough that only c_4 is important. For different strengths of magnetron excitation the following tuning-ratio scan is repeated:

1. Set a certain value of the tuning ratio to test the tuning ratio
2. Measure axial frequency $\nu_{z,1}$
3. Set tuning ratio to work tuning ratio
4. Apply magnetron excitation burst
5. Set tuning ratio to test tuning ratio
6. Measure axial frequency $\nu_{z,2}$
7. Determine shift $\nu_{z,2} - \nu_{z,1}$.

Before the measurement all ion motions are cooled. To avoid potential systematic shifts due to different behaviors of the magnetron excitation at different tuning ratios, a working tuning ratio is chosen where all excitations are done. Since the RF-Switches, which ground the RF-lines, have some nonlinear behavior, the duration of the magnetron excitation pulse is changed instead of the amplitude. This sequence was repeated for three different pulse durations and each data set was fitted with a linear function. In the end, the intersection point of the three linear functions was calculated to determine the optimal tuning ratio, see fig. 5.8. The tuning ratio where all three lines intercept and which agrees with a near zero shift, is chosen as the optimal tuning ratio. The measurement for the second trap yields the value of

$$\mathrm{Tr}_{\mathrm{opt}} = 879.759(10)\,\mathrm{mUnit}.$$

5.7 TEMPERATURE MEASUREMENT OF THE THERMAL BATH OF THE AXIAL RESONATOR

The effective temperature of the detection system is interesting because it defines the motion amplitudes of the thermalized ion. Furthermore, the magnitude of the amplitudes determines the influence of the imperfections of the

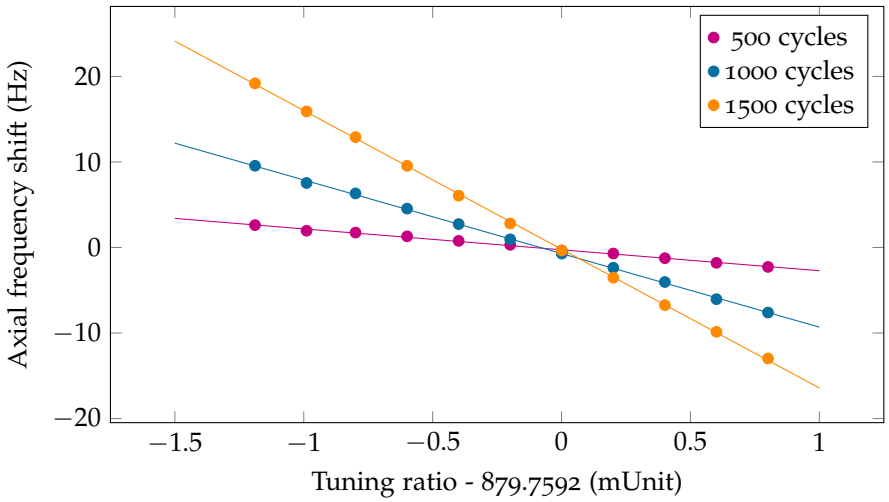

Figure 5.8: Tuning ratio scan ($^{131}Xe^{+17}$) with same amplitude (2.5 V at RF-Generator output) but different cycles of the magnetron excitation burst. The solid line is a linear fit to the corresponding data points.

trapping fields. The knowledge of the amplitudes is therefore relevant for the studies of systematic effects. Since the setup is submerged in liquid helium at one atmosphere pressure, the naive assumption is a temperature of 4.2 K. However, the thermal equilibrium is determined by the thermal coupling of the axial resonator to the liquid helium and by several cables which connect the cryogenic electronic to 300 K. Another relevant heating source is the axial amplifier which produces approximately 10 mW of heat power. To measure the temperature of the axial detection system, the scattering of the magnetron radius after an excitation pulse over many measurements is determined. Every measurement starts from a sideband cooled magnetron motion. Only changes in the radius due to the finite temperature of the axial detector system change the starting conditions. These changes are the scattering which are later measured and analyzed to determine the temperature of the axial resonator. To measure the excited magnetron radius, a c_4 anharmonicity is introduced on purpose by detuning the optimal tuning ratio Tr_{opt} to the tuning ratio Tr_{c_4}. With the help of the optimal tuning ratio Tr_{opt} and the calculated d_4 parameter [61], the c_4 of Tr_{c_4} can be determined. The first anharmonicity term c_4 was chosen in a way that the shift with the applied excitation pulse is about 40 Hz. The measurement procedure starting from a cold ion goes as follows:

1. Measure $\nu_{z,cool}$ of cold ion at tr_{c_4}
2. Apply a magnetron dipole pulse at tr_{opt}
3. Measure ν_z^i at tr_{c_4}
4. Cool all motions of the ion.

This procedure is repeated till enough statistics is collected. Similar to the tuning-ratio measurement the excitation pulse is applied at the optimal tuning ratio to suppress any effects due to the excitation because of the c_4 term. The difference

$$\Delta\nu_z^i = \nu_{z,cool} - \nu_z^i \tag{5.1}$$

is calculated for further steps. With eq. [2.48] for the magnetron motion it is possible to determine the magnetron radius ρ_- and the scatter of the magentron radius $\delta\hat{\rho}_-$ from the frequency shifts $\Delta\nu_z^i$,

$$\hat{\rho}_- = \sqrt{\frac{2}{3}\frac{C2}{C4}\frac{\overline{\Delta\nu_z}}{\nu_{z,\mathrm{cool}}}}, \tag{5.2}$$

$$\delta\hat{\rho}_- = \frac{\hat{\rho}_-}{2}\frac{\sigma(\overline{\Delta\nu_z})}{\overline{\Delta\nu_z}}, \tag{5.3}$$

where $\overline{\Delta\nu_z}$ and $\sigma(\overline{\Delta\nu_z})$ are the mean value and the standard deviation of all measured values of $\Delta\nu_z^i$. Since the radius distribution in the magnetron motion is measured it needs to be related to the axial motion by:

$$\delta\hat{z} = \sqrt{\frac{\nu_+ - \nu_-}{\nu_z}}\delta\hat{\rho}_- \approx \sqrt{\frac{\nu_+}{\nu_z}}\delta\hat{\rho}_-. \tag{5.4}$$

Starting from the Boltzmann distribution over the probability density function and averaging over one period of the axial motion, the amplitude can be related to the FWHM of the Gaussian distribution, for details see [37]:

$$2\hat{z} \approx \frac{2.35}{\pi\nu_z}\sqrt{\frac{kT_z}{2m}}, \tag{5.5}$$

where the factor 2.35 comes from the conversion from σ to FWHM. Combining the last two equations gives a relation between the scatter of the magentron radius and the temperature of the axial detector,

$$T_z = \left(2.673\sqrt{\frac{\nu_+}{\nu_z}}\delta\hat{\rho}_-\nu_z\right)^2 \cdot \frac{2m}{k}. \tag{5.6}$$

This can be expressed with the help of eq. [5.3] and eq. [5.4] as a dependence of the standard deviation of the measured shift $\sigma(\overline{\Delta\nu_z})$,

$$T_z = 2.373\frac{m}{k}\frac{c_2}{c_4}\frac{\nu_+}{\overline{\Delta\nu_z}}\sigma(\overline{\Delta\nu_z})^2. \tag{5.7}$$

With the parameters and measured values listed in tab. 5.1 the temperature of the axial detector can be then calculated to

$$T_z = 6.2(1.6)_{\mathrm{stat}}\,\mathrm{K}.$$

This axial temperature results in the following amplitudes:

$$\begin{aligned}\hat{z} &= 10.9(1.4)\mu\mathrm{m}\\ \hat{\rho}_{-,+} &= 2.0(3)\mu\mathrm{m}\end{aligned}$$

where the radial motions are cooled via sideband coupling to the axial resonator.

5.8 SUMMARY OF THE COMMISSIONING OF PENTATRAP

The ion loading was implemented successfully and works reliably now for elements which are practically not limited in the availability. Furthermore, the transport between the single traps was demonstrated and is used reliably in the loading scheme. First ions were trapped and the eigenfrequencies were found. The tuning ratio and the temperature of the axial detector system were successfully determined. The temperature which is in the range

Parameter	Value
Measurement points	31
$\overline{\Delta\nu_z}$	40.3 Hz
$\sigma(\overline{\Delta\nu_z})$	0.52 Hz
ν_+	13956565 Hz
ν_z	481554.26 Hz
c_2	$-1.496 \cdot 10^{-2}\,(1/mm^2)$
d_4	$8.406 \cdot 10^{-4}\,(1/mm^4)$

Table 5.1: Measured shifts and values of $^{131}Xe^{17+}$ with the calculated coefficients c_2 and d_4 from [61].

of the best reachable temperature of 4.2 K approves the thermal concept of the cryogenic setup. Pending characterization measurements are the measurement of the B_1 and B_2 term of the magnetic field which are needed for further systematic studies. Furthermore, to load ions from small ^{163}Ho source ($\approx 10^{14}$ atoms) the beamline efficiency needs to be determined and probably improved. To test the performance of PENTATRAP, a test mass-ratio measurement was carried out. Its results are discussed in the following chapter.

6

FREE CYCLOTRON RATIO MEASUREMENT OF ^{132}XE OVER ^{131}XE

To test the performance of the new apparatus, cyclotron frequency ratio measurements and thus mass ratio measurements of nuclei pair with known masses were carried out. As nuclei pair the two isotopes of xenon ^{132}Xe and ^{131}Xe were chosen since their mass is already known witha relative uncertainty of $1 \cdot 10^{-10}$ [71]. Furthermore, xenon can be easily introduced and ionized in one of PENTATRAP's EBITs and with a natural abundance of 26.4% for ^{132}Xe and 21.3% for ^{131}Xe, natural xenon gas can be used instead of an expensive artificial enriched xenon gas. To load one or the other xenon isotope just a small adjustment of the current of the bender magnet is necessary. As charge states $^{132}Xe^{17+}$ and $^{131}Xe^{17+}$ were chosen.

Only one trap, the one with the best performance of the attached detection system, which is the second trap, was used as measurement trap. For the measurements reported here, the single-trap-measurement switching scheme, described in section 4.1.2, was applied. With this switching scheme several measurement procedures where evaluated which are described in the following. In all presented measurements the magnetron frequency is only measured every four hours by determining the axial and magnetron double dip (see section 2.4). Due to its stability over time and its suppressed impact on the final uncertainty due to $\nu_- / \nu_+ \approx 10^{-4}$ on the final ratio, this measurement interval is sufficiently short. The measurement schemes are optimized for measuring ν_z and ν_+ as fast as possible.

The data analysis was carried out similar to the one described in chapter 3.4. The data is split into groups and a polynomial function is fitted to each group to model the magnetic field drift [39]. However, in difference to the analysis discussed in chapter 3.4, all following data analyzes were automated and the degree of the polynomial function was determined with the F-test for each group of the data-set.

6.1 DOUBLE DIP TECHNIQUE

To determine ν_c via the invariance theorem (see eq.2.15) all eigenfrequencies of an ion in a Penning trap have to be measured. Since only an axial detection system is available, only the axial frequency can be directly measured by detecting an axial dip. However, the radial frequencies need to be coupled to the axial mode first, followed by the detecting of a double dip, described in chapter 2.4.

In the sequential double-dip technique, one measurement e.g. of an axial dip consists of a number of acquisitions of the FFT-analyzer which are immediately averaged. The axial frequency is measured once before the modified cyclotron double dip measurement and once after. This allows the interpolation of the axial frequency to the time of the measurement of the modified cyclotron frequency. After these three measurements, the ion specie is switched and the procedure is repeated for the other ion specie. The difference of this sequential procedure to the alternating double-dip technique is that one acquisition of an axial dip is followed by one acquisition of a double dip. This sequence is then repeated and the single acquisitions are averaged

Parameter of the double dip method	sequential		alternating	
Total measurement time	33 std.		45 std.	
Number of ν_c ratio measurements	157		80	
Number of analysis groups	22		16	
Time per analysis group	140-214 min.		104-139 min.	
Instrumental uncertainty	$1.845 \cdot 10^{-09}$		$1.435 \cdot 10^{-09}$	
Average χ^2_{red} of fits	μ: 4.95 σ: 2.24		μ: 2.54 σ: 1.25	
Setting	ν_z	ν_+	ν_z	ν_+
Number of averages	15	15	20	20
FFT sampling time	5.46 sec	10.92 sec	20 sec	20 sec

Table 6.1: Used settings for the measurements of ν_z and ν_+. The average χ^2_{red} is the mean(μ) and the standard deviation(σ) of all the $\chi^2_{red,i}$ of each analysis groups.

afterwards. The idea which should be tested with the comparison of the sequential to the alternating measurement scheme is the potential higher suppression of axial frequency fluctuations in the alternating measurement scheme, due to the smaller time difference between a single ν_+ to a single ν_z measurement. Also, the alternating measurement scheme allows for testing different post process average methods.

The used settings and parameters of these two measurement schemes are listed in tab. 6.1. The measured free cyclotron frequency ratio of the sequential measurement R_{seq} and alternating measurement R_{alt} are,

$$R_{\mathrm{seq}} = 1.00763256931(12_{\mathrm{stat}})$$
$$R_{\mathrm{alt}} = 1.00763256898(35_{\mathrm{stat}}).$$

They are in excellent agreement with each other, however the sequential measurement scheme has a factor of three reduced uncertainty. The reason for this reduced uncertainty is the decreases number of measurements due the longer sampling time and higher number of averages which only slightly increasing the instrumental uncertainty but not enough to compensate the loss in number of measurements. The compilation of the single free cyclotron frequency ratio measurements are shown in fig. 6.1 for the sequential and in fig. 6.2 for the alternating measurement. Furthermore, with the value of the mass excess of $ME(^{131}\mathrm{Xe}) = -88413.558(9)\,\mathrm{keV}$ [72], the summed electron binding energies $E_{B,e} = 2.994(10)\,\mathrm{keV}$ [73] and rest masses of the missing electrons, the atomic mass difference of $\Delta M = M(^{132}\mathrm{Xe}) - M(^{131}\mathrm{Xe})$ can be calculated to

$$\Delta M_{\mathrm{seq}} = 930628.711(16_{\mathrm{stat}})\,\mathrm{keV}/c^2,$$
$$\Delta M_{\mathrm{alt}} = 930628.671(43_{\mathrm{stat}})\,\mathrm{keV}/c^2,$$
$$\Delta M_{lit} = 930628.691(10)\,\mathrm{keV}/c^2.$$

The comparison with the literature value shows a relative offset $(\Delta M_{lit} - \Delta M)/M_{^{131}\mathrm{Xe}}$ on the $1.6 \cdot 10^{-10}$ level for both measurements, however they agree within their uncertainties.

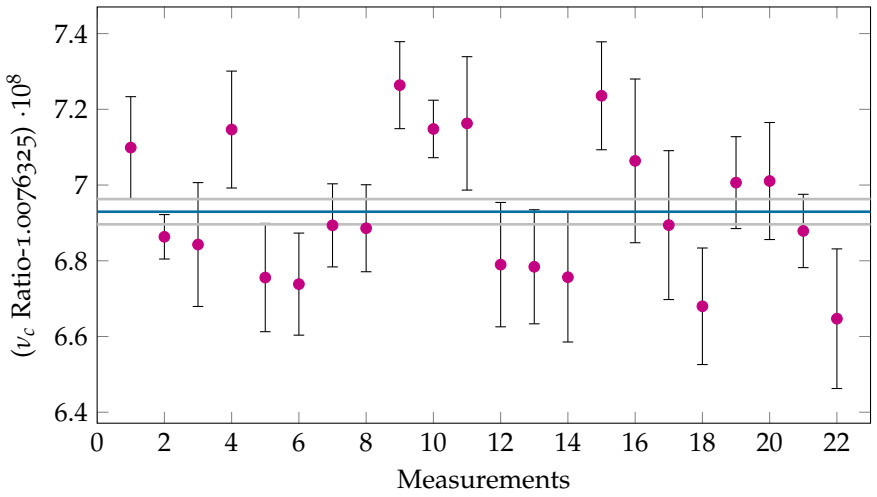

Figure 6.1: Shown are all measured ν_c ratio determinations with the sequential double dip technique. Each point is a result of a polynomial fit to a group of ν_c measurements of $^{132}Xe^{17+}$ and $^{131}Xe^{17+}$. With the blue line, the mean value is indicated, while the grey lines indicate the error of the mean.

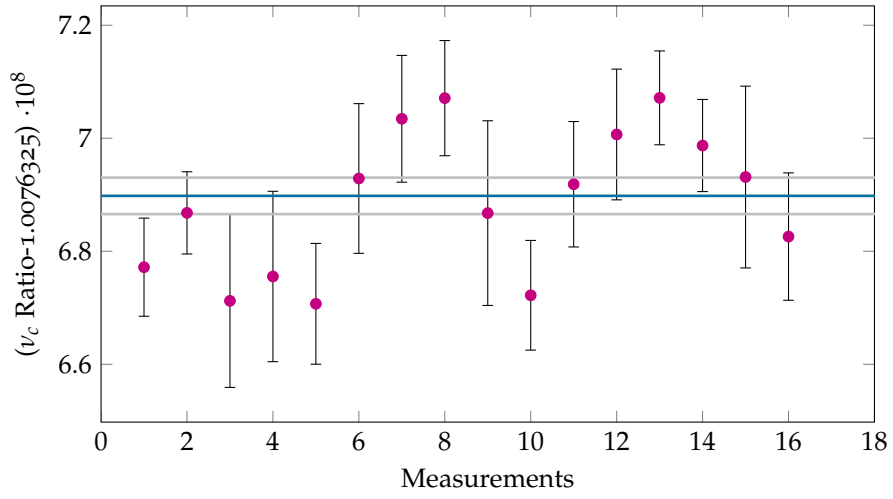

Figure 6.2: Shown are all measured ν_c ratio determinations with the alternating double dip technique. Each point is a result of a polynomial fit to a group of ν_c measurements of $^{132}Xe^{17+}$ and $^{131}Xe^{17+}$. With the blue line, the mean value is indicated, while the grey lines indicate the error of the mean.

6.2 PNP TECHNIQUE WITH SIMULTANEOUS AXIAL MEASUREMENT

In comparison with the usually used PnP technique [74], the following PnP measurements have been combined with a simultaneous dip-detection during the phase accumulation time. The applied pulse sequence scheme is shown in fig. 6.3. Former measurement schemes measured the axial frequency with the dip-technique before the phase sensitive measurement of the modified cyclotron frequency. The advantage of this new modified scheme is that during the measurement of the axial frequency the ion is on the same radius as during the measurement of the modified cyclotron frequency. This reduces the influence of the higher anharmonic terms $C_{4,6}$ of the electrical field. Moreover, the impact of the time-dependent drift of the axial frequency is suppressed due to the simultaneous measurement of ν_+ and ν_z. To reach a suitable frequency resolution for the dip detection, this simultaneous measurement needs at least a certain phase accumulation time. The minimal required phase accumulation time depends on the dip-width and with that on the q/m ratio of the ion and the quality factor of the attached resonator. Furthermore, a certain number of averages are needed to clearly determine the axial frequency. This modification was only possible due to the full control over the self-programmed FFT-analyzer discussed in chapter 4.7.

6.2.1 *Phase measurement and phase unwrapping*

A phase measurement of the ν_+ frequency starts with imprinting a start phase on the ions reduced cyclotron eigenmotion. This is followed by a phase accumulation time till the readout procedure of the phase starts. Within the phase accumulation time, an axial dip spectrum can be acquired. Thus, it can be used in case it will be averaged with other acquired dip spectra to determine the axial frequency in parallel to the ν_+ frequency. The procedure to read out the phase is starting with the coupling of the modified cyclotron motion to the axial motion with a lower sideband coupling of the length of a π-pulse. After a small time delay (typically 20 ms) to reduce the influence of the π-pulse on the detector system, the FFT-analyzer starts its acquiring and the determination of the phase of the down-mixed axial frequency relative to the FFT-sampling frequency. After the acquiring the modified cyclotron motion of the ion is sideband cooled and the procedure is repeated with a suitable number of averages. The illustration of this pulse scheme is shown in fig. 6.3.

PHASE UNWRAPPING While only the modulo of 2π of the total phase can be measured, the total phase can be written as

$$\phi_{\text{total}} = 2\pi\nu_+ t_{\text{total}} = 2\pi N_{\text{total}} + \phi_{\text{measured}}. \tag{6.1}$$

The time t_{total} is the total time between the setting of the start phase and the read out of the final phase. This time is in general unknown and therefore the number of complete periods N_{total} in this time, too. The reason is that the dipole pulse and the couple pulse at the position of the ion are not known well enough to calculate the action on the ion with the required accuracy. To overcome this problem the phase difference between two phase measurements with different phase accumulation times are determined. Only the time distance t_1 of the first measurement and t_2 of the second measurement

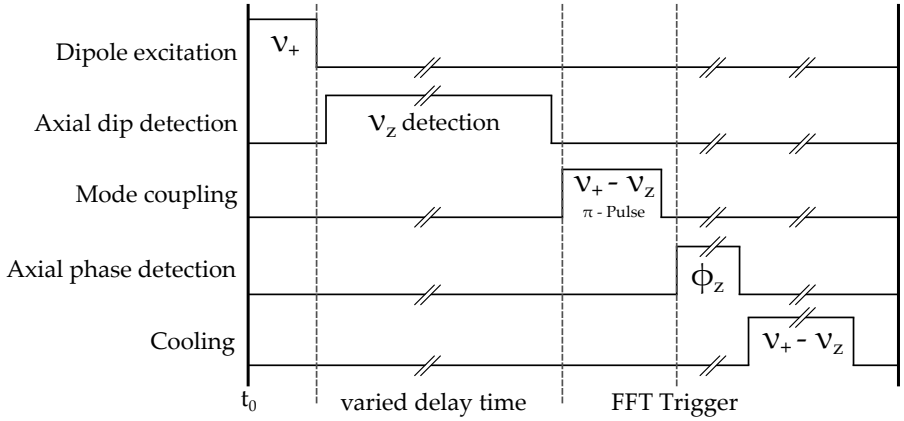

Figure 6.3: Diagram of the pulse sequence which is used in a PnP measurement with simultaneous axial-dip detection during the varied delay time between the dipole excitation and coupling pulse. For details, see text.

between the dipole pulse and the coupling pulse is different. The total time of one each of these measurements is,

$$t_{\text{total},1} = t_1 + t_x, \tag{6.2}$$
$$t_{\text{total},2} = t_2 + t_x, \tag{6.3}$$

where t_x is the unknown time component in which stays the same between the two measurements. In the same way N_{total} can be written with an unknown component N_x as,

$$N_{\text{total},1} = N_1 + N_x, \tag{6.4}$$
$$N_{\text{total},2} = N_2 + N_x, \tag{6.5}$$

where $N_{1,2}$ are the total turns in the times $t_{1,2}$. With this substitution, the total phase can be written as,

$$\phi_{\text{total},(1,2)} = 2\pi\nu_+(t_{1,2} + t_x) = 2\pi(N_{1,2} + N_x) + \phi_{\text{measured},(1,2)}. \tag{6.6}$$

In the difference all the unknowns vanishes including unknown phase offsets due the phase conversion to the axial frequency. Finally the measured frequency ν_+ can be written as

$$\omega_+ = 2\pi\nu_+ = \frac{2\pi N_2 + \phi_{\text{measured},2} - 2\pi N_1 - \phi_{\text{measured},1}}{t_2 - t_1}. \tag{6.7}$$

Usual $\phi_{\text{measured},1}$ is chosen as reference phase and N_1 and t_1 are subtracted as offset from N_2 and t_2,

$$\Delta t = t_2 - t_1, \tag{6.8}$$
$$N = N_2 - N_1, \tag{6.9}$$
$$\Delta\phi = \phi_{\text{measured},2} - \phi_{\text{measured},1}. \tag{6.10}$$

In the evaluation then Δt, $\Delta\phi$ and N is used.

If N is known, the frequency can be determined only by two measurements, the phase reference measurement and a measurement at a longer phase accumulation time. But N in general is unknown, but it can be determined by at least three phase measurements at three different accumulation times. To avoid any ambiguity in this method, it is recommend to do more

t (s)	$\phi_z(rad)$	Δt(s)	$\Delta\phi_z(rad)$	N
0.01	4.50(9)	0	0	0.00(2)
0.5	3.17(5)	0.49	-1.33(10)	6786851,94(2)
1	2.7(1)	0.99	-1.78(15)	13712210,93(2)
2.32	5.82(7)	2.31	1.33(12)	31995157,95(2)
4.81	1.92(8)	4.8	-2.58(12)	66483445,95(2)
6.45	3.25(9)	6.44	-1.25(13)	89198622,97(2)
9.57	0.63(12)	9.56	-3.87(15)	132412862,98(2)
12.46	3.6(1)	12.45	-0.90(14)	172441437,01(2)
15.76	2.57(8)	15.75	-1.92(12)	218148805,98(2)
17.51	3.60(8)	17.50	-0.90(13)	242387562,01(2)
20	5.94(14)	19.99	1.45(17)	276875849,01(3)

Table 6.2: Example of an unwrapping table of $^{132}Xe^{17+}$ with a determined ν_+ frequency of 13850717.82 Hz. Each measured phase is an average of 20 single measurements.

than three different accumulation times. Moreover the chosen times should not be multiple of each other. A result of such a measurement is exemplary listed in tab. 6.2, where N is calculated as

$$N = \frac{2\pi\Delta t\nu_+ + \Delta\phi}{2\pi}. \tag{6.11}$$

The frequency ν_+, which initial value is determined by a double dip measurement, is then scanned near its initial value to find the minimum in the deviations d of N to an integer number,

$$d = \sqrt{\sum_{k=1}^{K} (\lceil N_i \rfloor - N_i)^2}, \tag{6.12}$$

where k denotes the different phase accumulation time measurements. Since there are several local minima standard optimization algorithms are failing and slower global optimization algorithm needs to be used. It turns out that a simple generation of a list for d for different frequencies near the the expected frequency and a search in the list for the minimal value gives the fastest and most robust result.

6.2.2 *Measurement setup*

In fig. 6.4 the schematic measurement setup is shown, with which the pulse sequence in fig. 6.3 is produced. This setup is very similar to the one described in [23]. Each frequency generator, the FFT-analyzer and the pulse generator are synchronized with a 10 MHz rubidium standard (*FS725*) from *Stanford research systems*. This frequency standard produces a 10 MHz signal and via a second output a pulse-per-second (PPS) signal. The pulse generator will be triggered once by a PPS signal only if it was armed via its software communication interface in advanced of a PPS pulse. The pulses produced by the pulse generator will then trigger the start of the dipole pulse and the acquiring of the FFT-Analyzer. In this way the start of the pulse sequence is synchronized with the PPS signal. This has the advantage that

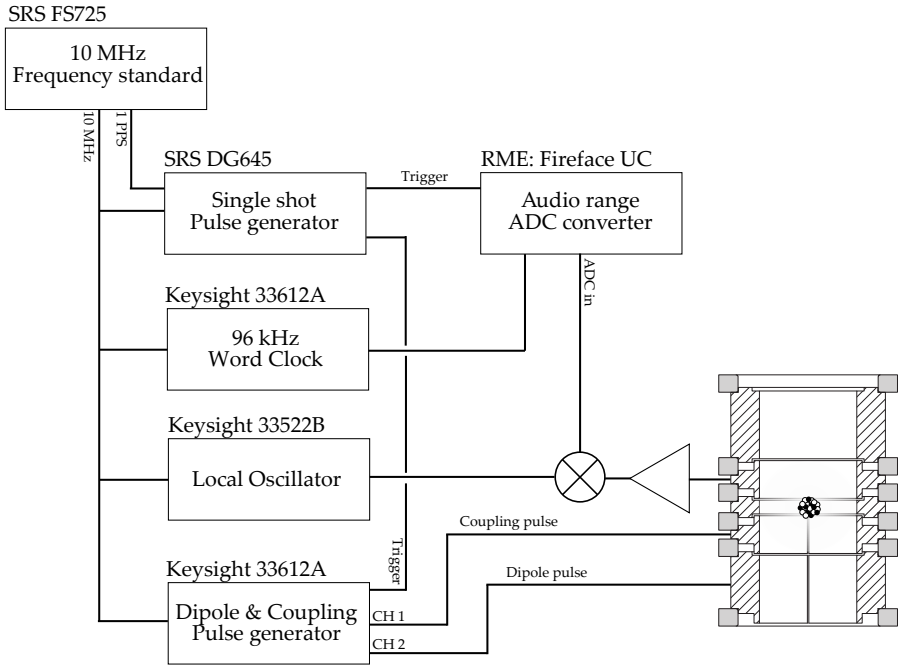

Figure 6.4: Schematic overview over the used devices and their relevant connections for the PnP method. For details see text.

every phase of a continuously generated frequency which has an even cycle number in one second is stable. This is the case for the 96 kHz FFT-reference clock and with it the internal sampling clock of the FFT-Analyzer and the local oscillator which controls the down mixing of the axial frequency of the ion to the audio frequency range. This is important since a change of the phase of this frequencies would also change the measured phase. The delay between the dipole and the coupling pulse is done internally in the two-channel rf-generator *33612A* by *Keysight*.

6.2.3 *PnP measurement results*

Similar to the double-dip technique, for the phase measurements a sequential and an alternating scheme was tested. This allows to to test the influence of the measured phase drifts which depend directly on the drift of the axial frequency. In the sequential scheme, first the a certain number reference phase measurements are averaged and a certain number the phase with longer phase accumulation time which will be called measurement phase in the following. While in the alternating scheme a reference phase measurement is followed by a measurement-phase measurement. After accumulating enough data, the ion species were switched in the measurement trap.

For the following measured free cyclotron frequency ratios for the sequential method R_{seq} and for the alternating method R_{alt} the used parameters and settings are listed in tab. 6.3. The final results of the average process of the fit results, shown in fig. 6.5 for the sequential and in fig. 6.6 for the alternating method, are,

$$R_{\mathrm{seq}} = 1.007632568997(29_{\mathrm{stat}})$$
$$R_{\mathrm{alt}} = 1.007632569117(35_{\mathrm{stat}}).$$

Parameter of the PnP method	sequential		alternating	
Total measuring	15 std.		15 std.	
Number of ν_c ratio measurements	40		29	
Number of analysis groups	9		9	
Time per analysis group	76-101 min.		87-116 min.	
Instrumental uncertainty	$1.865 \cdot 10^{-10}$		$1.066 \cdot 10^{-10}$	
Average χ^2_{red} of fits	μ: 3.19 σ: 2.25		μ: 2.18 σ: 1.71	
Setting	ϕ_{ref}	ϕ_{meas}	ϕ_{ref}	ϕ_{meas}
Number of averages	40	20	20	20
Phase accumulation time	0.01 sec	10 sec	0.01 sec	20 sec

Table 6.3: Used settings for the measurements of ϕ_{ref} and ϕ_{meas} for the sequential phase method and the alternating phase method. The average χ^2_{red} is the mean(μ) and the standard deviation(σ) of all the $\chi^2_{red,i}$ of each analysis groups.

Equal to the double-dip method, $\Delta M = M(^{132}\mathrm{Xe}) - M(^{131}\mathrm{Xe})$ can be calculated to

$$\begin{aligned}\Delta M_{\mathrm{seq}} &= 930628.6732(67_{\mathrm{stat}})\,\mathrm{keV},\\ \Delta M_{\mathrm{alt}} &= 930628.6879(71_{\mathrm{stat}})\,\mathrm{keV},\\ \Delta M_{lit} &= 930628.691(10)\,\mathrm{keV}.\end{aligned}$$

The comparison with the literature value shows a relative offset $(\Delta M_{lit} - \Delta M)/M_{^{131}\mathrm{Xe}}$ on the $1.5 \cdot 10^{-10}$ level for the sequential measurement and $2.9 \cdot 10^{-11}$ for the alternating measurement scheme.

6.3 SUMMARY OF ^{132}XE^{17+} VERSUS ^{131}XE^{17+} MEASUREMENTS

In fig. 6.7 PENTATRAPs measurement results of $\Delta M(^{132}\mathrm{Xe} - ^{131}\mathrm{Xe})$ are compared to two already existing ratios from two different Penning-trap mass spectrometers: The measurement by the FSU trap [71] and the measurement of SHIPTRAP [75]. Also the literature value is indicated [72]. The here reported results of PENTATRAP are in agreement with the literature value within the error bars. The statistical advantage of the phase sensitive measurement over the double-dip technique is obvious: Due to the higher resolution (lower instrumental uncertainty) within one cyclotron measurement by far less measurement time is needed to reach a relative mass uncertainty in the 10^{-11} regime. The advantage of the simultaneous measurement of the axial frequency during the phase accumulation time over an extra axial measurement before and after the phase measurement has still to be shown. Also, at the present precision level, a difference between the sequential and alternating measurement scheme is not visible. This result gives a good hint, that already now, PENTATRAP is ready to perform mass measurements at the relative 10^{-10} uncertainty level without many expected corrections due to systematic shifts.

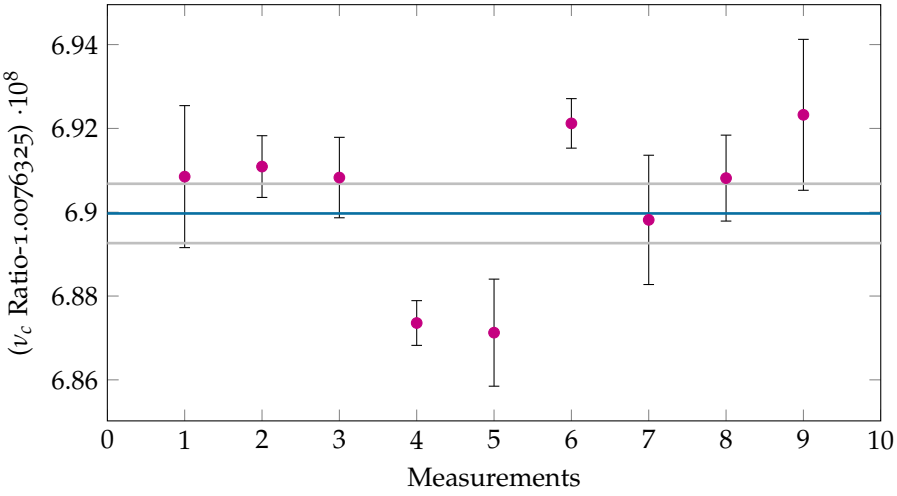

Figure 6.5: Shown are all measured single ratio determination with the sequential PnP technique with simultaneous axial measurement. With the blue line, the mean value is indicated while the grey lines indicates the error of the mean determination.

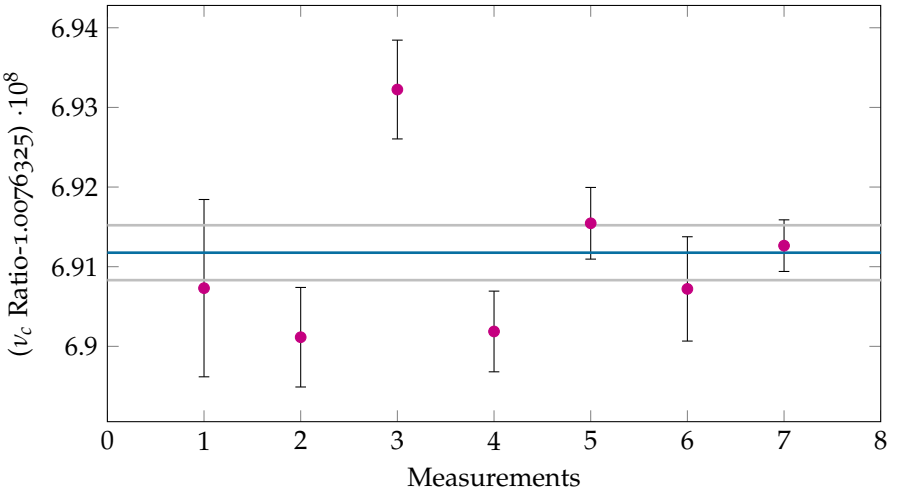

Figure 6.6: Shown are all measured single ratio determination with the alternating PnP technique with simultaneous axial measurement. With the blue line, the mean value is indicated while the grey lines indicates the error of the mean determination.

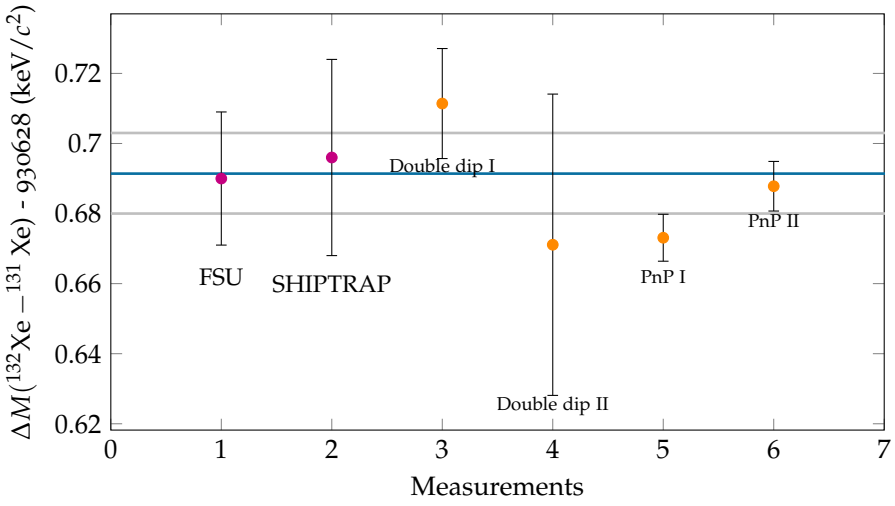

Figure 6.7: Shown are Penning-trap mass measurements of the mass difference of ^{132}Xe $-^{131}$ Xe. The purple points are measured by the labeled Penning trap mass spectrometer. The orange points are measured by PENTATRAP with different methods as labeled, where (I) refers to the sequential measurements and (II) to the alternating ones. Note, the error bars on the PENTATRAP measurements are only statistical errors, since the systematic errors are not yet known, studies are ongoing. However, the errors of the other measurements are statistical errors and systematic errors combined. The literature value with its error band is marked as an blue line.

7 CONCLUSION AND OUTLOOK

From the first half of this PhD time, since every repair attempt on the predecessor cryogenic setup were not successful, only the modification of the beamline and the determination of the Q-value of the electron capture in ^{163}Ho have been included into this thesis. The reported progress on PENTATRAP - from the design study of the current cryogenic setup to the first "proof-of-principle" mass-ratio measurement with the PnP technique - took place in the second half of the PhD time, which encompasses the last two years:

Q-Value of the EC in ^{163}Ho

To investigate the discrepancy between the Q-values obtained indirectly in different experiments, the first direct measurement of the Q-value of the EC in ^{163}Ho was carried out with SHIPTRAP and the results of this measurement are presented in this thesis. The obtained value of 2.833(32) keV is in agreement with the Q-values obtained with cryogenic microcalorimetry and reveals a 7σ discrepancy to the AME 2012 evaluated value. The new Q-value recommended by AME 2017 is already based on our result. Moreover, the use of the new PI-ICR method enables one to reach an uncertainty which is sufficient for the ECHo-1k experiment to achieve a statistical uncertainty below $10\,\mathrm{eV}/c^2$ in the electron-neutrino mass determination.

PENTATRAP

The Penning-trap mass spectrometer PENTATRAP plans to reach a relative uncertainty of a few parts in 10^{12} for highly charged ions in the mid to heavy mass regime (atomic mass numbers > 10). This requires an advanced experimental setup which overcomes current limitations in existing Penning-trap mass spectrometers. The new modification of the beamline and the cryogenic setup was designed, built and commissioned within this thesis. However, several parts like the design and production of the axial-resonators, the axial and cyclotron amplifiers and the design of the new trap were not part of this work but were successfully integrated into the designed setup.

The new cryogenic setup is a suitable tool to carry out high-precision measurements in a few parts in 10^{12}. Due to its two vacuum chambers, it is very robust against any vacuum leak. This robustness will be further improved by installing the presented cryogenic valve. The cabling concept uses successfully commercially available connectors which improves maintainability of PENTATRAP.

The start of the commissioning of PENTATRAP was presented. Single ion preparation and the control over all ion motions were demonstrated. Through the measurement of the temperature of the ion motions, it was proven that the inner parts are in good thermal contact with the liquid helium. A professional sound card with a self-made software is used as an alternative to commercial FFT-analyzers. Moreover, a hardware modification of this sound card made it possible to use it for phase sensitive methods, too. The first test of PENTATRAP was done with the measurement of the

free cyclotron-frequency ratio of $^{131}Xe^{17+}$ and $^{132}Xe^{17+}$. Although potential sources of systematic errors are still investigated, the achieved agreement with the literature value confirms the capability of reaching a sub 10^{-11} uncertainty with PENTATRAP in mass-ratio measurements of even heavy nuclides.

OUTLOOK

With the knowledge gained during the assembly and commissioning of the new setup, some improvements are already designed and in the workshop. As soon as all new parts are available, PENTATRAP will be upgraded. All five traps will be equipped with an individual detection system. This enables finally the testing of the new measurement schemes and proceeding to reach relative uncertainties of a few parts in 10^{12}.

Nevertheless, the setup in its present state already allows the routine conductance of mass-ratio measurements with relative uncertainties close to 10^{-11}. The reached performance of PENTATRAP is sufficient to allows us to carry out in the near future a series of mass measurements. Just to name some of them:

1. The determination of the binding energies in highly charged ions. For example the binding energy of the last electron of $^{132}Xe^{18+}$. The measured binding energy will be then compared to the QED calculations [76],

2. The measurement of the mass difference of $^{40}Ca^{17+}$ and $^{48}Ca^{17+}$ to improve various QED calculations [77] which are currently limited by the mass uncertainty of this nuclei pair. The advantages with PENTATRAP is the possibility to measure the mass difference directly of the highly charged ions. Thus, no knowledge about the electron binding energy is needed to calculate back from the atomic mass to the highly-charged ion mass.

3. The measurement of the Q-value of the β-decay of ^{187}Re. ^{187}Re is a candidate, similar as ^{163}Ho, for experiments on the improvement of the upper limit of the electron-neutrino mass.

4. The measurement of the mass difference of ^{35}Cl and ^{36}Cl which will be compared with a gamma spectroscopy of the neutron capture of ^{35}Cl. This measurement aims to improve the test on special relativity $E = mc^2$ [78] about an order of magnitude.

To be able to load in the traps highly charged ions of rare species where only small amounts are available, the new TIP-EBIT will be installed at the PENTATRAP beamline soon. For improving beamline transport efficiency, the current room-temperature charge amplifier will be exchanged with a cryogenic charge amplifier. We expect an improvement of roughly a factor 100, as shown in [60]. This would result in a single highly charged ion sensitivity, which can be used to optimize the beamline transport efficiency.

Finally with the new upgrade, the Q-value of the EC in ^{163}Ho will be further improved to support the next phases in the ECHo collaboration and thus to lower the upper limit of the electron-neutrino mass below $1\,eV/c^2$ and further.

[1] C. L. Cowan et al. "Detection of the Free Neutrino: a Confirmation." In: *Science* 124.3212 (1956), pp. 103–104. ISSN: 0036-8075. DOI: 10.1126/science.124.3212.103.

[2] G. Danby et al. "Observation of High-Energy Neutrino Reactions and the Existence of Two Kinds of Neutrinos." In: *Phys. Rev. Lett.* 9 (1 1962), pp. 36–44. DOI: 10.1103/PhysRevLett.9.36.

[3] B. T. Cleveland et al. "Measurement of the solar electron neutrino flux with the Homestake chlorine detector." In: *The Astrophysical Journal* 496.1 (1998), p. 505.

[4] Q. R. Ahmad et al. "Direct Evidence for Neutrino Flavor Transformation from Neutral-Current Interactions in the Sudbury Neutrino Observatory." In: *Phys. Rev. Lett.* 89 (1 2002), p. 011301. DOI: 10.1103/PhysRevLett.89.011301.

[5] Z. Maki et al. "Remarks on the Unified Model of Elementary Particles." In: *Progress of Theoretical Physics* 28.5 (1962), pp. 870–880. DOI: 10.1143/PTP.28.870.

[6] T. K. Kuo et al. "Neutrino oscillations in matter." In: *Rev. Mod. Phys.* 61 (4 1989), pp. 937–979. DOI: 10.1103/RevModPhys.61.937.

[7] S. M. Bilenky et al. "Massive neutrinos and neutrino oscillations." In: *Rev. Mod. Phys.* 59 (3 1987), pp. 671–754. DOI: 10.1103/RevModPhys.59.671.

[8] G.L. Fogli et al. "Global analysis of three-flavor neutrino masses and mixings." In: *Progress in Particle and Nuclear Physics* 57.2 (2006), pp. 742 –795. ISSN: 0146-6410. DOI: 10.1016/j.ppnp.2005.08.002.

[9] I. Esteban et al. "Updated fit to three neutrino mixing: exploring the accelerator-reactor complementarity." In: *Journal of High Energy Physics* 2017.1 (2017), p. 87. ISSN: 1029-8479. DOI: 10.1007/JHEP01(2017)087.

[10] K.N. Abazajian et al. "Cosmological and astrophysical neutrino mass measurements." In: *Astroparticle Physics* 35.4 (2011), pp. 177 –184. ISSN: 0927-6505. DOI: 10.1016/j.astropartphys.2011.07.002.

[11] B. McKellar. "The influence of mixing of finite mass neutrinos on beta decay spectra." In: *Physics Letters B* 97.1 (1980), pp. 93 –94. ISSN: 0370-2693. DOI: 10.1016/0370-2693(80)90554-7.

[12] E. W. Otten et al. "Neutrino mass limit from tritium beta decay." In: *Reports on Progress in Physics* 71.8 (2008), p. 086201. URL: http://stacks.iop.org/0034-4885/71/i=8/a=086201.

[13] V. N. Aseev et al. "Upper limit on the electron antineutrino mass from the Troitsk experiment." In: *Phys. Rev. D* 84 (11 2011), p. 112003. DOI: 10.1103/PhysRevD.84.112003.

[14] Ch. Kraus et al. "Final results from phase II of the Mainz neutrino mass searching tritium β decay." In: *The European Physical Journal C - Particles and Fields* 40.4 (2005), pp. 447–468. ISSN: 1434-6052. DOI: 10.1140/epjc/s2005-02139-7.

[15] P. T. Springer et al. "Measurement of the neutrino mass using the inner bremsstrahlung emitted in the electron-capture decay of ^{163}Ho." In: *Phys. Rev. A* 35 (2 1987), pp. 679–689. DOI: 10.1103/PhysRevA.35.679.

[16] F. M. Penning. "Die Glimmentladung bei niedrigem Druck zwischen koaxialen Zylindern in einem axialen Magnetfeld." In: *physica* 3.9 (1936), pp. 873–894.

[17] H. Dehmelt. "Experiments with an isolated subatomic particle at rest." In: *AIP Conference Proceedings*. Vol. 233. 1. AIP. 1991, pp. 28–45.

[18] L. S. Brown et al. "Precision spectroscopy of a charged particle in an imperfect Penning trap." In: *Physical Review A* 25.4 (1982), p. 2423.

[19] G Gabrielse et al. "Open-endcap Penning traps for high precision experiments." In: *International Journal of Mass Spectrometry and Ion Processes* 88.2-3 (1989), pp. 319–332.

[20] L. S. Brown et al. "Geonium theory: Physics of a single electron or ion in a Penning trap." In: *Rev. Mod. Phys.* 58 (1 1986), pp. 233–311. DOI: 10.1103/RevModPhys.58.233.

[21] P. J. Mohr et al. "CODATA recommended values of the fundamental physical constants: 2014." In: *Journal of Physical and Chemical Reference Data* 45.4 (2016), p. 043102.

[22] DJ Wineland et al. "Principles of the stored ion calorimeter." In: *Journal of Applied Physics* 46.2 (1975), pp. 919–930.

[23] S. Sturm. "The g-factor of the electron bound in 28 Si 13: The most stringent test of bound-state quantum." In: (2012).

[24] S. Sturm. personal communication.

[25] J. Verdú et al. "Calculation of electrostatic fields using quasi-Green's functions: application to the hybrid Penning trap." In: *New Journal of Physics* 10.10 (2008), p. 103009.

[26] J. Ketter et al. "First-order perturbative calculation of the frequency-shifts caused by static cylindrically-symmetric electric and magnetic imperfections of a Penning trap." In: *International Journal of Mass Spectrometry* 358 (2014), pp. 1–16.

[27] B. Alpert et al. "Holmes." In: *The European Physical Journal C* 75.3 (2015), p. 112.

[28] J. J. Simpson. "Measurement of the β-energy spectrum of ^{3}H to determine the antineutrino mass." In: *Phys. Rev. D* 23 (3 1981), pp. 649–662. DOI: 10.1103/PhysRevD.23.649.

[29] S. Eliseev et al. "Direct measurement of the mass difference of Ho 163 and Dy 163 solves the Q-value puzzle for the neutrino mass determination." In: *Physical review letters* 115.6 (2015), p. 062501.

[30] E. Achterberg et al. "Nuclear Data Sheets for A = 193." In: *Nuclear Data Sheets* 107.1 (2006), pp. 1 –224. ISSN: 0090-3752. DOI: 10.1016/j.nds.2005.12.001.

[31] E. G. Myers et al. "Atomic Masses of Tritium and Helium-3." In: *Phys. Rev. Lett.* 114 (1 2015), p. 013003. DOI: 10.1103/PhysRevLett.114.013003.

[32] M. Galeazzi et al. "End-point energy and half-life of the 187 Re β decay." In: *Physical Review C* 63.1 (2000), p. 014302.

[33] L. Gastaldo et al. "The electron capture in 163Ho experiment–ECHo." In: *The European Physical Journal Special Topics* 226.8 (2017), pp. 1623–1694.

[34] M. Wang et al. "The Ame2012 atomic mass evaluation." In: *Chinese Physics C* 36.12 (2012), p. 1603. URL: http://stacks.iop.org/1674-1137/36/i=12/a=003.

[35] M. Block et al. "The ion-trap facility SHIPTRAP." In: *The European Physical Journal A-Hadrons and Nuclei* 25.1 (2005), pp. 49–50.

[36] A. Chaudhuri et al. "Carbon-cluster mass calibration at SHIPTRAP." In: *The European Physical Journal D* 45.1 (2007), pp. 47–53.

[37] S. Eliseev et al. "A phase-imaging technique for cyclotron-frequency measurements." In: *Applied Physics B* 114.1-2 (2014), pp. 107–128.

[38] P. R. Bevington et al. *Data reduction and error analysis for the physical sciences*.

[39] F. DiFilippo et al. "Accurate atomic mass measurements from Penning trap mass comparisons of individual ions." In: *Physica Scripta* 1995.T59 (1995), p. 144.

[40] G. Audi et al. "The Ame2012 atomic mass evaluation." In: *Chinese physics C* 36.12 (2012), p. 1287.

[41] F. Gatti et al. "Calorimetric measurement of the 163Ho spectrum by means of a cryogenic detector." In: *Physics Letters B* 398.3 (1997), pp. 415 –419. ISSN: 0370-2693. DOI: 10.1016/S0370-2693(97)00239-6.

[42] P. C.-O. Ranitzsch et al. "Development of Metallic Magnetic Calorimeters for High Precision Measurements of Calorimetric 187Re and 163Ho Spectra." In: *Journal of Low Temperature Physics* 167.5 (2012), pp. 1004–1014. ISSN: 1573-7357. DOI: 10.1007/s10909-012-0556-0.

[43] J.U. Andersen et al. "A limit on the mass of the electron neutrino: The case of 163Ho." In: *Physics Letters B* 113.1 (1982), pp. 72 –76. ISSN: 0370-2693. DOI: 10.1016/0370-2693(82)90112-5.

[44] P. A. Baisden et al. "Measurement of the half-life of ^{163}Ho." In: *Phys. Rev. C* 28 (1 1983), pp. 337–341. DOI: 10.1103/PhysRevC.28.337.

[45] E. Laegsgaard et al. *The capture ratio N/M in the EC beta decay of* ^{163}Ho. Tech. rep. 198409294, 1984.

[46] F. X. Hartmann et al. "Observation of N and M orbital-electron capture in the decay of ^{163}Ho." In: *Phys. Rev. C* 31 (4 1985), pp. 1594–1596. DOI: 10.1103/PhysRevC.31.1594.

[47] F.X. Hartmann et al. "High temperature gas proportional detector techniques and application to the neutrino mass limit using 163Ho." In: *Nuclear Instruments and Methods in Physics Research Section A: Accelerators, Spectrometers, Detectors and Associated Equipment* 313.1 (1992), pp. 237 –260. ISSN: 0168-9002. DOI: 10.1016/0168-9002(92)90102-A.

[48] S. Yasumi et al. "The mass of the electron neutrino using electron capture in 163Ho." In: *Physics Letters B* 181.1 (1986), pp. 169 –172. ISSN: 0370-2693. DOI: 10.1016/0370-2693(86)91277-3.

[49] S. Yasumi et al. "The mass of the electron neutrino from electron capture in 163Ho." In: *Physics Letters B* 334.1 (1994), pp. 229 –233. ISSN: 0370-2693. DOI: 10.1016/0370-2693(94)90616-5.

[50] M. Jung et al. "First observation of bound-state β-decay." In: *Phys. Rev. Lett.* 69 (15 1992), pp. 2164–2167. DOI: 10.1103/PhysRevLett.69.2164.

[51] K. Blaum et al. "Penning traps as a versatile tool for precise experiments in fundamental physics." In: *Contemporary Physics* 51.2 (2010), pp. 149–175.

[52] J. Repp et al. "PENTATRAP: a novel cryogenic multi-Penning-trap experiment for high-precision mass measurements on highly charged ions." In: *Applied Physics B* 107.4 (2012), pp. 983–996.

[53] A. Dörr. "PENTATRAP: A novel Penning-trap system for high-precision mass measurements." PhD thesis. Ruprecht-Karls-Universität Heidelberg, 2015.

[54] R. X. Schuessler. "Pentatrap." PhD thesis. Ruprecht-Karls Universität Heidelberg, 2019.

[55] G. Zschornack et al. "Status report of the Dresden EBIS/EBIT developments a." In: *Review of Scientific Instruments* 81.2 (2010), 02A512.

[56] JR. C. López-Urrutia et al. "Progress at the Heidelberg EBIT." In: *Journal of Physics: Conference Series*. Vol. 2. 1. IOP Publishing. 2004, p. 42.

[57] M. Door. "Erzeugung hochgeladener Chlor- und Siliziumionen für das Pentatrap-Experiment in einer Elektronenstrahlionenquelle unter Anwendung der MIVOC-Methode." Ruprecht-Karls-Universität Heidelberg, 2015.

[58] J. Repp. "The setup of the high-precision Penning-trap mass spectrometer PENTATRAP and first production studies of highly charged ions." PhD thesis. 2012.

[59] P. Filianin. "Pentatrap." PhD thesis. Ruprecht-Karls Universität Heidelberg, 2019.

[60] S. Sturm et al. "The Alphatrap Experiment." In: *The European Physical Journal Special Topics* (2018).

[61] C. Roux. "High-resolution mass spectrometry: The trap design and detection system of PENTATRAP and new Q-values for neutrino studies." PhD thesis. Ruprecht-Karls Universität Heidelberg, 2012.

[62] L. Brillouin. "A theorem of Larmor and its importance for electrons in magnetic fields." In: *Physical Review* 67.7-8 (1945), p. 260.

[63] G. Herrmann. "Optical theory of thermal velocity effects in cylindrical electron beams." In: *Journal of Applied Physics* 29.2 (1958), pp. 127–136.

[64] Cypress. *AN1032 - Using Decoupling Capacitors*. Tech. rep. Cypress, 2017.

[65] Ch. Böhm et al. "An ultra-stable voltage source for precision Penning-trap experiments." In: *Nuclear Instruments and Methods in Physics Research Section A: Accelerators, Spectrometers, Detectors and Associated Equipment* 828 (2016), pp. 125 –131. ISSN: 0168-9002. DOI: 10.1016/j.nima.2016.05.044.

[66] Ch. Böhm. "High-precision mass measurements of neutron-deficient Tl isotopes at ISOLTRAP and the development of an ultra-stable voltage source for the PENTATRAP experiment." PhD thesis. Ruprechts-Karls-Universität Heidelberg, 2015.

[67] *Experimental Physics and Industrial Control System*. https://epics.anl.gov/. Accessed: 2018-04-10.

[68] M Door. "Master thesis." PhD thesis. Ruprecht-Karls Universität Heidelberg, 2018.

[69] *Datasheet: AK4621 24-Bit 192kHz Stereo Audio CODEC*. https://www.akm.com/akm/en/file/datasheet/AK4621EF.pdf. Accessed: 2018-04-10.

[70] R. X. Schüssler et al. "Recent Developments at the High-Precision Mass Spectrometer PENTATRAP." In: *Proceedings of the 12th International Conference on Low Energy Antiproton Physics (LEAP2016)*. DOI: 10.7566/JPSCP.18.011020.

[71] M. Höcker et al. "Atomic masses of ^{82,83}Kr and ^{131,134}Xe." In: *Phys. Rev. A* 88 (5 2013), p. 052502. DOI: 10.1103/PhysRevA.88.052502.

[72] M. Wang et al. "The AME2016 atomic mass evaluation (II). Tables, graphs and references." In: *Chinese Physics C* 41.3 (2017), p. 030003.

[73] GC. Rodrigues et al. "Systematic calculation of total atomic energies of ground state configurations." In: *Atomic Data and Nuclear Data Tables* 86.2 (2004), pp. 117–233.

[74] E. A. Cornell et al. "Single-ion cyclotron resonance measurement of $M(CO^+)/M(N_2^+)$." In: *Phys. Rev. Lett.* 63 (16 1989), pp. 1674–1677. DOI: 10.1103/PhysRevLett.63.1674.

[75] D. A. Nesterenko et al. "Direct determination of the atomic mass difference of ^{187}Re and ^{187}Os for neutrino physics and cosmochronology." In: *Phys. Rev. C* 90 (4 2014), p. 042501. DOI: 10.1103/PhysRevC.90.042501.

[76] A. V. Malyshev et al. "QED calculation of the ground-state energy of berylliumlike ions." In: *Phys. Rev. A* 90 (6 2014), p. 062517. DOI: 10.1103/PhysRevA.90.062517.

[77] F. Köhler et al. "Isotope dependence of the Zeeman effect in lithium-like calcium." In: *Nature Communications* 7 (2016). Article. DOI: 10.1038/ncomms10246.

[78] Simon Rainville et al. "A direct test of E=mc2." In: *Nature* 438 (2005), 1096 EP –. URL: http://dx.doi.org/10.1038/4381096a.

DANKSAGUNG

Zu allererst möchte ich meinem Betreuer *Klaus Blaum* danken. Vielen Dank für deine Unterstützung, das stets offene Ohr für allerlei Probleme, für all die guten Ratschläge und insbesondere für das exzellente Arbeitsumfeld, das du geschaffen hast.

Herzlichen Dank an *Ulrich Uwer* für die Bereitschaft die Aufgabe des Zweigutachters zu übernehmen.

Vielen Dank an alle PENTATRAPer: *Christoph*, *Menno*, *Pascha*, *Rima*, und *Sergey* und an die ehemaligen Gruppenmitglieder: *Christine*, *Julia*, *Mikhail* , *Christian* und *Andreas*. *Rima*, danke für die gemeinsame Zeit im Büro und danke für das Organisieren von Events auch außerhalb des MPIKs. *Menno*, danke für das Teilen deines Enthusiasmus für PYTHON und insgesamt für allerlei Basteleien. Sergey, danke für die zahlreichen lehreichen Diskussionen und das teilen deiner Laborerfahrung.

Zudem möchte ich auch allen in den Nachbargruppen danken, den THeTRAPpern und ALPHATRAPpern: Insbesondere *Martin* und *Andi*, möchte ich für die zahlreichen Diskussionen und für eure Begeisterung für alle Arten von Bastelleien danken. *Sven*, danke für das Teilen deines großen Penning-trap Wissens und deiner Laborerfahrung.

Außerdem möchte ich mich herzlich bedanken bei allen Kletterbegeisterten: *Hendrik*, *Alban* und *Giovanni* für die wöchentlichen gemeinsamen Klettereinheiten. Ein besonderer Dank an *Giovanni* der mich das erste Mal auf eine Mehrseillängentour mitgenommen hat. Vielen Dank für deine Freundschaft und all die alpinen Abenteuer dir wir zusammen erlebt haben und hoffentlich noch werden.

Zu guter Letzt möchte ich meiner Familie danken: Meinen Eltern *Erika* und *Olgierd* und meinen Großeltern für all die bedingungslose Unterstützung. Vielen Dank an meine Schwester *Desiree* und meinem Schwager *Robert* für alles. Insbesondere einen Dank an meine Nichte *Elea*, durch dich sind Familienfeiern wieder spannender geworden.